NEW NMR METHODS FOR CHARACTERIZING NANOPOROUS STRUCTURES AND NANOCONFINED SHALE GAS

Yun-Zhao Xing

A dissertation submitted to the faculty at the University of North Carolina at Chapel Hill in partial fulfillment of the requirements for the degree of Doctor of Philosophy in the Department of Applied Physical Sciences.

Chapel Hill
2017

Approved by:

Yue Wu

Sean Washburn

Jianping Lu

Jack Ng

Alfred Kleinhammes

ABSTRACT

Yun-Zhao Xing: New NMR Methods for Characterizing
Nanoporous Structures and Nanoconfined Shale Gas
(Under the direction of Yue Wu)

Nanoporous materials, such as activated carbons and gas shale rocks, play crucial roles in both industry and daily life. Activated carbons have been used in various areas, such as water filtration, supercapacitors, and catalysis carriers, and shale gas has contributed more than 50% of the annual natural gas production in the United States. In all those areas, the performance of nanoporous materials is controlled by the properties of nanopores. However, both accurate characterization of micropores in activated carbons and evaluation of adsorption capability of high-pressure nature gas in shale rocks are challenging problems.

We first introduce a room temperature method for determining micropore size distribution of activated carbons based on ^{1}H nuclear magnetic resonance (NMR) of adsorbed water under magic angle spinning (MAS). The observed NMR peak shift comes from the nucleus-independent chemical shift (NICS). The density functional theory computation of NICS yields a quantitative relationship between the observed peak shift and the micropore size. This relationship provides a direct link between the ^{1}H MAS NMR lineshape and micropore size distribution. The NICS NMR porometry technique is shown to be useful for characterizing micropore structures of highly carbonized activated carbons.

In the second part, we develop a novel method for the evaluation of the gas storage capability of gas shale based on NMR T_2 contrast. The FT-NMR spectral lineshape of gas stored inside pores, which reveal the properties of nanopores, are also studied by experiments. The combined information from spectra, longitudinal relaxation, and transverse relaxation not

only offers a powerful tool for the evaluation of gas storage quantity but also provides valuable information for gas storage mechanisms.

To my parents and my beloved grandfather Chunxiang.
Thank you for all the love you gave to me

ACKNOWLEDGEMENTS

First, I would like to express my deepest gratitude to my advisor Prof. Yue Wu. During the past seven years, I have gained enormous invaluable experience from him. His enthusiasm for science and his passion for discovering the unknown world served as a vivid model of an ideal scientist for me. Sometimes, I could see the happiness directly from his eyes when he was sharing some new scientific ideas. Without his great patience and selfless help, I could not finish my Ph.D. work. I will always remember the times when we were sitting side by side in front of the computer and discussing the experimental data. I will miss those precious moments in my future life.

Second, I want to show my sincere appreciation to Prof. Alfred Kleinhammes. He is both a good friend and an excellent academic mentor. He is the one I could rely on all the time without any anxiety or hesitation. His positive attitude, encouragements, and especially the lively sense of humor enlightened all the shadows of hard times in my research life. His profound knowledge and generous help were crucial elements in my Ph.D. work.

Third, I would like to thank Songhua Chen and Paul Ganssle from Halliburton. The internship experience in Halliburton made me much more confident. It's the first time that I realized my hard work would be rewarding and also appreciated by others. Paul is a selfless friend and a great mentor. He guided me to proceed through the work patiently and encouraged me with each small improvement.

Fourth, I would like to thank Weijian Mo from Shell Exploration & Production Company and Caineng Zou from PetroChina Research Insititute of Petroleum Exploration & Development. They provide us not only the valuable shale samples and the sample

information but also many helpful suggestions the interpretation of gas storage results.

Finally, I would like to thank all my group members. They are generous and good friends who filled my Ph.D. life with happiness and precious memories. To Horst Kessemeir, I learned many funny old stories and valuable wisdom of life. To Zhi-Xiang Luo who is a smart and funny guy, I enjoyed every academic discussion and non-academic chat with him. To Patrick Doyle, I greatly appreciate your great help on my dissertation and your writing skill.

TABLE OF CONTENTS

LIST OF TABLES

LIST OF FIGURES

LIST OF ABBREVIATIONS

AC	activated carbon
ACS	activated carbons
AQ	acquisition time
BET	Brunauer-Emmett-Teller
BJH	Barrett-Joyyner-Halenda
DFT	density functional theory
FT	Fourier transform
GTOs	Gaussian-type orbitals
IUPAC	International Union of Pure and Applied Chemistry
MAS	magic angle spinning
NICS	nucleus independent chemical shift
NLDFT	nonlocal density functional theory
NMR	nuclear magnetic resonance
PSD	pore size distribution
RD	ring down
RE	Rock Eval
RF	radio frequency
TOC	total organic carbon

CHAPTER 1. INTRODUCTION

1.1 Dissertation Outline

In Chapter 1, Section 1.2 explains the motivations of my research. Section 1.3 introduces the mechanisms of conventional adsorption methods based on different models and different pore size and discusses the issues of various models and approaches. Section 1.4 briefly introduces the NMR theory and some experimental details.

In Chapter 2, a simple room temperature method is presented for determining micropore size distribution of activated carbons. Section 2.1 explains the origin of the NICS effect and the NICS effect in AC samples. Section 2.2 uses DFT simulation to study NICS effect in AC samples. Section 2.3 introduces the models and the equations of the method, which is developed for the characterization of micropores in activated carbons. Section 2.4 provides the experimental details. Section 2.5 is a brief summary of the NICS NMR porometry technique introduced in the chapter.

In Chapter 3, a novel method for evaluation of the gas storage capability of gas shale is introduced. Section 3.1 covers a brief introduction to shale gas systems and their properties. It also includes some background information, such as the diffusion of high-pressure methane, the magnetic field inside a packed solid system, *et cetera*. Section 3.2 explains the primary NMR relaxation mechanisms of methane gas in the gas shale packing system. Section 3.3 introduces the core concept of the method for evaluating the gas storage. Section 3.4 provides the experimental details. Section 3.5 discusses the issues with the experiments.

In Chapter 4, the method introduced in Chapter 3 is used to study several different gas shale samples. Section 4.1 gives a brief introduction to several standard characterization

parameters used in the oil industry and those parameters values of the samples that we have studied by NMR. Section 4.2 presents and analyzes the experimental NMR results. Section 4.3 discusses several possible ways to correlate NMR results with the standard parameters. Section 4.4 discusses several possible parameters to predict methane storage capability.

Chapter 5 summarizes the whole dissertation and also puts the significance of my research into a broader context.

1.2 Motivations

1.2.1 Activated Carbon

Activated carbons (ACs) are widely used in many applications, such as filtration and adsorption, chemical recovery and purification, catalysis, and fuel cells [1]. All these applications of ACs depend strongly on their porous structural features, characterized by a complex porous network consisting of micropores (pore size of less than 2 nm), mesopores (pore size between 2 and 50 nm), and macropores (pore size greater than 50 nm) [2]. In particular, the micropore network of ACs plays a crucial role in most of their applications. For measurements of pore size and pore size distribution (PSD) of ACs, simple characterization methods are highly desirable.

The conventional way to characterize the PSD is adsorption isotherm measurements of probe molecules (He, Ar, N_2, CO_2, etc.). Among these, N_2 adsorption at 77 K is the most widely used technique for ACs characterization [3]. Several idealized theoretical models have been employed to interpret such adsorption isotherms and to derive the surface area and the PSD. Here, the most well-known is the Brunauer-Emmett-Teller (BET) equation for the interpretation of N_2 adsorption isotherm. However, this method faces problems when applied to micropores. There, micropore filling is an important mechanism of adsorption, which violates the assumptions of BET [2]. Alternative methods have also been proposed for determining the PSD of micropores such as the Dubinin-Stoeckli equation [4]. However, this

equation is semi-empirical, requires knowledge of the binding energy, and assumes a Gaussian pore size distribution [4]. Recently, using density functional theory (DFT) computations, the relationship between N_2 or Ar isotherms and pore size has been predicted [5-7]. This method needs information on interaction potentials and requires isotherms measured at extremely low relative pressure $P/P_0 < 10^{-5}$ (P_0 is the saturated vapor pressure), which is very time-consuming. More details of conventional adsorption characterization methods are introduced in Section 1.3.

In Chapter 2, a simple room temperature method is presented for determining micropore size distribution of activated carbons based on ^{1}H nuclear magnetic resonance (NMR) of adsorbed water under magic angle spinning (MAS). The observed NMR peak shift is determined by nucleus-independent chemical shift (NICS). The Density Functional Theory computation of NICS yields a quantitative relationship between the observed peak shift and the micropore size. This relationship provides a direct link between the ^{1}H MAS NMR lineshape and micropore size distribution. The NICS NMR porometry technique is shown to be useful for characterizing micropore structures of highly carbonized activated carbons.

1.2.2 Gas Shale

In recent years, shale gas has become one of the most valuable natural gas resources. Due to technological improvements in hydraulic fracturing, the production of shale gas has grown from only 1% to over 20% of U.S. natural gas production and been predicted to reach 46% by 2035 [8]. Gas shale is considered an unconventional resource since the gas stored in the rock is inaccessible by conventional production methods. The majority of gas in shale is well sealed and stored in the organic kerogen nano- and micro-pores [9]. The porosity and gas permeability in gas shale are usually very low, which makes the estimation of storage challenging. More details of unconventional petroleum resources and gas shale system are introduced in Chapter 3.

Conventionally, gravimetric or volumetric methods are used to characterize shale gas storage. They are well-developed lab techniques for probing the adsorption quantity and mechanism. However, the low porosity and resulting low gas adsorption rate in gas shale introduce significant relative uncertainty into the results of conventional methods. Meanwhile, to estimate the total gas in place, other techniques such as volume and/or density measurements need to be involved, which introduces, even more, uncertainties [10]. Although by using extracted kerogen as a substitute of original gas shale may increase the adsorption in a unit mass of the testing sample, it's in doubt if the extraction procedure would change the nanopores volume or structure in kerogen. The mechanisms and disadvantages of conventional methods are introduced in Section 1.3.

In Chapter 3, a novel method for evaluation of the gas storage capability of gas shale based on NMR T_2 contrast is introduced. The Fourier transform NMR spectra of gas stored inside pores, which reveal the information of the pore space, are also studied in these experiments. The combined information from spectra, longitudinal relaxation, and transverse relaxation not only offers a powerful tool for evaluating the gas storage but also provides valuable information about the gas storage mechanism.

1.3 Gas Adsorption Method

Gas adsorption measurement is the most widely used characterization methods for determining the surface area and pore size distribution in a variety of solid materials. Nitrogen (at 77K) is the most common adsorbate used for the characterization of porous materials. The Brunauer-Emmett-Teller (BET) method [11], although it is based on an over-simplified model of multilayer adsorption, has been used as a standard procedure for the determination of surface area. However, M. M. Dubinin reported that adsorption in micropores is dominated by a volumetric micropore filling process, which could be described by an empirical equation [12, 13]. With the development of scientific computations, Density

Functional Theory (DFT) approaches are also used for the characterization of micropore size and PSD [5, 7, 14]. A brief introduction to the procedure, theory, and issues of the gas adsorption method is provided in this chapter.

1.3.1 Experimental Methods

The many different experimental systems used to determine the amount of gas adsorbed may be divided into two groups: volumetric methods and gravimetric methods. Gravimetric methods provide a high degree of accuracy, but can only be used with small sample sizes. On the contrary, the volumetric methods can be used with much larger samples, which can better account for the heterogeneity of certain samples, such as gas shale rock [15].

A schematic arrangement of a simultaneous volumetric and gravimetric adsorption experiment is shown in Figure 1.1

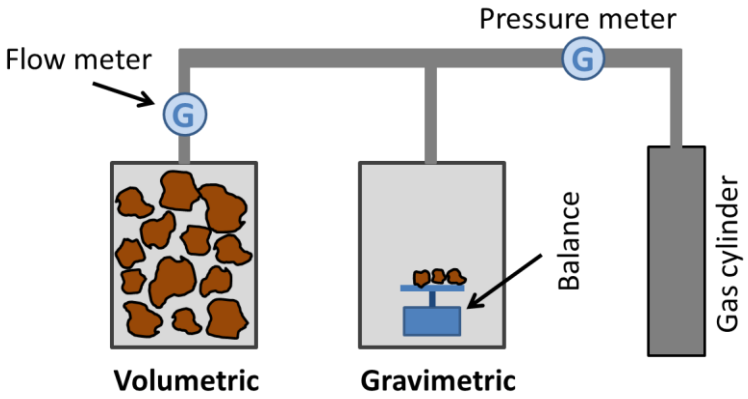

Figure 1.1 Schematic diagram of volumetric and gravimetric methods.

The pressure in the system is controlled precisely. In the volumetric method, the quantity of gas injected into the sample chamber can be measured. In the gravimetric method, the weight of the sample is measured by a high-precision balance. The adsorption isotherm can be acquired through either method.

1.3.2 Classification of Pores and Adsorption Isotherms

As it is mentioned at the beginning of this chapter, the classification of pores depends on the pore sizes [2]:

1. Pores with widths exceeding about 50 nm are defined as *macropores*;
2. Pores with widths between 2 nm and 50 nm are defined as *mesopores*;
3. Pores with widths not exceeding about 2 nm are defined as *micropores*;

Some literature [5, 16] also refined the micropores into two categories:

A. *Ultramicropores* for the pores with widths not exceeding about two molecular diameters (≤ 0.7 nm);
B. *Supermicropores* for the pores in the range of approximately two to five molecular diameters (0.7 nm to 2 nm).

According to the *International Union of Pure and Applied Chemistry* (IUPAC), the majority of physisorption isotherms may be grouped into the six types of isotherms, as shown in Figure 1.2 [2].

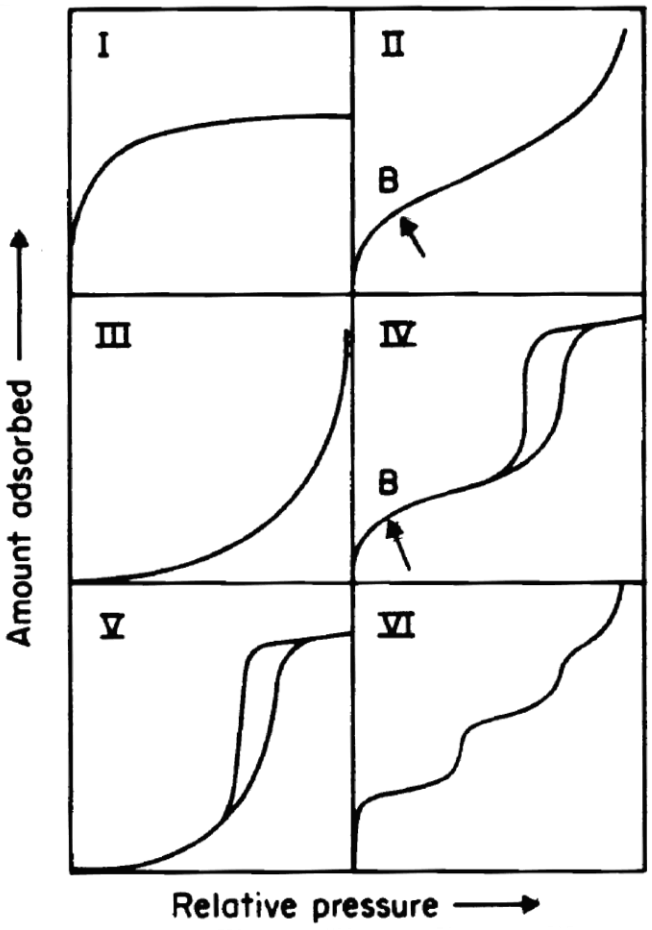

Figure 1.2 Types of physisorption isotherms [2].

Type I isotherms are given by microporous solids with relatively small external surfaces, the limiting uptake being governed by the accessible micropore volume.

Type II isotherms are the typical isotherm obtained from a non-porous or macroporous adsorbent.

Type III isotherms are convex over the entire p/p_0 axis. It can be observed in the system where adsorbate-adsorbate interactions play a significant role.

Type IV isotherms have a hysteresis loop from the capillary condensation taking place in mesopores. The initial part of the Type IV isotherm is attributed to monolayer-multilayer adsorption which follows the same paths as the corresponding part of a Type II isotherm.

Type V isotherms may be found in a certain porous system where adsorbent-adsorbate interaction is weak.

Type VI isotherms represent multilayer adsorption on a uniform non-porous surface.

1.3.3 Langmuir Adsorption Model

In 1916, Langmuir developed a model of adsorption leading to a conception of adsorption as a monolayer [17]. He made two assumptions: first, he assumed that the heat of adsorption would be the same for every molecule which strikes the bare surface and that this heat of adsorption is independent of the other molecules which are held there; second, he assumed that every molecule which hits a molecule already adsorbed, returns immediately to the gas phase. The first assumption implies that the interactions among adsorbate molecules on the adsorbent surface are ignored. The second assumption means the adsorption energy between the molecules adsorbed on the surface and molecules striking it are ignored and leads to the concept of monolayer adsorption. The Langmuir adsorption model is illustrated in Figure 1.3.

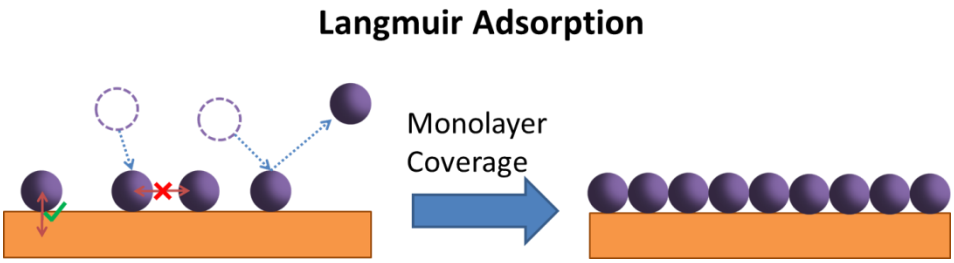

Figure 1.3 An illustration of Langmuir adsorption model.

The equation of Langmuir adsorption is given as following

$$\theta = \frac{k_u p}{1 + k_u p} \tag{1.1}$$

where θ is the fractional occupancy of adsorption sites, and k_u is the associated equilibrium constant, which depends on the temperature, the molar mass of adsorbate, and the adsorption energy. A plot of equation 1.1 is the same shape as a Type I isotherm.

Although the adsorption of fatty acids or fatty alcohols on surfaces of inorganic salts tends to obey the Langmuir adsorption isotherm [18], for most other adsorption systems, when the degree of occupation increases, the adsorbed molecules influence each other not only because of the space they occupy but also because of the mutual van der Waals interaction between them. Moreover, if molecules, when striking a layer of already adsorbed molecules, are attracted by sufficiently great forces, multilayer adsorption needs to be considered.

1.3.4 BET Theory

The most successful model for multilayer adsorption is that published by Brunauer, Emmett, and Teller in 1938 [11], which has become a standard method for characterization of surface area in porous materials. BET theory still uses the simplified assumption that the molecules of one layer do not mutually influence one other while this layer is being built up. It also has the condition that the adsorption energy of the molecules of the first layer is constant and the heat of adsorption for the molecules in each following layers is constant. The

equation for adsorption in BET theory is given as following:

$$n = \frac{kpn_m}{(q-p)\left[1+(k-1)\,p/q\right]} \tag{1.2}$$

where n is the molar number of adsorbed molecules, n_m is the molar number required for full monolayer coverage, q is a constant depending on the adsorption heat for the adsorbate molecules in each of the layers following the first layer, and k is a constant depending on the adsorption heat of both the first layer and further layers.

With the further simplifying assumption that the heat of adsorption and the probability of evaporation of molecules adsorbed on top of other adsorbed molecules equals the heat of evaporation and the probability of evaporation of the molecules from their liquid state, k can be given as following:

$$k = \exp\left(\frac{(Q_a - Q_0)}{RT}\right) \tag{1.3}$$

where R is the ideal gas constant, T is temperature, and Q_a and Q_0 are the adsorption heat of the first layer and following layers respectively. Q_0 equals the latent heat of evaporation of the adsorbate in liquid form. Meanwhile, the assumptions also implicitly require q is p_0, which is the saturated pressure of adsorbate. The equation 1.3 can thus be further simplified:

$$n = \frac{kpn_m}{(p_0-p)\left[1+(k-1)\,p/p_0\right]} \tag{1.4}$$

The model and assumptions of BET theory are illustrated in Figure 1.4.

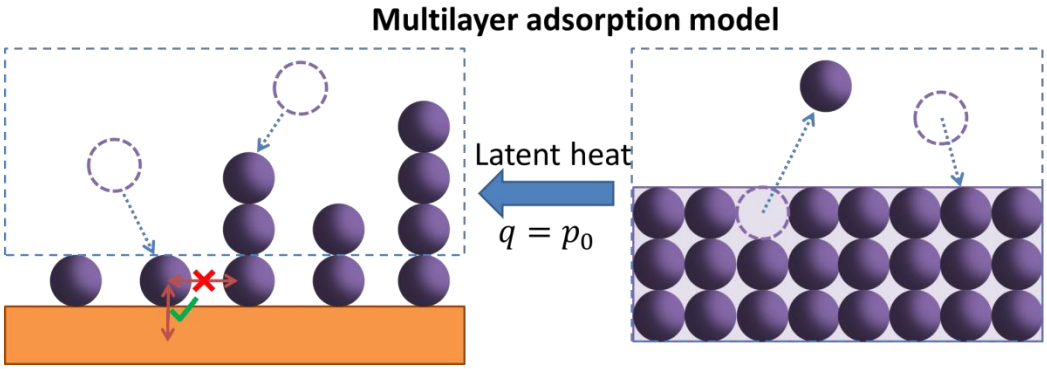

Figure 1.4 An illustration of BET model.

In order to characterize the surface area of adsorbent materials, the nitrogen adsorption isotherms of type II or type IV at $77\ \mathrm{K}$ need to be fitted by the BET equation in the p/p_0 range of $0.05 \sim 0.35$. The fitting range limitation is due to the influence of active spots and restricted adsorption [18]. Point B in Figure 1.2 represents the molar number of nitrogen required to completely cover the monolayer (n_m). It is usually assumed that the BET monolayer is close-packed, giving the *molecular cross-sectional area* of nitrogen in the completed packed monolayer as $a_m(\mathrm{N_2}) = 0.162\ \mathrm{nm}^2$ at $77\ \mathrm{K}$ [2]. Then the surface area can be calculated by $S = n_m \cdot a_m$.

1.3.5 Kelvin Equation

The Barrett-Joyner-Halenda (BJH) method [19], which is based on a modified Kelvin equation, has been widely used to characterize the pore size and PSD of mesopores. As discussed in Section 1.3.2, materials with mesopores show a type IV adsorption isotherm; the apparent hysteresis is due to capillary condensation inside mesopores. The pore size calculation is given by the Kelvin equation of the form

$$\frac{1}{r_1} + \frac{1}{r_2} = -\frac{RT}{\sigma^{\mathrm{lg}} v^{\mathrm{l}}} \ln\left(\frac{p}{p_0}\right) \tag{1.5}$$

where r_1 and r_2 are the principle radii of curvature of the liquid meniscus in the pore, p/p_0 is the relative pressure, σ^{lg} is the surface tension of the liquid condensate, and v^{l}

is its molar volume. In a slit-shaped pore model, as shown in Figure 1.5, the meniscus is hemicylindrical, where $r_1 =$ width of slit, and $r_2 = \infty$.

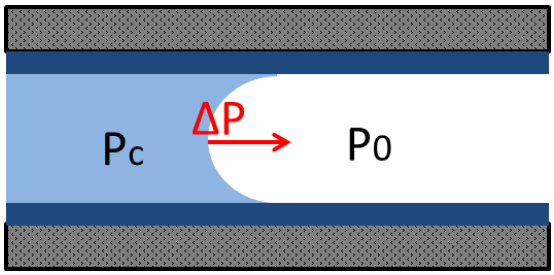

Figure 1.5 Capillary condensation inside slip-shaped pore model.

Capillary condensation is a first order phase transition. The vapor pressure of capillary condensation (p_c) is lower than the saturation pressure (p_0) due to the surface tension at the interfacial meniscus. The Kelvin equation can be deduced from the equilibrium of those pressures.

1.3.6 Micropore Filling

Generally, the adsorption of microporous AC samples shows a typical type I isotherms, however, it cannot be simply described by the Langmuir model. Although the BET theory and the BJH method provide characterizations of the surface area and the pose distribution of mesopores respectively, they fail to characterize micropores due to the micropore filling [2, 12]. Unlike the surface adsorption models discussed in previous sections covering mesopores, the adsorption mechanisms of micropores are volume filling processes [20].

The micropore filling processes of AC sample can be broadly divided into two groups. Ultramicroporous carbons exhibit high adsorption affinity, their isotherms generally having a steep initial increment with a plateau approached at very low p/p_0. The enhanced adsorption energy is due to the significant overlap of the adsorption forces since the pore widths are not much larger than two molecular diameters. This process is also called ‘primary micropore filling’ [21]. The second group occurs in many supermicroporous AC samples which have pore width in the range of approximately two to five molecular diameters. The

supermicropores are filled by a combination of surface coverage at low p/p_0 and a cooperative process at higher p/p_0. It is not a first order phase transition as is the case in capillary condensation since it involves two overlapping stages. Figure 1.6 illustrates 'primary micropore filling' and the cooperative process.

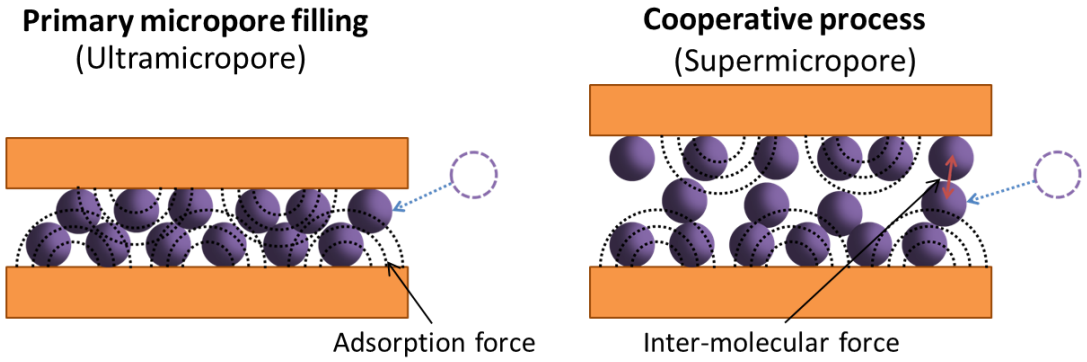

Figure 1.6 Illustration of micropore filling models.

1.3.7 Characterization of Micropores

In order to characterize micropores, in the 1950s, M. M. Dubinin and his co-works developed Dubinin-Radushkevich (DR) equation to described the micropore filling process empirically [12, 22]:

$$W = W_0 \exp\left[-\left(\frac{A}{\beta E_0}\right)^2\right] \tag{1.6}$$

where W is the amount of gas adsorbed at p/p_0, W_0 is the micropore volume, and $A = RT\ln(p/p_0)$. The affinity coefficient, β, is a shifting factor related to the adsorbate. E_0 is the characteristic adsorption energy, and is associated with the isosteric heat of adsorption.

However, there are two principle drawbacks: first, since only the pore volume can be acquired from the DR equation, an arbitrarily chosen functional form of PSD—such as Gaussian distribution—is required for the characterization of pore size and surface area; second, it requires the use of empirical energy parameters to solve for the PSD. Thus, fitting

the isotherm using the DR equation provides insufficient evidence to validate the underlying theory.

Over the past few years, the DFT simulation method, usually in the refined form of nonlocal density functional theory (NLDFT), has become more and more important for the characterization of microporous AC samples [5-7, 14]. However, the DFT method highly depends on the pore structure models, so it requires the solid and surface structures are well known, and the pores are all of a similar, well-defined shape. Moreover, very precise measurements at an ultra-low relative pressure, as low as $p/p_0 \sim 10^{-5}$, are required to characterize the micropore filling processes. It is very time-consuming to wait for the system to reach equilibrium at such low pressures.

1.3.8 Adsorption of High-Pressure Gas

Adsorption methods have also been used to evaluate gas storage capacity of gas shale samples. In contrast to the adsorption measurements discussed previously, the measurements of gas shale adsorption are usually taken at a relatively high temperature and high pressure, such as measuring the adsorption of methane gas at room temperature and 4500 PSI. In this case, the density of gas needs to take into account. The process and principle of a conventional volumetric method for measuring high-pressure gas adsorption are illustrated in Figure 1.7.

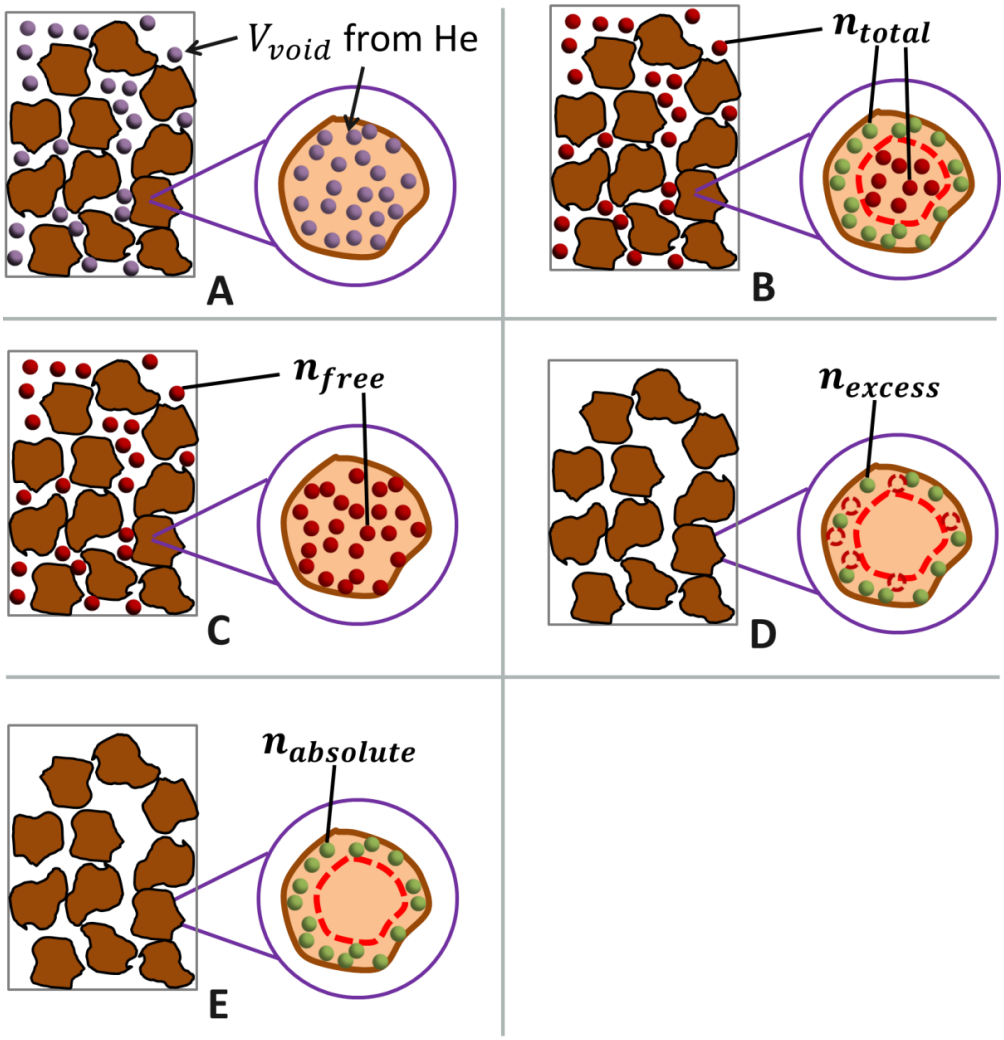

Figure 1.7 An illustration of the volumetric adsorption method process. The brown patterns are porous sample chunks; the purple filled dots are helium atoms (for void volume measurement); red filled dots are 'free gas' probe (methane) molecules; green filled dots are adsorbed probe molecules; empty red circles are the part over-subtracted from adsorbed probe molecules.

The sample is ground into particles and loaded into a vacuum chamber. The measurement steps are listed:

A. The void volume of the chamber (V_{void}), excluding the volume occupied by the solid part of samples, is measured by gas which does not adsorb (e.g. helium). The V_{void} includes both the volume of the inter-particle space and the volume of pores.

B. The non-adsorptive gas is pumped out of the chamber and replaced with the probe gas, such as methane. The total molar number of probe gas (n_{total}) is

measured and also includes both the gas at the inter-particle space and inside the pores.

C. If there is no adsorption, the molar number of probe gas (n_{free}) required to reach the current pressure can be calculated as $n_{free} = V_{void} / V_{cham} \cdot n_{cham}^{cal}$, where V_{cham} is the chamber volume without any samples, and n_{cham}^{cal} is the calibration molar number of probe gas at the current pressure, which is measured before loading samples.

D. Then the excess gas due to adsorption can be calculated by

$$n_{excess} = n_{total} - n_{free} \tag{1.7}$$

For adsorption measurements of low-pressure gas, n_{excess} can be directly used as the amount of adsorption.

E. For adsorption measurements of high-pressure gas, the density of gas needs to take into account, so the absolute adsorbed amount $n_{absolute}$ is calculated by

$$n_{absolute} = \frac{n_{excess}}{1 - \rho_{\text{super}} / \rho_{ads}} \tag{1.8}$$

where ρ_{super} is the density of the gas, and ρ_{ads} is the density of adsorption state.

As such, the volumetric method can only measure the number of adsorbed particles (green dots in Figure 1.7E) rather than the total number stored inside pores. Therefore, some other techniques—such as NMR—are desired to determine the total amount of high-pressure gas stored inside pores.

1.4 NMR Principles

Nuclear Magnetic Resonance is a versatile and noninvasive analytical technic, which is suitable for characterizing porous materials. It can provide both the total quantity and the dynamic information of the molecules adsorbed inside the pores. The intensity of NMR

signal provides the total adsorption amount, and the relaxation measurements offer the dynamics information of molecules. Therefore, in the following sections, we briefly introduced the NMR theory.

1.4.1 1/2 Spin Ensemble System

Due to the *Zeeman Effect*, a single spin $1/2$ has two *Zeeman eigenstates* which obey the following eigenequations [23]:

$$\begin{aligned} \hat{I}_z|\alpha\rangle &= +\frac{1}{2}|\alpha\rangle \\ \hat{I}_z|\beta\rangle &= -\frac{1}{2}|\beta\rangle \end{aligned} \tag{1.9}$$

Equation 1.9 indicates that the state $|\alpha\rangle$ is an eigenstate of angular momentum along the z-axis, with eigenvalue $+1/2$. A spin that is in the state $|\alpha\rangle$ is called *polarized along the z-axis*. Similarly, the state $|\beta\rangle$ is called *polarized along the –z-axis* as shown in Figure 1.8.

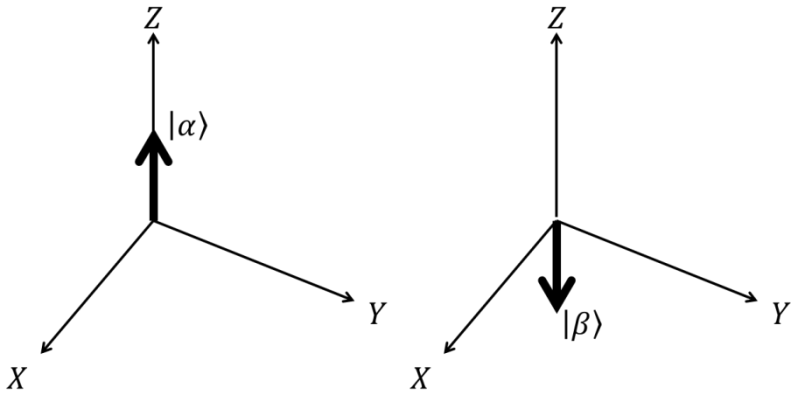

Figure 1.8 The two Zeeman eigenstates of a single spin 1/2.

If there is a magnetic field with magnitude B^0 along the z-axis, the spin Hamiltonian is proportional to $\hat{I}_z$ as shown in equation 1.10.

$$\hat{\mathbf{H}}^0 = \omega^0 \hat{I}_z \tag{1.10}$$

where the (chemical shifted) Larmor frequency is given by $\omega^0 = -\gamma B^0(1+\delta)$. The

eigenvalues and energies of states $|\alpha\rangle$ and $|\beta\rangle$ are $\pm\frac{1}{2}\omega^0$. The energy level splitting between the two states in a magnetic field is known as the *Zeeman splitting* and is equal to the Larmor frequency ω^0 (in units of $\hbar$) as shown in Figure 1.9.

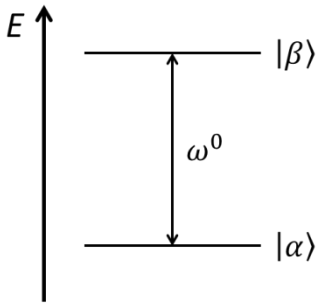

Figure 1.9 Energy levels for a spin 1/2 in a magnetic field.

Consider a 1/2 spin system under thermal equilibrium at temperature T, there is no transition between two states, the populations of the state $|r\rangle$ obey the *Boltzmann distribution*:

$$\rho_r^{\text{eq}} = \frac{\exp\left(-\hbar\omega_r / k_B T\right)}{\exp\left(-\hbar\omega_\alpha / k_B T\right) + \exp\left(-\hbar\omega_\beta / k_B T\right)} \tag{1.11}$$

where $k_B = 1.38066\times10^{-23}\,\text{JK}^{-1}$ is the *Boltzmann constant*. At room temperature, $k_B T \cong 4.1\times10^{-21}\,\text{J}$, and the energy difference between the Zeeman states of protons in a field of 4.7T (200MHz resonance frequency for protons) is $\left|\hbar\omega^0\right| \cong 1.3\times10^{-25}\,\text{J}$. Since the difference in energy between the Zeeman eigenstates is four orders of magnitude smaller than the available thermal energy, the thermal equilibrium population difference between the states is possible to estimate by an approximation of equation 1.11. The thermal equilibrium populations of the two states under *high-temperature approximation* are:

$$\rho_{\alpha}^{\mathrm{eq}} \cong \frac{1}{2} + \frac{1}{4} \cdot \Im$$
$$\rho_{\beta}^{\mathrm{eq}} \cong \frac{1}{2} - \frac{1}{4} \cdot \Im \tag{1.12}$$

where γ is the gyromagnetic ratio, $\Im = \hbar\gamma B^0 / k_B T$ is defined as *Boltzmann factor*. For positive γ, the low-energy $|\alpha\rangle$ state is populated slightly more than the high-energy $|\beta\rangle$ state, though the population difference is only about 1 part in 10^5.

1.4.2 Effects of $(\pi/2)_x$ and π_x Pulses

Under the rotation frame of reference frequency ω_{rot}, the spin states are related to the fixed-frame states through the transformation equation;

$$|\tilde{\psi}\rangle = \hat{R}_z\left(-\Phi(t)\right)|\psi\rangle \tag{1.13}$$

where

$$\Phi(t) = \omega_{\mathrm{ref}} t + \phi_{\mathrm{ref}} \tag{1.14}$$

and ω_{ref} is the reference frequency, equal to the frequency of the rotating frame. The operator $\hat{R}_z(-\Phi)$ generates a rotation around the z-axis, through the angle $-\Phi$.

Spin can be flipped by a strong radio frequency (RF) pulse of Larmor frequency, the spin-flip angle β_{P} is given by $\beta_{\mathrm{P}} = \omega_{\mathrm{nut}} \tau_{\mathrm{P}}$, where the nutation frequency ω_{nut} is a measure of the amplitude of the RF field, and τ_{P} is the pulse duration. The spin ensemble average ρ_{before} after the RF pulse β_{P} can be expressed as:

$$\hat{\rho}_{\mathrm{after}} = \hat{R}_{\phi_{\mathrm{P}}}(\beta_{\mathrm{P}})\,\hat{\rho}_{\mathrm{before}}\,\hat{R}_{\phi_{\mathrm{P}}}(-\beta_{\mathrm{P}}) \tag{1.15}$$

where ϕ_{P} is the phase of the pulse.

The effect of a strong $(\pi/2)_x$ pulse on an ensemble of non-interaction spins 1/2 in a state of thermal equilibrium can be expressed as (See *Levitt*'s book for more details [24]):

$$\hat{\rho}_{\text{before}} = \hat{\rho}^{\text{eq}} = \frac{1}{2}\hat{1} + \frac{1}{2}\Im\hat{I}_z$$
$$\hat{\rho}_{\text{after}} = \frac{1}{2}\hat{1} - \frac{1}{2}\Im\hat{I}_y \tag{1.16}$$

The $(\pi/2)_x$ pulse rotates the magnetization vector from the z-axis to –y-axis.

In terms of the matrix representations, the action of the pulse is as follows:

$$\hat{\rho}_{\text{before}} = \begin{pmatrix} \frac{1}{2} + \frac{1}{4}\Im & 0 \\ 0 & \frac{1}{2} - \frac{1}{4}\Im \end{pmatrix} \xrightarrow{(\pi/2)_X} \hat{\rho}_{\text{after}} = \begin{pmatrix} \frac{1}{2} & -\frac{1}{4\text{i}}\Im \\ \frac{1}{4\text{i}}\Im & \frac{1}{2} \end{pmatrix} \tag{1.17}$$

Therefore the $(\pi/2)_x$ pulse equalizes the populations of the two states and converts the population difference into coherences.

Similarly, the effect of a π_x pulse on the thermal equilibrium state can be expressed as:

$$\hat{\rho}_{\text{after}} = \frac{1}{2}\hat{1} - \frac{1}{2}\Im\hat{I}_z \tag{1.18}$$

Therefore, the π_x pulse accomplishes an inversion of the magnetization vector. In terms of population and coherence, it exchanges the populations of the two states as the transformation:

$$\hat{\rho}_{\text{before}} = \begin{pmatrix} \frac{1}{2} + \frac{1}{4}\Im & 0 \\ 0 & \frac{1}{2} - \frac{1}{4}\Im \end{pmatrix} \xrightarrow{\pi_x} \hat{\rho}_{\text{after}} = \begin{pmatrix} \frac{1}{2} - \frac{1}{4}\Im & 0 \\ 0 & \frac{1}{2} + \frac{1}{4}\Im \end{pmatrix} \tag{1.19}$$

1.4.3 Relaxation Theory

As mentioned in previous sections, RF pulses can disturb the equilibrium of the spin system. Relaxation is the process by which equilibrium is regained, through the interaction of the spin system with the thermal molecular environment. It can be divided into two types: *longitudinal relaxation* which is concerned with the movement of spin populations back to their Boltzmann distribution values and *transverse relaxation* which is concerned with the

decay of coherences.

In an ensemble of isolated spins $1/2$, there are only two time constants for the relaxation processes: *spin-lattice relaxation time constant* T_1 and *transverse relaxation time constant* T_2. Relaxations can be caused by fluctuating magnetic fields at the sites of the nuclear spins, which caused by thermal motion of the molecules. The *autocorrelation function* is introduced to define how rapidly the local magnetic fields are fluctuating as follow:

$$\mathbb{C}(\tau) = \langle B_x(t) B_x(t+\tau) \rangle \neq 0 \tag{1.20}$$

Here, τ is a time interval which is chosen on time scale of the local fluctuating magnetic field $B_x(t)$. Generally, a simple exponential form is assumed for the autocorrelation function:

$$\mathbb{C}(\tau) = \langle B_x^2 \rangle \mathrm{e}^{-|\tau|/\tau_C} \tag{1.21}$$

An important parameter in the relaxation theory is the spectral density $\mathbf{J}(\omega)$ which is defined as:

$$\begin{aligned} \mathbf{J}(\omega) &= 2\int_0^\infty \mathbb{C}(\tau) \exp(-\mathrm{i}\omega\tau)\,\mathrm{d}\tau \\ &= 2\langle B_x^2 \rangle J(\omega) \end{aligned} \tag{1.22}$$

where a normalized spectral density $J(\omega)$ is defined as:

$$J(\omega) = \frac{\tau_C}{1+\omega^2\tau_C} \tag{1.23}$$

The transition probabilities between states α and β for a single $1/2$ spin under the random field model are expressed by spectral density as following:

$$W_{-} = W_{+} = \frac{1}{2}\gamma^2 \left\langle B_x^2 \right\rangle J\left(\omega^0\right) \tag{1.24}$$

where W_{-} is the transition probabilities from state α to state β, vice versa. The transition probabilities in the two directions are predicted to be equal and are proportional to the spectral density of the random field at the Larmor frequency ω^0.

For a two spins system, the problem gets more complicated, and the detail of derivation is omitted here. It can be found in Levitt's book [23]. In summary, there are four quantum states, eight single-quantum transition probabilities, four double- and four zero- quantum transition probabilities as following:

$$\begin{aligned}
W_{+\alpha} = W_{+\beta} = W_{\alpha+} = W_{\beta+} &= W_1\left(1+\frac{1}{2}\mathbb{C}\right) \\
W_{-\alpha} = W_{-\beta} = W_{\alpha-} = W_{\beta-} &= W_1\left(1-\frac{1}{2}\mathbb{C}\right) \\
W_{++} &= W_2\left(1+\mathbb{C}\right) \\
W_{--} &= W_2\left(1-\mathbb{C}\right) \\
W_{+-} = W_{-+} &= W_0
\end{aligned} \tag{1.25}$$

Here W_1 , W_2 and W_0 are the *single-*, *double- and zero-quantum transition probabilities*, which are shown as following:

$$\begin{aligned}
W_1 &= \frac{3}{20} b^2 J\left(\omega^0\right) \\
W_2 &= \frac{3}{5} b^2 J\left(2\omega^0\right) \\
W_0 &= \frac{1}{10} b^2 J\left(0\right)
\end{aligned} \tag{1.26}$$

If the vibrational motions are ignored, the dipole-dipole coupling constant is given by

$$b = -\frac{\mu_0}{4\pi}\frac{\hbar\gamma^2}{r^3} \tag{1.27}$$

where the distance between the spins is denoted as r.

For a two spins ensemble system, the longitudinal relaxation time and transverse

relaxation time are given by:

$$T_1^{-1} = \frac{3}{10} b^2 \left\{ J\left(\omega^0\right) + 4J\left(2\omega^0\right) \right\}$$
$$T_2^{-1} = \frac{3}{20} b^2 \left\{ 3J\left(0\right) + 5J\left(\omega^0\right) + 2J\left(2\omega^0\right) \right\} \quad (1.28)$$

According to Equation 1.28, the T_2 relaxation times are dominated by the $J\left(0\right)$ and are therefore very sensitive to the low frequency or slow motion while the T_1 relaxation times are sensitive to the much higher Larmor frequency ($J\left(\omega^0\right)$ and $J\left(2\omega^0\right)$).

1.4.4 NMR Spectrum

When the ensemble of spins is excited by an RF pulse, the precessing nuclear transverse magnetization will induce an oscillating electric current which is called NMR signal or *free-induction decay* (FID) as shown in Figure 1.10 (A). The transverse magnetization components have the following form:

$$M_y^{\text{nuc}} = -M_{\text{eq}}^{\text{nuc}} \cos\left(\omega^0 t\right) \exp\left(-t/T_2\right)$$
$$M_x^{\text{nuc}} = M_{\text{eq}}^{\text{nuc}} \sin\left(\omega^0 t\right) \exp\left(-t/T_2\right) \quad (1.29)$$

The decay rates of both components are determined by *transverse relaxation time* T_2. The oscillating frequencies of both components are Larmor frequency ω^0. After Fourier transform, the FID signal can be transferred into the spectrum as shown in Figure 1.10 (B).

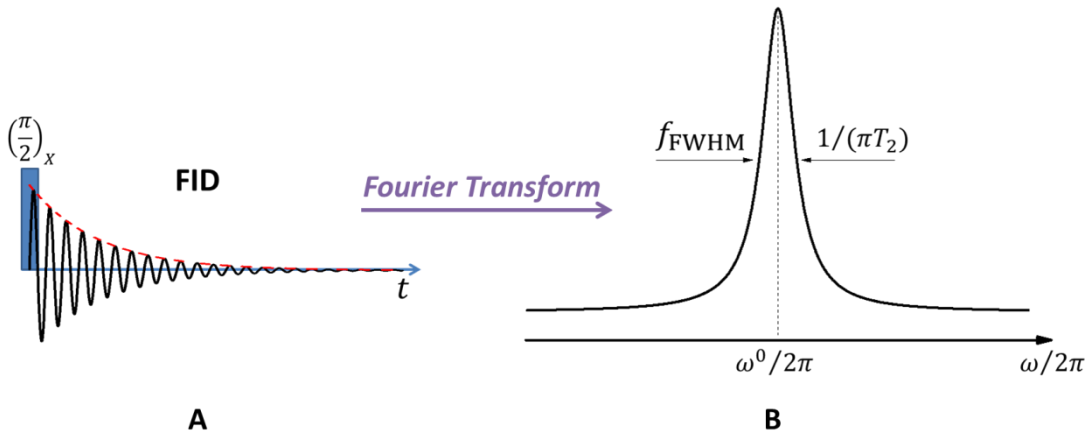

Figure 1.10 (A) The NMR FID signal and (B) The NMR spectrum.

The function of spectrum can be written as

$$S(\omega)=\frac{\lambda}{\lambda^2+\left(\omega-\omega^0\right)^2} \tag{1.30}$$

where the value of S is at a maximum when the frequency coordinate ω is equal to the Larmor frequency ω^0. The parameter λ is called the coherence decay rate constant. The *Full width at half maximum* (FWHM) f_{FWHM} is given as following:

$$f_{\mathrm{FWHM}}=\frac{\lambda}{\pi}=\frac{1}{\pi T_2} \tag{1.31}$$

However, the precise Larmor frequency of a given nucleus in the sample depends on a lot of factors in practice. Generally, if the Larmor frequency difference among the probing nucleus is caused by macroscopic factors, such as imperfect external magnetic field, field distortion from the bulk magnetic susceptibility of sample, and gradient field, it is called inhomogeneous broadening, as shown in Figure 1.11.

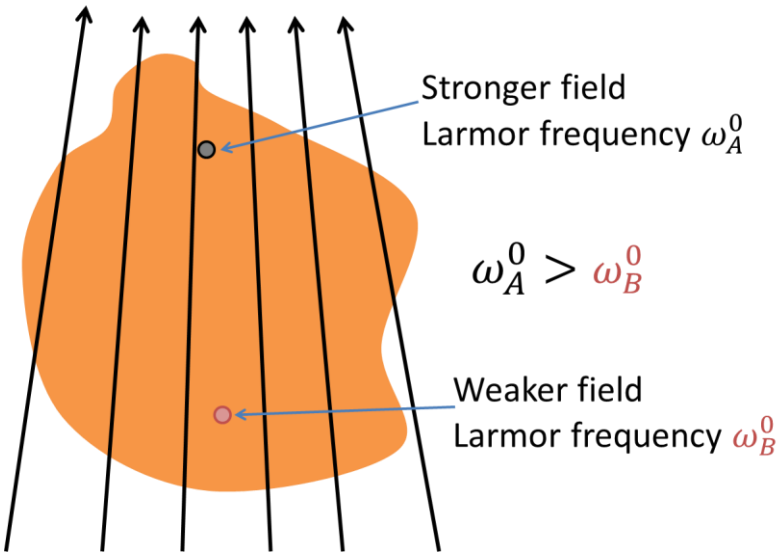

Figure 1.11 An illustration of inhomogeneous broadening.

The nuclear Larmor frequency also depends on the local electronic environment. This effect is called the *chemical shift*. The frequency difference can be observed in the spectrum as shown in Figure 1.12.

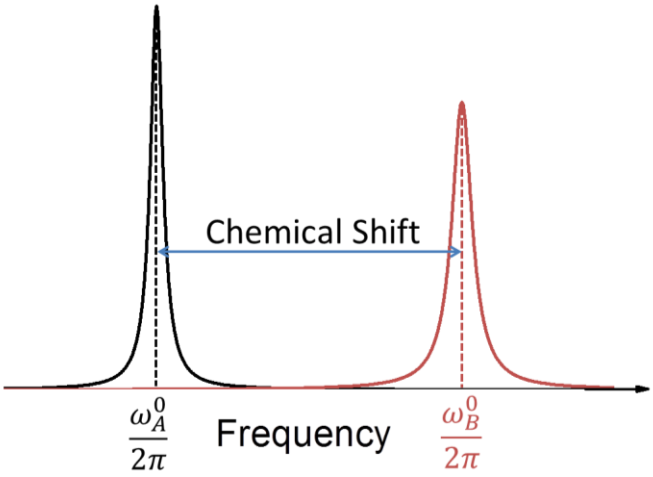

Figure 1.12 An illustration of *chemical shift*.

Because of the difference of Larmor frequency among the nucleus in the sample, the spin ensemble will lose the coherence faster and the decay time constant of FID, which is defined as T_2^*, generally is shorter than *transverse relaxation time* T_2 as shown in Figure 1.13.

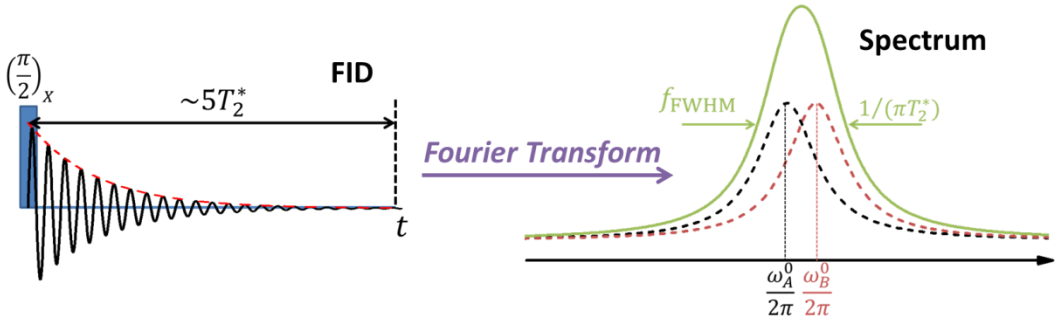

Figure 1.13 Illustrations of T_2^* and spectrum under broadening.

The FWHM of the spectrum f_{FWHM}^* is

$$f_{\mathrm{FWHM}}^* = 1/\left(\pi T_2^*\right) \tag{1.32}$$

1.4.5 NMR Pulse Sequences

In the FID experiment, a single 90° pulse is applied, as shown in Figure 1.13. After the 90° pulse, spin coherence on the x-y plane is generated. The FID signal is detected by RF coil and processed by the receiver. The "dead time" issues in FID measurements are

discussed in Section 3.5.1.

In the *longitudinal relaxation time* measurement, both the *inversion recovery* pulse sequence and the *saturation recovery* pulse sequence can be applied [25]. The pulse sequences are shown in Figure 1.14.

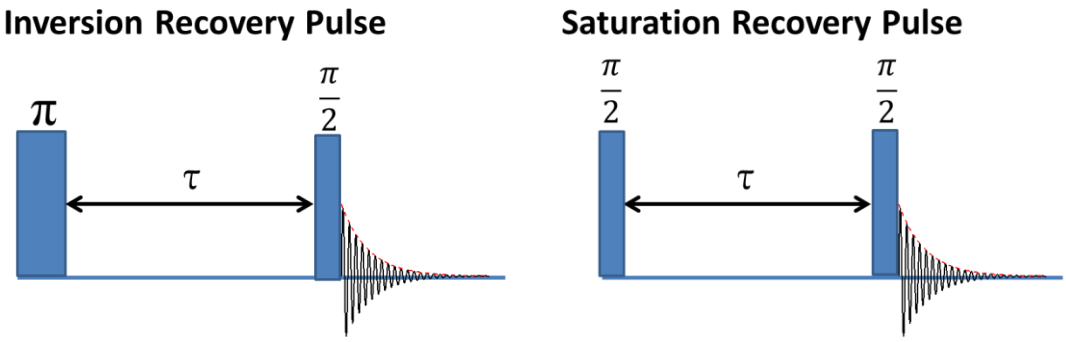

Figure 1.14 The *inversion recovery* pulse sequence and the *saturation recovery* pulse sequence

The magnetizations after waiting time τ are given by equation 1.33 for *inversion recovery* pulse and equation 1.34 for *saturation recovery* pulse.

$$M(\tau) = M_0\left(1-2\exp\left(-\tau/T_1\right)\right) \tag{1.33}$$

$$M(\tau) = M_0\left(1-\exp\left(-\tau/T_1\right)\right) \tag{1.34}$$

where M_0 is the amplitude of NMR signal.

In the *transverse relaxation* time measurement, there are also two common pulse sequences: the *Hahn Echo* pulse sequence and the *Carr-Purcell-Meiboom-Gill* (CPMG) pulse sequence as shown in Figure 1.15.

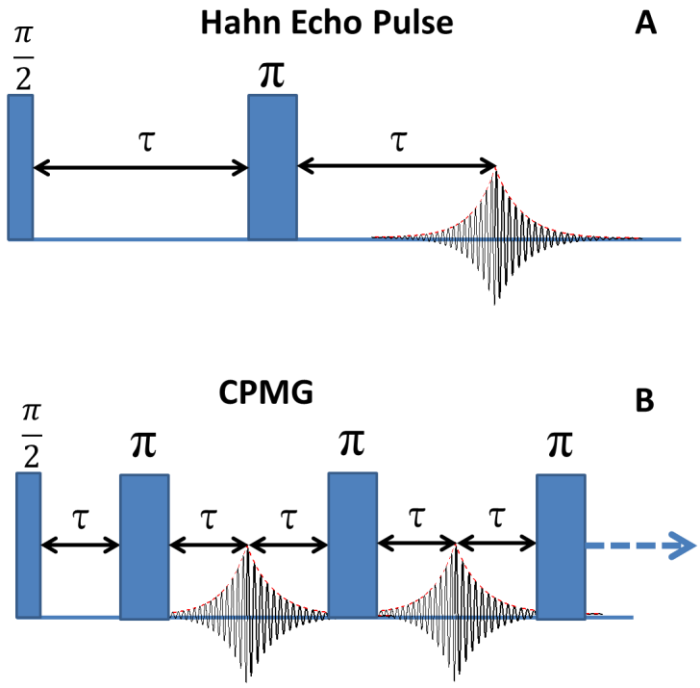

Figure 1.15 (A) The *Hahn Echo* pulse sequence and (B) The CPMG pulse sequence.

If the transverse relaxation is induced by diffusion through magnetic field gradient, it is given as

$$M(2\tau) = M(0)\exp\left(\frac{2\tau}{T_2}\right)\exp\left(-\left(\gamma\frac{\partial H}{\partial z}\right)^2\frac{2}{3}D\tau^3\right) \tag{1.35}$$

where D is the diffusion coefficient and $\partial H/\partial z$ is the gradient in a static field.

1.4.6 Magic-Angle Spinning

Mechanical sample rotation can be applied to reduce anisotropic spin interactions (quadrupole couplings, chemical shift anisotropies, and direct dipole-dipole couplings) [24]. In *magic-angle spinning* (MAS), the solid sample is rotated fast (several kHz to tens kHz) around an axis which subtends the 'magic angle' (54.74°) with respect to the static field, as shown in Figure 1.16.

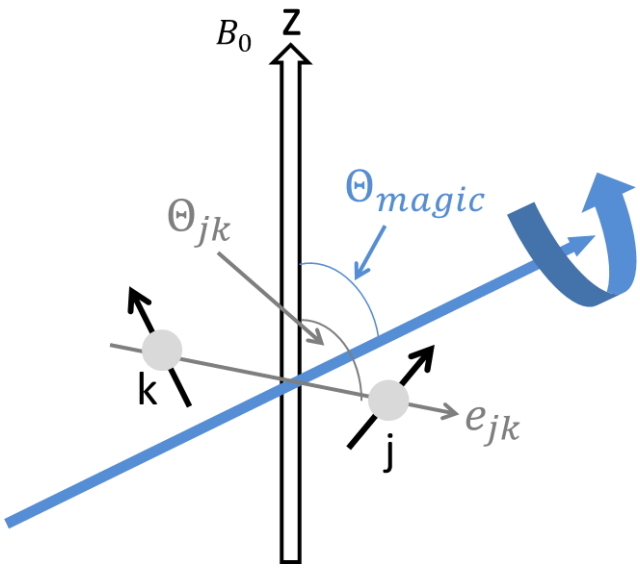

Figure 1.16 An illustration of MAS.

Considering a pair of spins with direct dipole-dipole coupling i and k, the secular part of the dipole-dipole coupling spin Hamiltonian is given by

$$\hat{\mathbf{H}}_{jk}^{\mathrm{DD}}\left(\Theta_{jk}\right) = d_{jk}\left(3\hat{I}_{jz}\hat{I}_{kz} - \hat{\mathbf{I}}_{\mathbf{j}}\cdot\hat{\mathbf{I}}_{\mathbf{k}}\right) \quad \text{(homonuclear case)} \tag{1.36}$$

where d_{ik} is the *secular dipole-dipole coupling*

$$d_{jk} = b_{jk}\frac{1}{2}\left(3\cos^2\Theta_{jk} - 1\right) \tag{1.37}$$

where is dipole-dipole the coupling constant. $\cos\Theta_{jk} = \mathbf{e}_{jk}\cdot\mathbf{e}_z$ is the angle between the vector joining the spins and the external magnetic field B_0 (along the z-axis). Therefore, in order to have the secular dipole-dipole coupling d_{jk} equal to zero, the *magic angle* can be calculated as:

$$3\cos^2\Theta_{jk} - 1 = 0 \tag{1.38}$$

$$\Theta_{\mathrm{magic}} = \arctan\sqrt{2} \cong 54.74^{\circ} \tag{1.39}$$

REFERENCES

[1] Lu GQ, Zhao XS, Wei TK. Nanoporous materials: science and engineering: Imperial College Press; 2004.

[2] Sing KSW, Everett DH, Haul RAW, Moscou L, Pierotti RA, Rouquerol J, et al. Reporting physisorption data for gas/solid systems, with special reference to the determination of surface area and porosity (recommendations 1984). Pure Appl Chem. 1985;57(4):603-19.

[3] Rodriguez-Reinoso F, Molina-Sabio M. Textural and chemical characterization of microporous carbons. Adv Colloid Interface Sci. 1998;76:271-94.

[4] Hutson ND, Yang RT. Theoretical basis for the Dubinin-Radushkevitch (D-R) adsorption isotherm equation. Adsorpt-J Int Adsorpt Soc. 1997;3(3):189-95.

[5] Lastoskie C, Gubbins KE, Quirke N. Pore size distribution analysis of microporous carbons: a density functional theory approach. Journal of Physical Chemistry. 1993;97(18):4786-96.

[6] Ryu ZY, Zheng JT, Wang MZ, Zhang BJ. Characterization of pore size distributions on carbonaceous adsorbents by DFT. Carbon. 1999;37(8):1257-64.

[7] Ravikovitch PI, Haller GL, Neimark AV. Density functional theory model for calculating pore size distributions: pore structure of nanoporous catalysts. Adv Colloid Interface Sci. 1998;76:203-26.

[8] Stevens P. The 'Shale Gas Revolution': Developments and Changes. Chatham house. 2012.

[9] Papaioannou A, Kausik R. Methane Storage in Nanoporous Media as Observed via High-Field NMR Relaxometry. Physical Review Applied. 2015;4(2):024018.

[10] Bae J-S, Bhatia SK. High-pressure adsorption of methane and carbon dioxide on coal. Energy & Fuels. 2006;20(6):2599-607.

[11] Brunauer S, Emmett PH, Teller E. Adsorption of gases in multimolecular layers. J Am Chem Soc. 1938;60(2):309-19.

[12] Dubinin M. Adsorption in micropores. Journal of Colloid and Interface Science. 1967;23(4):487-99.

[13] Dubinin M. Fundamentals of the theory of adsorption in micropores of carbon adsorbents: characteristics of their adsorption properties and microporous structures. Carbon. 1989;27(3):457-67.

[14] El-Merraoui M, Aoshima M, Kaneko K. Micropore size distribution of activated carbon fiber using the density functional theory and other methods. Langmuir. 2000;16(9):4300-4.

[15] Heller R, Zoback M. Adsorption of methane and carbon dioxide on gas shale and pure mineral samples. Journal of Unconventional Oil and Gas Resources. 2014;8:14-24.

[16] Sing KS. Adsorption methods for the characterization of porous materials. Adv Colloid Interface Sci. 1998;76:3-11.

[17] Langmuir I. The constitution and fundamental properties of solids and liquids. Journal of the Franklin Institute. 1917;183(1):102-5.

[18] DEBOER JH. The Dynamical Character of Adsorption: LWW; 1953.

[19] Barrett EP, Joyner LG, Halenda PP. The determination of pore volume and area distributions in porous substances. I. Computations from nitrogen isotherms. J Am Chem Soc. 1951;73(1):373-80.

[20] Bering B, Dubinin M, Serpinsky V. Theory of volume filling for vapor adsorption. Journal of Colloid and Interface Science. 1966;21(4):378-93.

[21] Sing KS. The use of physisorption for the characterization of microporous carbons. Carbon. 1989;27(1):5-11.

[22] Dubinin M. A study of the porous structure of active carbons using a variety of methods. Quarterly Reviews, Chemical Society. 1955;9(2):101-14.

[23] H.Levitt M. spin dynamics. Chichester, New York, Weinheim, Brisbane, Singapore, Toronto: John Wiley&Sons, Ltd; 2001.

[24] Levitt MH. Spin dynamics: basics of nuclear magnetic resonance: John Wiley & Sons; 2008.

[25] Fukushima E, Roeder SB. Experimental pulse NMR: a nuts and bolts approach: Addison-Wesley Reading, MA:; 1981.

CHAPTER 2. CHARACTERIZATION OF ACTIVATED CARBON NANOPOROUS STRUCTURES BASED ON NUCLEUS-INDEPENDENT CHEMICAL SHIFT

2.1 Introduction

Accurate determination of micropore size distribution is a challenging problem, especially of subnanometer-sized micropores. Besides the adsorption isotherm measurements, which have been discussed in Chapter 1, several NMR methods for characterizing PSD of ACs were also introduced, including NMR cryoporometry [1], relaxometry [2], and diffusometry [3]. NMR cryoporometry is based on the size-dependent depression of the melting temperature as described by the Gibbs-Thomson equation; this thermodynamic theory uses the macroscopic concept of surface tension and is applicable for pore sizes of a few nanometers and larger [4]. NMR relaxometry is based on separating the confined liquid into a bulk phase and a surface phase and is applicable to mesopores rather than micropores unless detailed information of the micropore geometry is available [5]. NMR diffusometry sheds light on the pore architectures related to the nature of the pore surface, diameter, and tortuosity and is not a technique exclusively for pore size determination [3, 6].

In this work, a quantitative NMR method is introduced based on taking a room temperature ^{1}H MAS NMR spectrum of a well-known quantity of water added to the ACs sample. This approach is made possible by DFT calculation of nucleus-independent chemical shift (NICS) [7], which establishes a quantitative relationship between the micropore size and NICS in ACs. This NICS NMR porometry technique applies to local internal surfaces that are graphitic-like and is particularly useful for determining pore size and pore size distribution of micropores (diameter less than 2 nm). It only requires taking one ^{1}H MAS spectrum of added

water and involves no additional knowledge such as interaction potentials or adsorption mechanisms.

2.1.1 Nucleus-Independent Chemical Shift

NICS is an aromatic ring current effect on the local magnetic field experienced by the nuclear spin of the probe atom. It is not related to any chemical bond and is thus nucleus independent. This chemical shift mechanism resulting from interatomic ring currents was known for a long time [8, 9], such as that of a benzene molecule [10]. The benzene molecule with cyclic conjugated π electrons has an induced ring current in the external magnetic field and gives rise to a diamagnetic response to the field above the plane of the benzene ring as shown in Figure 2.1, inducing an upfield chemical shift [9, 10].

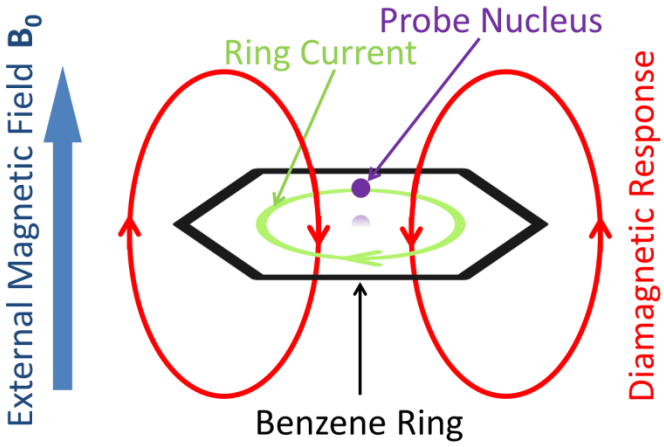

Figure 2.1 Illustration of diamagnetic response induced by Benzene molecule under external magnetic field.

The same effect was also observed in ^{1}H NMR spectrum by several different adsorbates on the surface of aromatic systems, such as hydrogen [11], water [12], ammonia [13] and so on. Since the chemical shift is from the diamagnetic and paramagnetic effects of the ring currents associated with aromatic and antiaromatic compounds, it is independent of the probe atoms. The substantial negative NICS values indicate the existence of a diatropic ring current [14]. Therefore the so-called NICS index is widely used for characterizing aromaticity and antiaromaticity [7, 14, 15].

2.1.2 Observation of NICS in ACs

As expected, there is also a large NICS effect in ACs. Figure 2.2 shows ^{1}H, ^{19}F, and ^{23}Na MAS spectra of a P-32 AC sample (see Section 2.4.2 for nomination rules) with added 1M $NaBF_4$ aqueous solution. Two well-resolved peaks are clearly observed in all three spectra. The ^{1}H chemical shift of the left peak, peak A, is due to water stored in large mesopores and macropores. It is slightly upfield shifted by -0.1 ppm compared to that of bulk water due to the isotropic bulk magnetic susceptibility effect. Since the whole sample space is experiencing the identical isotropic bulk magnetic susceptibility effect, it is suitable to use peak A as a reference for measuring the value of NICS. Setting the left peak chemical shift of all three nuclei as 0 ppm, the right peaks of all three nuclei exhibit the same chemical shift of -7.7 ppm. The right peak B is associated with water adsorbed inside micropores [12]. The upfield shift of peak B with respect to that of peak A is due to the NICS effect of ACs [8-10]. It is not related to any effect of chemical bonding as all three nuclei exhibit the same chemical shift.

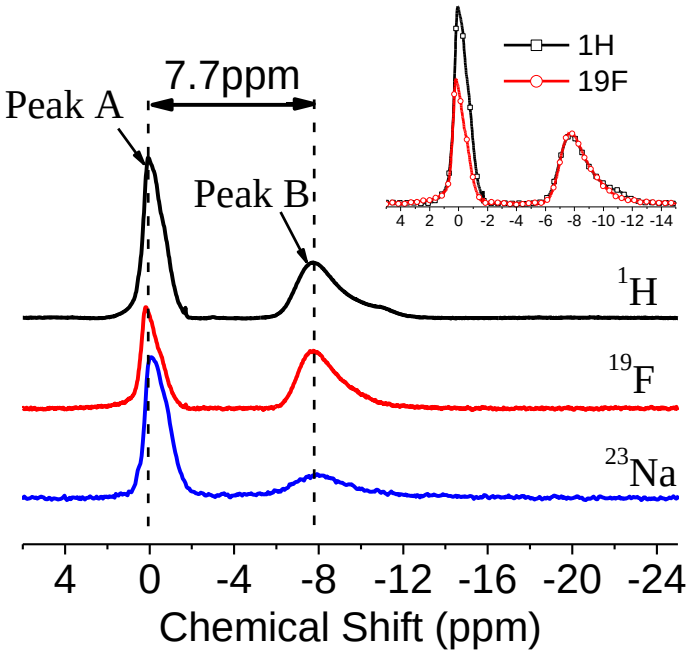

Figure 2.2 ^{1}H, ^{19}F, ^{23}Na MAS spectra of a P-32 AC sample filled with 1M $NaBF_4$ solution. The left peak A is set at 0 ppm, and the right peaks of all three nuclei exhibit the

same chemical shift of -7.7 ppm. Inset: ^{1}H and ^{19}F spectra were stacked together scaled in intensity according to peak B.

2.2 DFT Simulation of NICS

2.2.1 The Simulation Approach

All the DFT computation results were obtained by *Gaussian version 09-b01*[16]. *Gaussian* is an advanced computational chemistry software, which has been widely used in a lot of scientific areas [17]. It was initially released in 1970 by John Pople and his research group at Carnegie Mellow University [18]. It is a powerful tool to achieve first principle calculations [19] based on quantum mechanics.

Different from molecular mechanics methods which rely on force fields [20], first principle calculation solves the *Schrödinger Equations* usually under the assumption that nuclei are stationary. To achieve first principle calculations, *Gaussian* approximates the electron orbital shapes and electron orbital energies of a given molecular geometry by a model consisting of two parts: a *basis set* and a *method*.

The *basis set* applied in this work is *6-311G(d)* [21]. The first number "*6*" indicates the number of primitive Gaussians basis functions used for each core (inner) electron orbital; the following three digits "311" indicate how many sub-orbitals each valence atomic orbital is split into; and the character "*(d)*" indicates adding polarization basis functions. According to the online manual of *Gaussian*, *6-311G(d)* is sufficient for both ^{1}H and ^{12}C simulations.

The *method* used for geometry optimization is ***B3LYP*** (Becke, three-parameter, Lee-Yang-Parr) [22, 23], which is one of the most popular DFT methods used in computational chemistry. NICS values were computed by the *Gauge-Independent Atomic Orbital method*, which has been used a lot in previous studies [24-28].

A sample code of *Gaussian* is shown in Figure 2.3 as below:

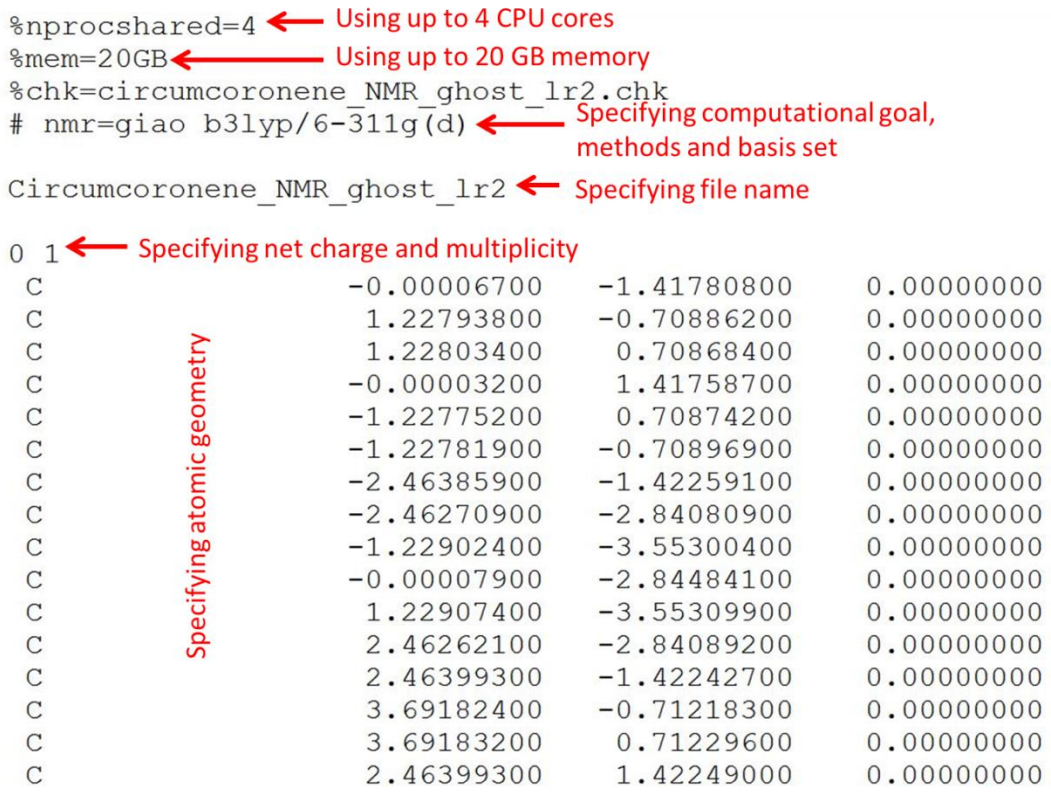

Figure 2.3 A sample code of the *Gaussian* software.

All the computational tasks are finished on *"KillDevil"* clusters supported by the *Information Technology Services* department of UNC.

2.2.2 The Simulation Model

The internal surface structure of ACs was mimicked by the central carbon ring of a circumcoronene molecule (as shown in Figure 2.4). The NICS probe atom (ghost atom [29]) was placed at three different locations, namely, over the center of the central carbon ring, over the top of the carbon atom of the central carbon ring, and over the middle point of the carbon-carbon bond of the central carbon ring, as illustrated in Figure 2.4 In each location, the NICS value is evaluated as a function of distance along the line perpendicular to the carbon surface.

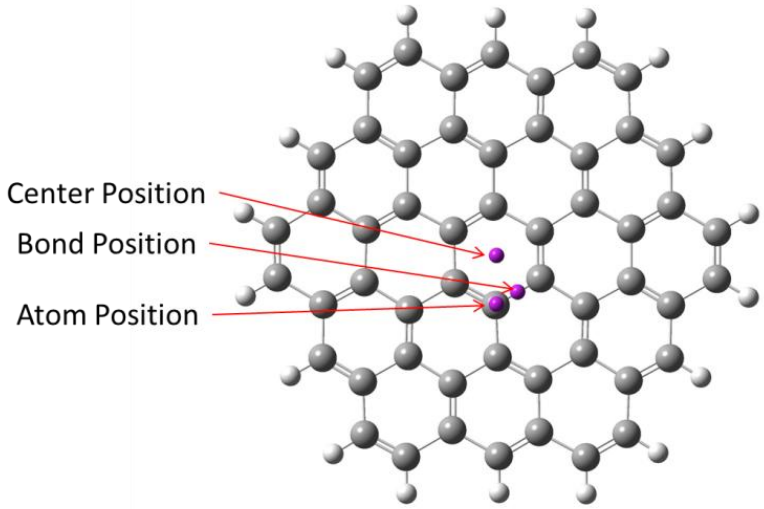

Figure 2.4 Molecular structure of circumcoronene. Gray atoms are carbon; white atoms are hydrogen. Purple dots are NICS probe atoms at three different locations.

2.2.3 The Simulation Scripts

The *Gaussian* script of geometry optimization is shown as below:

```
%nprocshared=4
%mem=20GB
%chk=circumcoronene.chk
# opt freq b3lyp/6-311g(d)

Circumcoronene_opt

0 1
 C                    -0.02875967    -1.44714823     0.00000000
 C                    -1.21615756    -0.80932756     0.00000000
 C                    -1.25638248     0.71508659     0.00000000
 C                    -0.09556602     1.42597309     0.00000000
 C                     1.25896766     0.69631033     0.00000000
 C                     1.27701089    -0.66810344     0.00000000
 C                     2.58076382    -1.48017055     0.00000000
 C                     2.54300326    -2.84052536     0.00000000
 C                     1.21201991    -3.61120499     0.00000000
 C                     0.02932816    -2.96572048     0.00000000
 C                    -1.28035576    -3.73365568     0.00000000
 C                    -2.57492264    -2.93088024     0.00000000
 C                    -2.54447119    -1.57953704     0.00000000
 C                    -3.85017493    -0.78019704     0.00000000
 C                    -3.79277561     0.75840543     0.00000000
 C                    -2.61225533     1.43562444     0.00000000
 C                    -2.60346578     2.95858981     0.00000000
 C                    -1.25316198     3.66869797     0.00000000
```

C	-0.09684700	2.96266835	0.00000000
C	1.25079557	3.69581040	0.00000000
C	2.56253387	2.88442417	0.00000000
C	2.57392073	1.51813903	0.00000000
C	3.92119588	0.77592411	0.00000000
C	3.92132154	-0.75238956	0.00000000
C	5.07923016	-1.44724888	0.00000000
C	5.04367451	-2.99390177	0.00000000
C	3.84716120	-3.64653917	0.00000000
C	3.79205267	-5.19562563	0.00000000
C	2.60166242	-5.87920702	0.00000000
C	1.23937433	-5.14321269	0.00000000
C	0.06371972	-5.84261120	0.00000000
C	-1.29098386	-5.08701969	0.00000000
C	-2.63795586	-5.86762143	0.00000000
C	-3.84631123	-5.21702949	0.00000000
C	-3.89649166	-3.67715573	0.00000000
C	-5.06850909	-2.98334586	0.00000000
C	-5.04784738	-1.43136238	0.00000000
C	-6.38737462	-0.64248169	0.00000000
C	-6.41824975	0.72462902	0.00000000
C	-5.10816833	1.53021613	0.00000000
C	-5.10696970	2.89272559	0.00000000
C	-3.76422559	3.66238594	0.00000000
C	-3.75370814	5.21732070	0.00000000
C	-2.58306423	5.92635081	0.00000000
C	-1.23302599	5.18815859	0.00000000
C	-0.04872485	5.85288446	0.00000000
C	1.28158968	5.06073544	0.00000000
C	2.62586802	5.83733346	0.00000000
C	3.82725411	5.19249380	0.00000000
C	3.88208770	3.65752183	0.00000000
C	5.07026031	2.99806880	0.00000000
C	5.08820462	1.45626376	0.00000000
C	6.42258136	0.67948390	0.00000000
C	6.41861212	-0.68220017	0.00000000
H	5.95742693	-3.55063776	0.00000000
H	4.70839866	-5.74808222	0.00000000
H	2.61553707	-6.94911670	0.00000000
H	0.07864047	-6.91250891	0.00000000
H	-2.62119862	-6.93749046	0.00000000
H	-4.75585399	-5.78061805	0.00000000
H	-6.00156478	-3.50708467	0.00000000
H	-7.31026769	-1.18392788	0.00000000
H	-7.35805635	1.23615939	0.00000000
H	-6.03254401	3.42957763	0.00000000
H	-4.68413451	5.74571851	0.00000000
H	-2.60671215	6.99608996	0.00000000
H	-0.03502157	6.92279669	0.00000000
H	2.60914698	6.90720177	0.00000000

H	4.73554720	5.75809236	0.00000000
H	5.98917249	3.54624336	0.00000000
H	7.35096000	1.21147371	0.00000000
H	7.34323589	-1.22068975	0.00000000

The *Gaussian* script of NMR calculation is shown as below:

```
%nprocshared=4
%mem=20GB
%chk=circumcoronene_NMR_ghost_lr2.chk
# nmr=giao b3lyp/6-311g(d)

Circumcoronene_NMR_ghost_lr2

0 1
```

C	-0.00006700	-1.41780800	0.00000000
C	1.22793800	-0.70886200	0.00000000
C	1.22803400	0.70868400	0.00000000
C	-0.00003200	1.41758700	0.00000000
C	-1.22775200	0.70874200	0.00000000
C	-1.22781900	-0.70896900	0.00000000
C	-2.46385900	-1.42259100	0.00000000
C	-2.46270900	-2.84080900	0.00000000
C	-1.22902400	-3.55300400	0.00000000
C	-0.00007900	-2.84484100	0.00000000
C	1.22907400	-3.55309900	0.00000000
C	2.46262100	-2.84089200	0.00000000
C	2.46399300	-1.42242700	0.00000000
C	3.69182400	-0.71218300	0.00000000
C	3.69183200	0.71229600	0.00000000
C	2.46399300	1.42249000	0.00000000
C	2.46280300	2.84096900	0.00000000
C	1.22907600	3.55306200	0.00000000
C	-0.00002500	2.84478000	0.00000000
C	-1.22914700	3.55302200	0.00000000
C	-2.46277500	2.84068400	0.00000000
C	-2.46402400	1.42252800	0.00000000
C	-3.69184500	0.71210700	0.00000000
C	-3.69182400	-0.71225500	0.00000000
C	-4.92579700	-1.43113700	0.00000000
C	-4.90201000	-2.82986600	0.00000000
C	-3.70277800	-3.55020500	0.00000000
C	-3.66388100	-4.98568100	0.00000000
C	-2.48591000	-5.66562600	0.00000000
C	-1.22326700	-4.98144100	0.00000000
C	0.00036500	-5.65982700	0.00000000
C	1.22345000	-4.98114000	0.00000000
C	2.48560000	-5.66544100	0.00000000
C	3.66368000	-4.98541100	0.00000000

C	3.70237500	-3.55017800	0.00000000
C	4.90209400	-2.82956300	0.00000000
C	4.92605000	-1.43126000	0.00000000
C	6.14968400	-0.68009600	0.00000000
C	6.14978000	0.68005500	0.00000000
C	4.92611300	1.43135000	0.00000000
C	4.90202400	2.83042600	0.00000000
C	3.70250700	3.55038500	0.00000000
C	3.66385600	4.98562300	0.00000000
C	2.48580500	5.66565000	0.00000000
C	1.22355700	4.98136300	0.00000000
C	-0.00039800	5.66005300	0.00000000
C	-1.22344700	4.98132600	0.00000000
C	-2.48591000	5.66548700	0.00000000
C	-3.66379000	4.98555900	0.00000000
C	-3.70277100	3.55014500	0.00000000
C	-4.90219000	2.82981800	0.00000000
C	-4.92616900	1.43097000	0.00000000
C	-6.14951500	0.67979900	0.00000000
C	-6.14931500	-0.68040100	0.00000000
H	-5.84345800	-3.37278000	0.00000000
H	-4.60537500	-5.52702100	0.00000000
H	-2.48403100	-6.75165500	0.00000000
H	0.00075000	-6.74656300	0.00000000
H	2.48350400	-6.75141600	0.00000000
H	4.60511800	-5.52679300	0.00000000
H	5.84327000	-3.37291600	0.00000000
H	7.08928700	-1.22470800	0.00000000
H	7.08938300	1.22465700	0.00000000
H	5.84317100	3.37381700	0.00000000
H	4.60537400	5.52685200	0.00000000
H	2.48385300	6.75166000	0.00000000
H	-0.00029100	6.74681000	0.00000000
H	-2.48385500	6.75150300	0.00000000
H	-4.60524500	5.52698100	0.00000000
H	-5.84352600	3.37297000	0.00000000
H	-7.08921000	1.22419100	0.00000000
H	-7.08872600	-1.22526100	0.00000000
Bq	0.00000000	0.00000000	0.00000000
Bq	0.00000000	0.00000000	0.50000000
Bq	0.00000000	0.00000000	1.00000000
Bq	0.00000000	0.00000000	1.50000000
Bq	0.00000000	0.00000000	2.00000000
Bq	0.00000000	0.00000000	2.50000000
Bq	0.00000000	0.00000000	3.00000000
Bq	0.00000000	0.00000000	3.50000000
Bq	0.00000000	0.00000000	4.00000000
Bq	0.00000000	0.00000000	4.50000000
Bq	0.00000000	0.00000000	5.00000000
Bq	0.00000000	0.00000000	5.50000000

Bq	0.00000000	0.00000000	6.00000000
Bq	0.00000000	0.00000000	6.50000000
Bq	0.00000000	0.00000000	7.00000000
Bq	0.00000000	0.00000000	7.50000000
Bq	0.00000000	0.00000000	8.00000000
Bq	0.00000000	0.00000000	8.50000000
Bq	0.00000000	0.00000000	9.00000000
Bq	0.00000000	0.00000000	9.50000000
Bq	0.00000000	0.00000000	10.00000000
Bq	0.00000000	0.00000000	11.00000000
Bq	0.00000000	0.00000000	12.00000000
Bq	0.00000000	0.00000000	13.00000000
Bq	0.00000000	0.00000000	14.00000000
Bq	0.00000000	0.00000000	15.00000000
Bq	0.00000000	0.00000000	16.00000000
Bq	0.00000000	0.00000000	17.00000000
Bq	0.00000000	0.00000000	18.00000000
Bq	0.00000000	0.00000000	19.00000000
Bq	0.00000000	0.00000000	20.00000000
Bq	0.00000000	0.00000000	25.00000000
Bq	0.00000000	0.00000000	30.00000000
Bq	0.00000000	0.00000000	35.00000000
Bq	0.00000000	0.00000000	40.00000000
Bq	0.00000000	0.00000000	45.00000000
Bq	0.00000000	0.00000000	50.00000000
Bq	-0.00006700	-1.41780800	3.00000000
Bq	-0.00006700	-1.41780800	3.50000000
Bq	-0.00006700	-1.41780800	4.00000000
Bq	-0.00006700	-1.41780800	4.50000000
Bq	-0.00006700	-1.41780800	5.00000000
Bq	-0.00006700	-1.41780800	5.50000000
Bq	-0.00006700	-1.41780800	6.00000000
Bq	-0.00006700	-1.41780800	6.50000000
Bq	-0.00006700	-1.41780800	7.00000000
Bq	-0.00006700	-1.41780800	7.50000000
Bq	-0.00006700	-1.41780800	8.00000000
Bq	-0.00006700	-1.41780800	8.50000000
Bq	-0.00006700	-1.41780800	9.00000000
Bq	-0.00006700	-1.41780800	9.50000000
Bq	-0.00006700	-1.41780800	10.00000000
Bq	-0.00006700	-1.41780800	11.00000000
Bq	-0.00006700	-1.41780800	12.00000000
Bq	-0.00006700	-1.41780800	13.00000000
Bq	-0.00006700	-1.41780800	14.00000000
Bq	-0.00006700	-1.41780800	15.00000000
Bq	-0.00006700	-1.41780800	16.00000000
Bq	-0.00006700	-1.41780800	17.00000000
Bq	-0.00006700	-1.41780800	18.00000000
Bq	-0.00006700	-1.41780800	19.00000000
Bq	-0.00006700	-1.41780800	20.00000000

Bq	-0.00006700	-1.41780800	25.00000000
Bq	-0.00006700	-1.41780800	30.00000000
Bq	-0.00006700	-1.41780800	35.00000000
Bq	-0.00006700	-1.41780800	40.00000000
Bq	-0.00006700	-1.41780800	45.00000000
Bq	-0.00006700	-1.41780800	50.00000000
Bq	0.61393550	-1.06333500	2.00000000
Bq	0.61393550	-1.06333500	2.50000000
Bq	0.61393550	-1.06333500	3.00000000
Bq	0.61393550	-1.06333500	3.50000000
Bq	0.61393550	-1.06333500	4.00000000
Bq	0.61393550	-1.06333500	4.50000000
Bq	0.61393550	-1.06333500	5.00000000
Bq	0.61393550	-1.06333500	5.50000000
Bq	0.61393550	-1.06333500	6.00000000
Bq	0.61393550	-1.06333500	6.50000000
Bq	0.61393550	-1.06333500	7.00000000
Bq	0.61393550	-1.06333500	7.50000000
Bq	0.61393550	-1.06333500	8.00000000
Bq	0.61393550	-1.06333500	8.50000000
Bq	0.61393550	-1.06333500	9.00000000
Bq	0.61393550	-1.06333500	9.50000000
Bq	0.61393550	-1.06333500	10.00000000
Bq	0.61393550	-1.06333500	11.00000000
Bq	0.61393550	-1.06333500	12.00000000
Bq	0.61393550	-1.06333500	13.00000000
Bq	0.61393550	-1.06333500	14.00000000
Bq	0.61393550	-1.06333500	15.00000000
Bq	0.61393550	-1.06333500	16.00000000
Bq	0.61393550	-1.06333500	17.00000000
Bq	0.61393550	-1.06333500	18.00000000
Bq	0.61393550	-1.06333500	19.00000000
Bq	0.61393550	-1.06333500	20.00000000
Bq	0.61393550	-1.06333500	25.00000000
Bq	0.61393550	-1.06333500	30.00000000
Bq	0.61393550	-1.06333500	35.00000000
Bq	0.61393550	-1.06333500	40.00000000
Bq	0.61393550	-1.06333500	45.00000000
Bq	0.61393550	-1.06333500	50.00000000

2.2.4 The Simulation Results

The function $\delta(r)$ is the NICS value as a function of the distance between the probe atom center and the surface of carbons (atomic center to center). This function can be obtained from the DFT calculation [29-31]. Here we use the central carbon ring of the circumcoronene molecule to model the effect of AC micropore surface (Figure 2.4). The

shielding tensor of NICS can then be calculated using the DFT method at the position specified by the NICS probe atom. The calculated result of $\delta(r)$ is shown in Figure 2.5. The NICS at locations over the center of the central aromatic ring, over the carbon atom, and over the middle of the carbon-carbon bond are nearly identical when the distance *r* is larger than 0.32 nm. Since atoms of water molecules would not approach the surface closer than this distance, we assume $\delta(r)$ to be the independence of the horizontal position over a graphitic-like surface. For the purpose of convenience for future usage of the calculated $\delta(r)$, we fit the calculated $\delta(r)$ in the region of $0.3\ \text{nm} \le r \le 3.0\ \text{nm}$ with a stretched exponential function $\delta(r) = A\exp\left[-(r/r_0)^{\beta}\right]$. There is no any physical meaning in this functional form of the fitting. It is simply for the purpose of reading off the values of the DFT computational result. A very good fit is obtained with $A = 24.5\ \text{ppm}$, $r_0 = 0.227\ \text{nm}$, and $\beta = 0.754$ as shown in Figure 2.5.

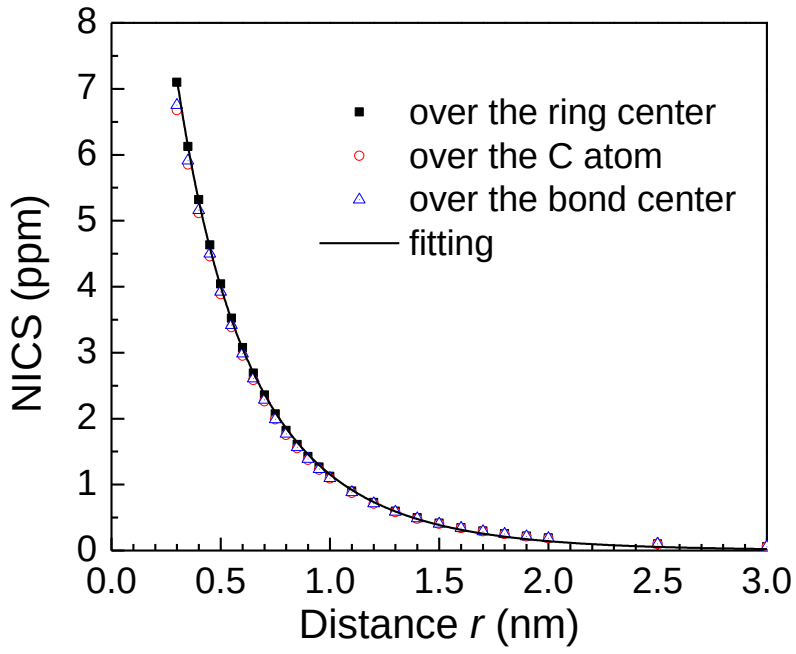

Figure 2.5 Calculated NICS $\delta(r)$ by DFT with the probe atom over the ring center,

over the carbon atom, and over the bond center of the central carbon ring of circumcoronene. The solid line is an empirical fit of the numerical $\delta(r)$ with $\delta(r) = A\exp\left[-(r/r_0)^{\beta}\right]$.

2.3 Probing Microporous ACs

2.3.1 Slit-Shaped Pore Model and Average NICS

A simple exchange model is assumed to correlate NICS-related isotropic chemical shift with the pore size. As it is shown in Figure 2.6, inside a slit-shaped pore [32], water molecules are distributed throughout the internal space. On the NMR timescale of 600 μs, a water molecule moves rapidly inside the micropore and spends time both close to (small *r*) and away from (large *r*) the surface. Therefore, the measured NMR spectrum is determined by the time-averaged effect of motion. Since the NICS is a function of distance from the surface, as shown in Figure 2.5, the measured NICS-related isotropic chemical shift of a fully filled micropore is NICS averaged over the pore space and can be calculated as

$$\delta_{avg}(d) = \frac{\int_{w}^{d-w}\delta(r)dr}{\int_{w}^{d-w}dr} + \frac{\int_{w}^{d-w}\delta(d-r)dr}{\int_{w}^{d-w}dr} = 2\frac{\int_{w}^{d-w}\delta(r)dr}{\int_{w}^{d-w}dr} \tag{2.1}$$

where δ_{avg} is the averaged NICS, *d* is the pore width between the two layers of carbon atoms (atom center to center), and *w* is the closest distance between hydrogen and carbon atoms chosen as *w*=0.32 nm [11]. NICS contributions from both surfaces are taken into account in Equation (2.1).

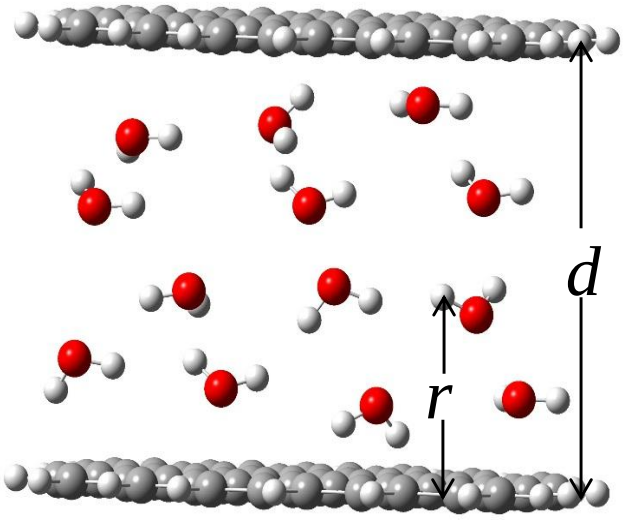

Figure 2.6 Illustration of water molecules inside a slit-shaped pore of width d (atom center to center).

2.3.2 Correlation of Isotropic Chemical Shift and Pore Size

By plugging $\delta(r) = A\exp\left[-(r/r_0)^{\beta}\right]$ with $A = 24.5$ ppm, $r_0 = 0.227$ nm, and $\beta = 0.754$ into Equation 2.1 and with w=0.32 nm, the averaged NICS δ_{avg} can then be calculated as a function of pore size d by

$$\delta_{avg}(d) = \frac{2A}{d-2w}\int_{w}^{d-w} e^{-(r/r_0)^{\beta}}\,dr \tag{2.2}$$

The function in Equation 2.2 can be inverted numerically to obtain the function of pore size d versus δ_{avg} and this numerical result is shown in Figure 2.7. Again, for convenience of future usage, the numerical result of d versus δ_{avg} is fitted empirically with the following function

$$d = A_1\exp\left(-\delta_{avg}/\delta_1\right) + A_2\exp\left(-\delta_{avg}/\delta_2\right) + d_0 \tag{2.3}$$

with the fitting parameters $\delta_1 = -0.53$ ppm, $\delta_2 = -3.7$ ppm, $A_1 = 16.15$ nm, $A_2 = 3.82$ nm, and $d_0 = 0.57$ nm. As shown in Figure 2.7, this fit is excellent. Figure 2.7 shows that water contained in mesopores larger than 3 nm would contribute to peak A rather than peak B. Peak B belongs predominantly to water contained in micropores ($d \le 2$ nm).

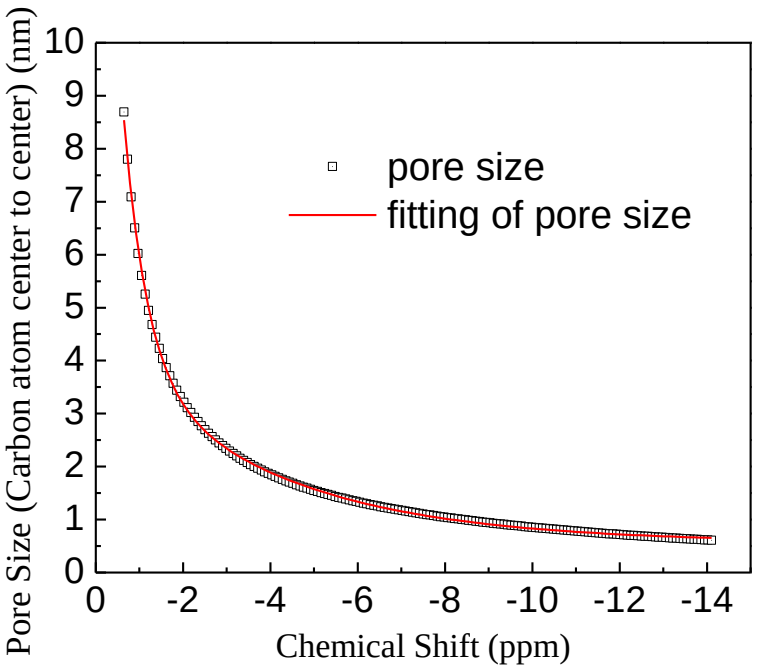

Figure 2.7 For a slit-shaped pore of width *d* (atom center to center), the deduced function of *d* versus the averaged NICS δ_{avg} based on Equation 2.2. The solid line is an empirical fit of the numerical result with a function given by Equation 2.3.

2.3.3 Micropore Filling

Complete micropore filling is essential for the application of this model, especially for large micropores. Figure 2.8a compares ^{1}H MAS NMR spectrum of a P-0 sample with adsorbed water under saturated water vapor for 20 hours with that by syringe water injection. The mass ratio of adsorbed water to AC after 20 hours exposure to saturated water vapor is 0.19. Its spectrum shows a single peak B and water is only adsorbed into micropores. The external surface is hydrophobic, and no significant water condensation happens. The internal surfaces of all accessible micropores have graphitic-like surface structures giving rise to nearly identical NICS. After the mass ratio of water to carbon is increased to 0.39 by further water addition with syringe water injection into the P-0 sample that already has 0.19 water to AC mass ratio, Peak A emerges, but peak B remains identical. Therefore, the micropores have already been fully filled with water by 20 hours exposure to saturated water vapor. The additionally injected water only goes to large mesopores and macropores giving rise to Peak

A. For comparison, water is also injected into a dry P-0 AC sample directly, and the spectrum shown in Figure 2.8a shows an identical peak B as that after 20 hours exposure to saturated water vapor. Thus, the water injection method also provides fully filled micropores with water. Figure 2.8b shows ^{1}H MAS NMR spectra of a P-92 AC sample filled with different amount of water by syringe water injection. Here, peak B appears first and grows in intensity as the amount of adsorbed water increases. After the mass ratio of water to carbon reaches 1.42, peak A starts to emerge while peak B stops growing. Notice in Figure 2.8b that peak B shifts gradually toward the lower field as its intensity increases with increasing water filling. The difference of chemical shifts between initial water filling and pore saturation is about 0.7 ppm. When a small amount of water is initially added into micropores, water molecules preferentially adsorb on the surface and spend, on average, more time near the surface where the NICS effect is large. With more water added, the pore space is gradually filled up and water distribution averaged over time is close to that of the volume average used in Equation 2.1. Therefore, the measured NICS-related isotropic chemical shift (shift of peak B with respect to the shift of peak A) of a fully filled micropore would have a less negative value (lower field) compared to that of a partially filled micropore, as shown in Figure 2.8b.

a

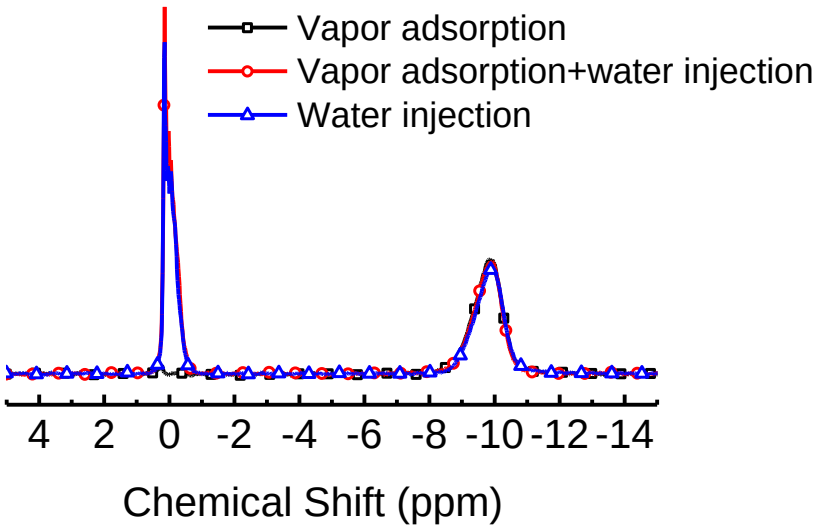

b

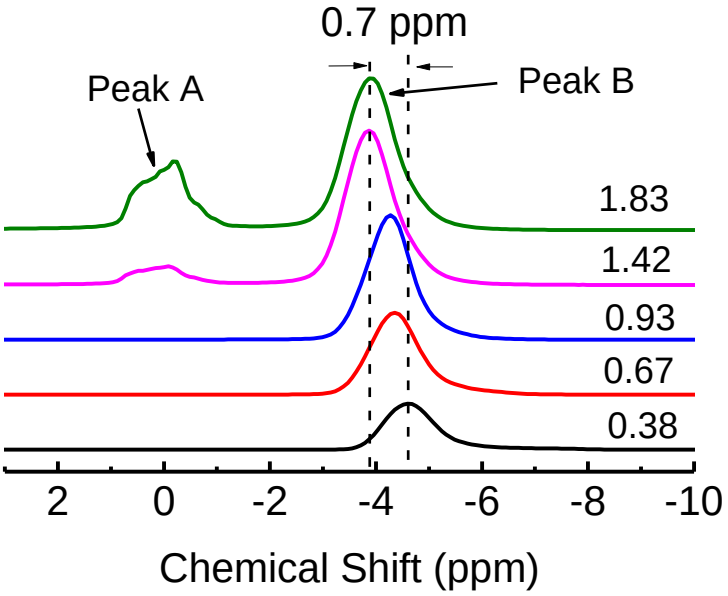

Figure 2.8 (a) ^{1}H MAS spectra of water in a P-0 AC sample with different water filling condition: Adsorption in saturate water vapor (square) followed by further water addition with syringe water injection (circle); adsorption by syringe injection into a dry AC sample (triangle). All three spectra have identical Peak B certifying the micropores were fully filled by each method. (b) ^{1}H MAS spectra of water in a P-92 AC sample at different water filling level with water/carbon mass ratio ranging from 0.38 to 1.83. The chemical shift of peak B at low filling level (0.38) differs by 0.7 ppm from that of saturated micropores (mass ratio 1.42 and above).

2.3.4 Micropore Volume in ACs

The amount of water adsorbed inside micropores can be measured quantitatively by NMR and can be used to calculate the micropore volume. Since ^{1}H MAS NMR spectra (Figures 2.2 and 2.8) clearly resolve the peak associated with micropores from the peak associated with the rest of the water, the amount of water inside micropores can be easily determined from the known amount of added water and the ratio of peak B intensity versus the total spectral intensity. The total micropore volume per unit mass of AC sample, V_B / m_s, can be calculated by

$$\frac{V_B}{m_s} = \frac{1}{\rho_w} \cdot \frac{A_B}{A_{total}} \cdot \frac{m_w}{m_s} \tag{2.4}$$

where m_w and m_s are the mass of water and AC sample, respectively, $\rho_w = 0.9$ g/cm^3 is the density of water inside micropores [33], A_{total} is the total spectral intensity, and A_B is the intensity of peak B.

Since the pore size *d* as a function of δ_{avg} is established, it is straightforward to obtain the dominant pore size of micropores in an AC sample by determining δ_{avg} of peak B. ^{1}H spectra of water filled ACs samples derived from PEEK with different BO values are shown in Figure 2.9. Table 2.1 summarizes the information extracted from the spectra including the measured δ_{avg} and the corresponding pore size *d*, as well as the micropore volume and micropore surface area. The pore width defined as the surface to surface distance d^* is determined by $d^* = d - 0.34$ nm where the carbon atom diameter of 0.34 nm is from the solid-solid Lennard-Jones interaction parameter [34]. The micropore internal surface area is calculated from pore volume and pore width d^* by

$$S = \frac{2V_B}{m_s \cdot d^*} \tag{2.5}$$

The 92% and 0% BO AC samples were also characterized by nitrogen adsorption

isotherm and showed a typical Type I adsorption isotherm (Section 2.4.4) which indicated the dominated pore type is micropores.

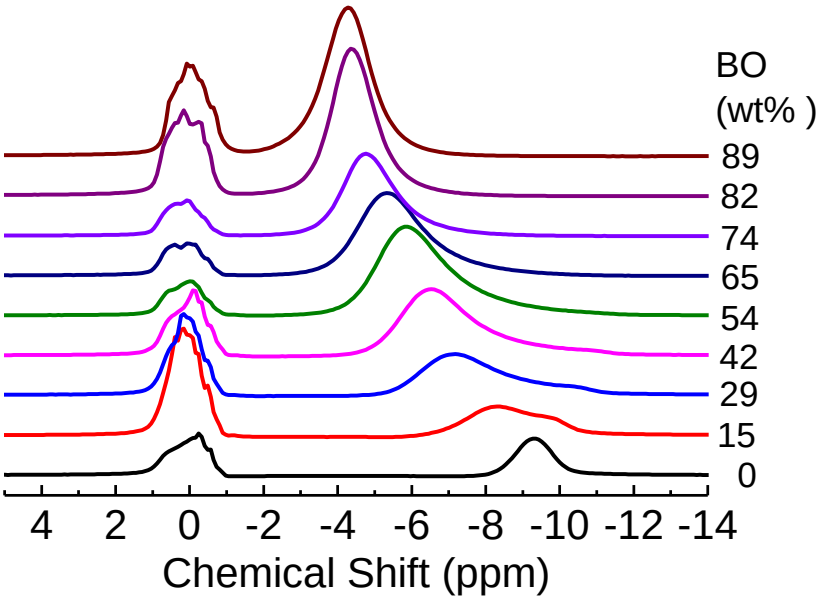

Figure 2.9 ^{1}H MAS spectra of water-filled AC samples derived from PEEK with different BO values as indicated in the figure.

The BET area and total pore volume of 92% BO sample are $2888\ m^2/g$ and $1.55\ cm^3/g$ (at P/P_0=0.99), respectively (Section 2.4.4). The 0% BO sample has $0.18\ cm^3/g$ total pore volume (at P/P_0=0.99). The micropore volume calculated by the MAS NMR method matches very well with nitrogen adsorption method in both 92% and 0% BO samples as shown in Table 2.1. As discussed in Section 2.3.3, the internal surfaces of all accessible micropores have graphitic-like surface structures. Thus the specific surface area of AC sample should be smaller than the theoretical specific surface area of graphene which is $2630\ m^2/g$. Therefore, the surface area of 92% BO sample calculated by the present method ($1912\ m^2/g$) is quite reasonable.

BO (%)	Measured (ppm)	Pore size d (nm)	Pore size d* (nm)	Micropore Volume (cm^3/g)	Micropore surface area (m^2/g)
0	-9.3	0.92	0.58	0.19	642
15	-8.3	1.02	0.68	0.25	747
29	-7.2	1.15	0.81	0.38	928
42	-6.5	1.25	0.91	0.51	1117
54	-5.8	1.38	1.04	0.67	1290
65	-5.3	1.47	1.13	0.88	1553
74	-4.8	1.59	1.25	1.00	1603
82	-4.4	1.71	1.37	1.18	1719
89	-4.3	1.74	1.40	1.39	1992
92	-3.9	1.89	1.55	1.48	1912

Table 2.1 AC samples with different BO values and the ^{1}H NMR derived δ_{avg}, pore size *d* and *d**, micropore volume, and micropore surface area.

2.3.5 PSD and Peak Broadening

Comparing with the static spectra, the full width at half maximum (FWHM) of ^{1}H spectra is significantly reduced under MAS from 4.6 ppm down to 1.3 ppm, as shown in Figure 2.10 Although the peaks of both the static and MAS spectra have the same average chemical shifts, the large anisotropic broadening of the static spectra obscures the contribution of intrinsic NICS distribution associated with PSD. In MAS spectra, the anisotropic broadening is removed [35], and the linewidth of peak B is dominated by micropore size distribution. The spin-lattice relaxation time T_1 under MAS is about 0.7 s, which contributes to an intrinsic line broadening of $\Delta\sigma(\text{ppm}) = \frac{1}{400}\frac{1}{\pi T_1} = 1.1\times10^{-3}$ at 400 MHz. This is negligible compared to the observed FWHM of 1.3 ppm, which is determined by NICS distribution. Therefore, it is possible to derive the PSD from the MAS spectrum.

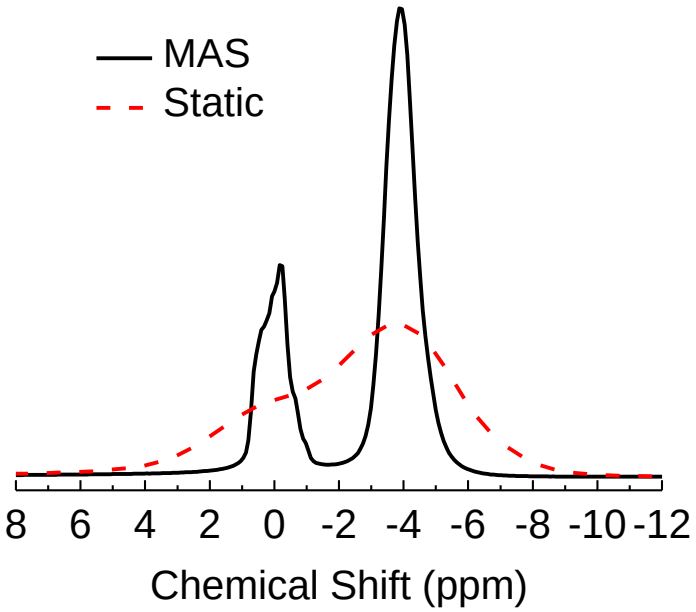

Figure 2.10 ^{1}H spectra of water in a P-92 AC sample. The static spectrum (dashed line, red) has a FWHM of 4.6 ppm, and the MAS spectrum (solid, black) has a FWHM of 1.3 ppm.

The function of pore volume versus pore size $V(d)$ is needed to calculate the PSD. The pore volume distribution function $V(d)$ can be calculated from the MAS NMR lineshape $I(\delta)$ by

$$V = \int V(\quad)\mathrm{d}\quad d \propto \int (\quad)\,\mathrm{d}\delta(\quad)\,d = \int (\quad)\quad \delta(\quad)\quad d \tag{2.6}$$

Therefore, $V(d) \propto I(\delta)\delta'(d)$. This relates the micropore size distribution $V(d)$ with the MAS NMR lineshape $I(\delta)$ and $\delta'(d)$, which can be obtained directly by taking the derivative of the function in Equation 2.2 to *d*. The NMR spectra in Figure 2.9 can then be translated into pore size distributions, and are shown in Figure 2.11. The distributions are scaled so that the areas are proportional to the total pore volumes listed in Table 2.1.

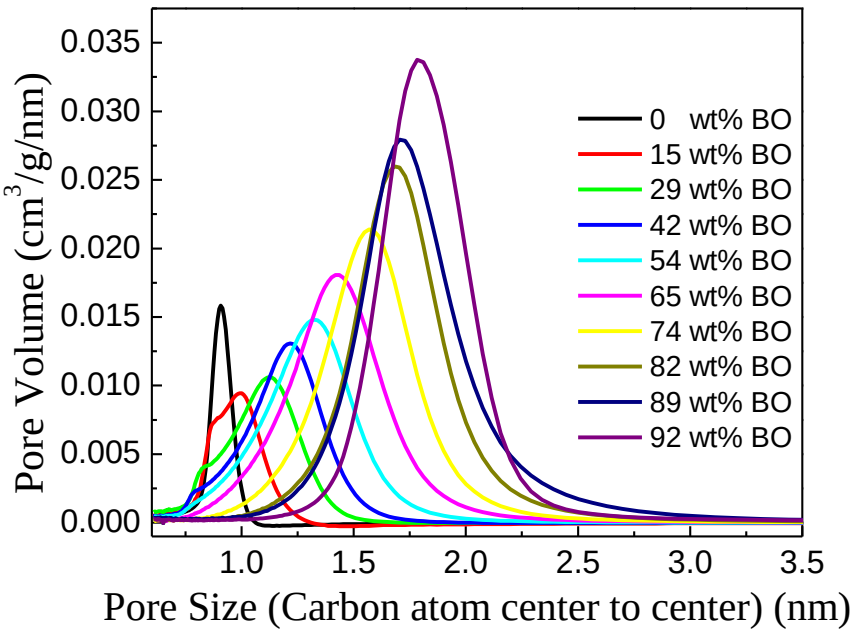

Figure 2.11 PSD obtained from ^{1}H MAS NMR spectra.

2.3.6 Effect of Carbonization Domain Size

Since the NICS effect is a local effect, it does not require the surface to be graphitic-like continuously on a large scale. It is important to realize that the NICS NMR porometry technique is not an atomic scale structural imaging technique. It probes local structures averaged over a certain length scale and measures the average pore size over such a length scale. Carbonization temperature is the crucial parameter in sample preparation for making the surface locally graphitic-like. All the AC samples discussed in this work were carbonized at 900 ℃. Graphitic crystalline domains can be clearly observed by transmission electron microscope in samples carbonized at temperatures above 1000 ℃ as shown in Figure 2.18 (Section 2.4.4).

High carbonization temperature makes atomic hybrid orbitals predominantly sp^2-like rather than sp^3-like and makes the graphitic-like domain larger; the degree of carbonization is also high (1 at% H in this work). The structural model employed in this work for NICS calculation is circumcoronene. Larger graphitic-like domain sizes than this could give rise to

slightly larger NICS effect on the order of 1 ppm [30]. Assuming an uncertainty of 1 ppm in the NICS effect due to local structure variations, this would give rise to an uncertainty in the determined pore size of approximately 0.08 nm (or 8%) for an average pore size of 1 nm (carbon atom center to center) and 0.36 nm (or 18%) for an average pore size of 2 nm (carbon atom center to center).

2.3.7 Diffusion Effect

As mentioned above, NICS NMR porometry measures the average pore size over a certain length scale. This length scale of averaging is determined by the diffusion length *l* of the probing molecule (H_2O in the current experiment) over the NMR time scale determined by the linewidth. From $T_2^* = 1/(1.3\ \text{ppm} \times 400\ \text{Hz} \times \pi)$, this time scale is about 600 μs. The water and BF_4^- diffusion coefficients inside ACs were reported to be on the order of $10^{-10}\ \text{m}^2/\text{s}$ [36] and $10^{-12}\ \text{m}^2/\text{s}$ [37], respectively. From $l = \sqrt{6Dt}$, *l* is estimated to be 600 nm for water and 60 nm for BF_4^-. As shown inset of Figure 2.2, the lineshapes of ^1H and ^{19}F spectra are nearly identical. The only difference is the tiny bump at the far right of peak B, and this is not surprising since hydrated BF_4^- cannot enter very small pores while H_2O can. The similar lineshapes of ^1H and ^{19}F spectra indicate that the length scale of averaging in the NICS NMR porometry technique is around 60 nm or less. Diffusion of water molecules can be restricted within micropores by barriers such as at pore throat. As it was reported [2] when probe molecules enter the microporous space, they tend to stay in this space, and the diffusion coefficient of probe molecules confined inside micropores of ACs can be very small ($4 \times 10^{-13}\ \text{m}^2/\text{s}$ for ethanol), and the length scale of averaging can be even smaller than 60 nm. Nevertheless, the PSD measured by NICS NMR porometry is a coarse-grained one over the length scale of averaging. In AC samples where micropores and mesopores are mixed in close proximity over a very short length scale much smaller than *l*, the NICS NMR porometry would then provide a pore size averaged over micropores and mesopores. In this case, peak B

will merge with peak A, and this could occur in our samples activated at the very high degree of burn off [11]. Figure 2.12 compares the water ^{1}H spectra in P-89 and P-94 AC samples. There is clearly a qualitative change in the ^{1}H spectrum of P-94 AC. Here, peak B nearly collapsed and merged with peak A. The high degree of activation creates very open structures where water molecules can effectively go through micropores and mesopores over the time scale of T_2^* causing the merge of peaks A and B. This averaging effect gives rise to a seeming smaller micropore volume in P-94 even though the burn-off is higher. In this case, the present technique is no longer effective in quantitative pore structure characterization.

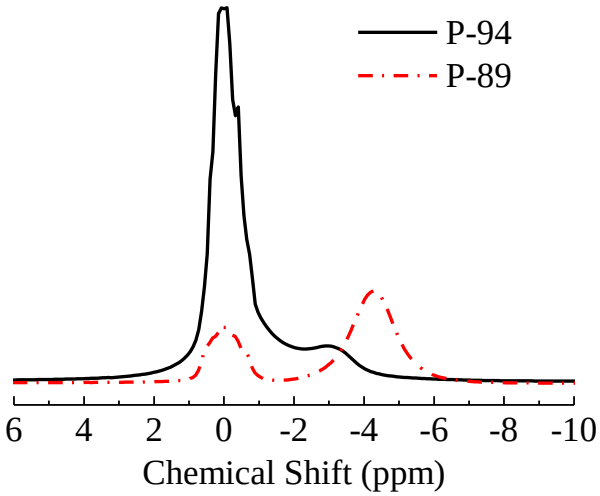

Figure 2.12 ^{1}H spectra of water in P-89 (dash-dotted line) and P-94 (solid line) AC samples. The intensity (spectral area) is scaled by water/AC weight ratio.

Other evidence also shows that water diffusion is extremely slow in our samples (except P-94). According to the SEM image of P-60 (Figure 2.17 in Section 2.4.4), the particle size is several hundred micrometers. It will take about 100 s for water molecules inside AC particles to diffuse to the surface assuming diffusion coefficient of 10^{-10} m^2/s. As a result, the sample should dry very quickly in a desiccator. In reality, it took at least two days to dry an AC sample loaded with water in a desiccator.

2.4 Experimental Details

2.4.1 High-Temperature Activation System

A high-temperature activation system is designed and constructed specifically for AC samples preparation, as shown in Figure 2.13. It consists of a *LINDBERG/NLUE Mini-Mite*^{TM} tube furnace, a 2.5cm diameter and 100cm length quartz tube, two argon gas flow meters with built-in valves, a sealed water chamber with two outlets, and a high-pressure argon gas cylinder with a regulator and a valve. Samples can be heated up to 1100°C by the tube furnace through programmed temperature steps and well controlled heating rate. The gas flow in the quartz tube can be switched between dry argon gas and wet argon gas (pass through the water chamber). The gas flow rate is monitored and well controlled.

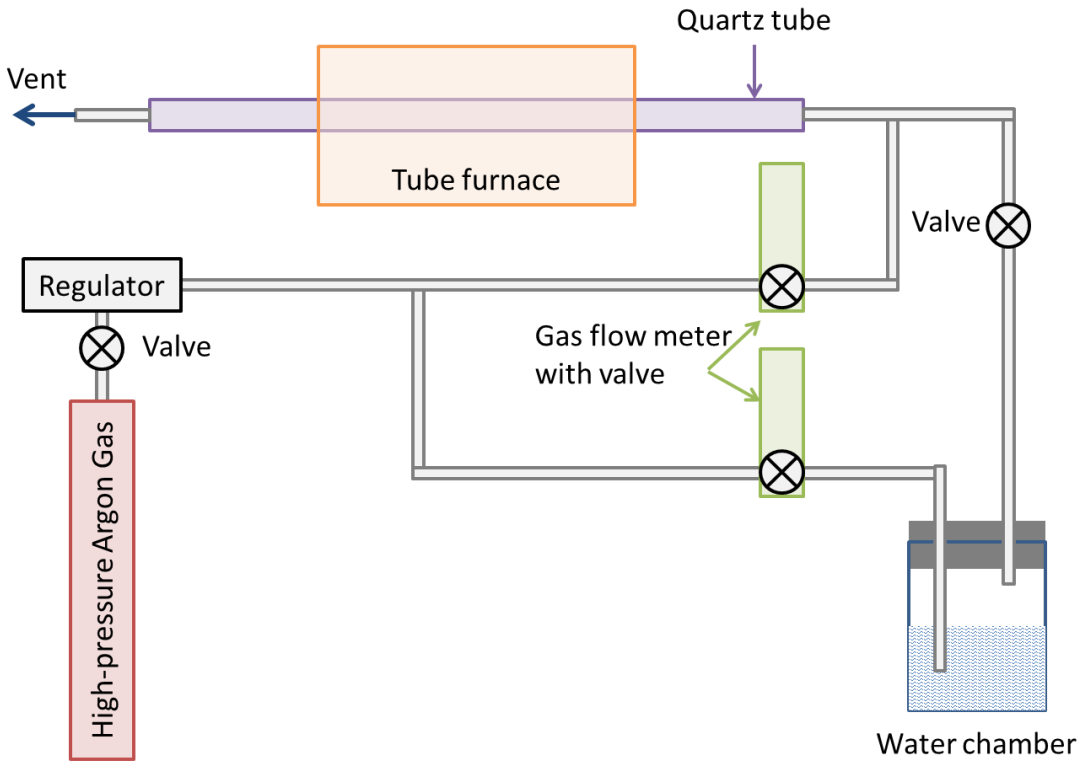

Figure 2.13 Schematic dagram of high-temperature activation system.

2.4.2 Sample Preparation and Nomination

Polyether ether ketone (PEEK) is used to prepare ACs by a method slightly modified from the procedure reported previously [38]. The process of sample preparation is divided

into two steps, carbonization and activation, where carbonization creates very small micropores and provides seeds for further micropore growth upon activation. Activation creates and enlarges micropores by reacting with weak bonds in the carbonized sample. During carbonization, pellets of PEEK were heated up under argon flow to 900 ℃ with a ramp rate of 45 ℃/min and carbonized at 900 ℃ for 30 min. The carbonized chunks were cooled down to room temperature under an argon flow and then ground into fine particles of approximately 0.5 mm in diameter. The ground material was heated up again to 900 ℃ and activated under water vapor carried by the Ar gas flow for a chosen period before cooling down to room temperature. An illustration and photos of sample preparation procedure are shown in Figure 2.14

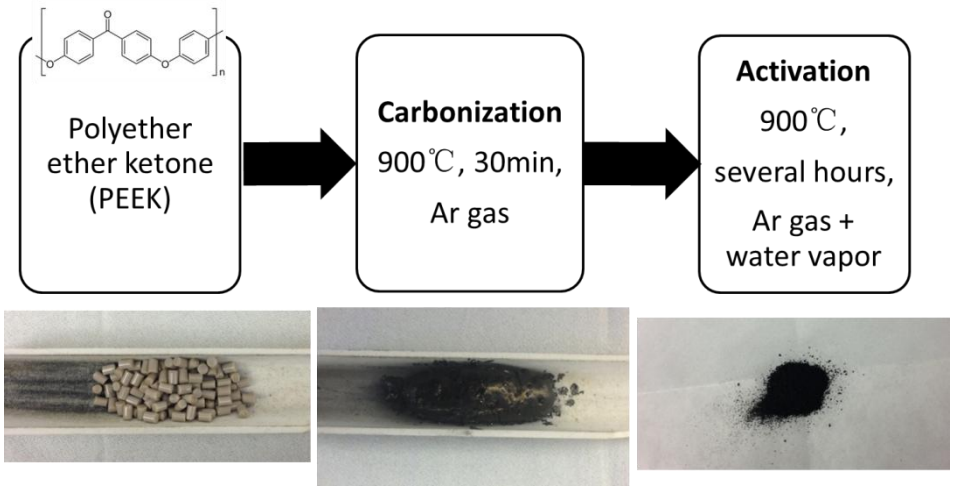

Figure 2.14 An illustration and photos of AC samples preparation procedure.

Activation for longer times leads to bigger micropores and larger burn off value (BO) which is defined as the ratio of mass reduction caused by the activation step with the mass of the sample before activation but after carbonization: $\mathrm{BO} = (m_c - m_a)/m_c$, where m_a is the mass after activation, and m_c is the mass before activation but after carbonization. Samples lose approximately 50% of the precursor mass in the carbonization step. The adopted sample label is based on its BO percentage such as sample P-92 represents an AC sample with BO of

92%.

2.4.3 NMR Experiment Details

The ^{1}H MAS NMR spectra were recorded at 400 MHz (9.4 T) on a TECMAG APOLLO spectrometer using a Chemagnetics MAS probe. About 10 mg AC powder was sealed in a 4 mm MAS rotor with an O-ring plug. The ^{1}H MAS NMR spectrum was acquired at a spinning speed of 8 kHz (all NMR spectra in this article were taken under 8 kHz MAS condition unless specified). A background ^{1}H MAS spectrum of the dry sample stored in a desiccator was first recorded. It is a weak featureless broad peak of 5 ppm, containing typically of 4×10^{20} protons/gram (1 at% H) and is subtracted in all spectra presented in this work as shown in Figure 2.15.

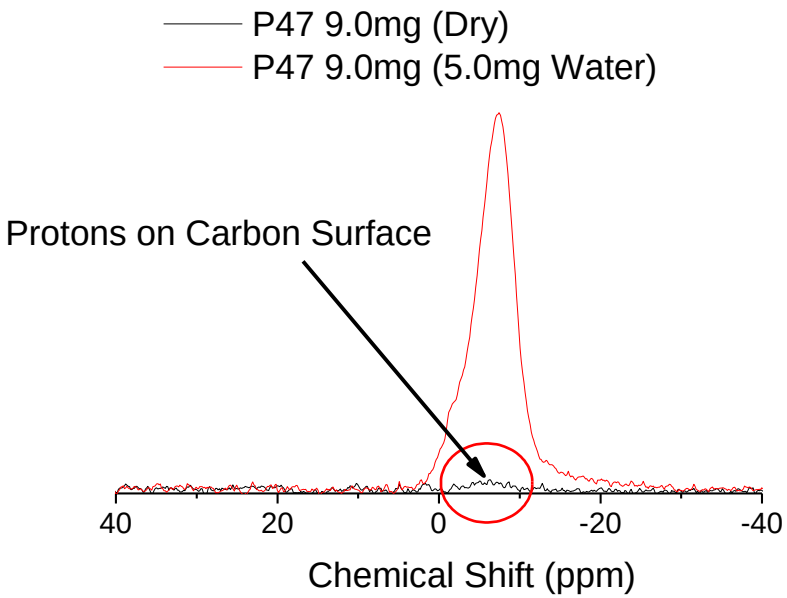

Figure 2.15 ^{1}H NMR background of AC samples carbonized at 900 ℃.

After that, a quantitative amount of distilled water was injected into the sample-containing MAS rotor using a syringe, sealed, and then waited till NMR spectra reaches equilibrium (typically less than 30 min). The amount of added water is determined both by the volume of injected water and by measuring the weight change of the MAS rotor.

All samples with adsorbed water were prepared by injection except some cases where vapor adsorption method is employed and will be mentioned specifically. An illustration of typical NMR measurements of AC samples loaded with water is shown in Figure 2.16.

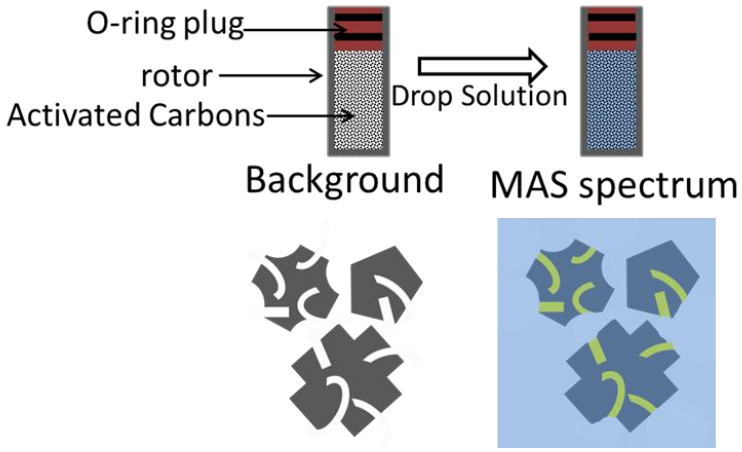

Figure 2.16 An illustration of typical NMR measurements of AC samples loaded with water

For verification, the sample was dried again in a desiccator for 48 hours, and the background spectrum was then taken again. The background spectra before and after adding water are identical for all samples, indicating that no permanent chemical bonds are formed in the process of the experiment. For further evaluation, water loading was also implemented by placing AC samples in saturated water vapor at room temperature for 20 hours. The ^{1}H MAS spectra of water adsorbed via saturated vapor and by syringe, injection were compared.

2.4.4 Other Characterization Results

Figure 2.17 is a scanning electron microscope (SEM) image of a P-60 AC sample. It shows the particle size of samples is several hundred micrometers.

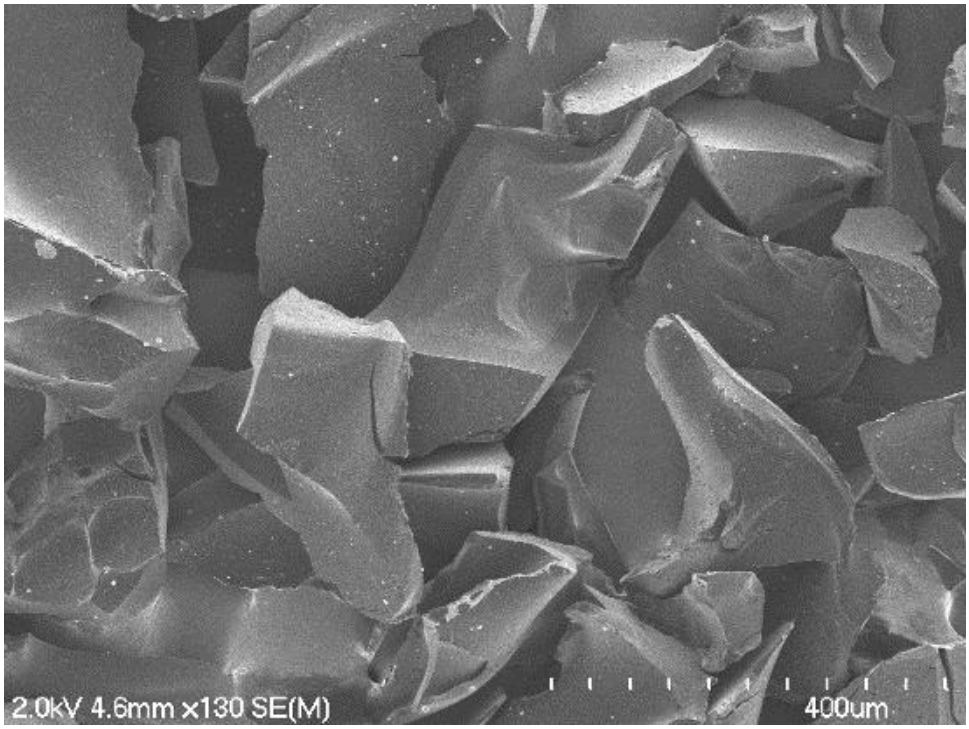

Figure 2.17 SEM image of an activated carbon sample of BO=60%. The scale bar is 400 μm, and each subdivision is 40 μm.

Figure 2.18a is the TEM result of the P-92 sample. It shows that after carbonization and activation at 900 ℃ AC, samples are amorphous carbon without significant crystallization. Figure 2.18b is the TEM result of AC sample after carbonization at 1000 ℃ for half an hour. Graphitic crystalline domains can be clearly observed.

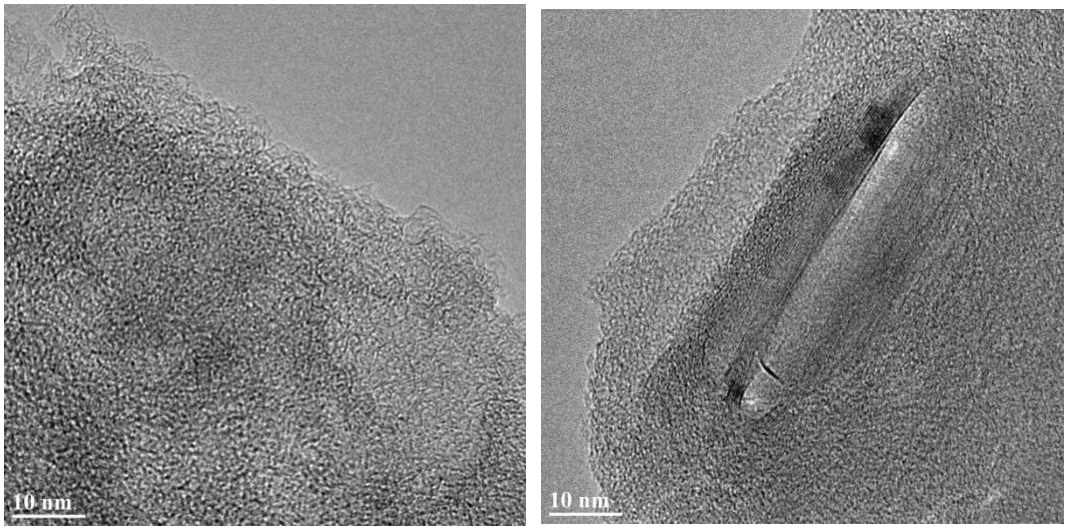

Figure 2.18 a (left) TEM result of the P-92 sample after carbonization and activation at 900 ℃; b (right) TEM result of AC sample after carbonization at 1000 ℃ for half hour.

The 92% and 0% BO AC samples are also characterized by nitrogen adsorption. The results are typical Type I adsorption isotherms, which indicate the dominant pore types are micropores in both samples, as shown in Figure 2.19.

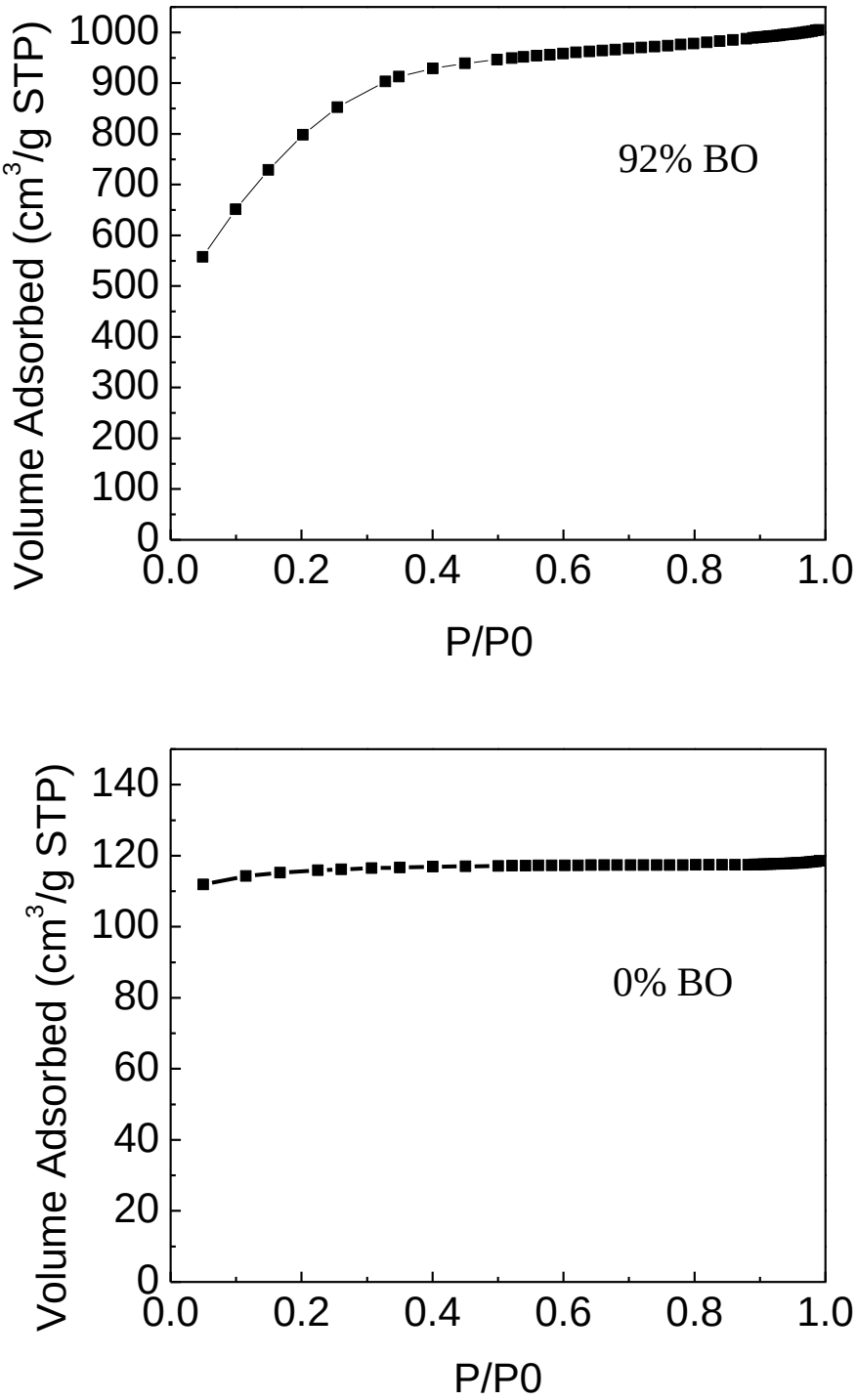

Figure 2.19 Nitrogen gas adsorption isotherms of 92% BO and 0% BO AC samples.

The BET area (5 points fitting at a relative pressure of range 0.05~0.3) and the total pore volume of 92% BO sample are $2888\ m^2/g$ and $1.55\ cm^3/g$ (at P/P_0=0.99), respectively. The 0% BO sample has $0.18\ cm^3/g$ total pore volume (at P/P_0=0.99).

2.5 Conclusion

NMR is a powerful tool for studying porous media. The NICS NMR porometry technique introduced here is suited for investigating pore structures of ACs smaller than 2 nm, which is traditionally the challenging pore size range for characterization. This technique is simple and offers information on pore size and PSD, pore volume, and surface area. It is based on room temperature ^1H MAS NMR spectrum of H_2O adsorbed in micropores. Because of the NICS effect, a distinct chemical shift is identified for H_2O molecules adsorbed inside micropores. The total micropore volume of ACs can be calculated from the intensity of the peak associated with micropores and the total amount of added water in the sample. A straightforward relationship between the PSD and the MAS NMR lineshape is established allowing the determination of the micropore size distribution from the lineshape of the ^1H MAS NMR spectrum. All these are made possible by DFT calculations which established the function of NICS versus the distance between the probe atom and the graphitic surface. Assuming this function is widely applicable for materials with local surface structures similar to graphitic materials, the only remaining task in future usage of this method is to take a room temperature ^1H MAS spectrum with known quantity of water added to the sample. From this, the micropore size distribution can be derived in a straightforward way.

REFERENCES

[1] Gun'ko VM, Turov VV, Kozynchenko OP, Nikolaev VG, Tennison SR, Meikle ST, et al. Activation and structural and adsorption features of activated carbons with highly developed micro-, meso- and macroporosity. Adsorpt-J Int Adsorpt Soc. 2011;17(3):453-60.

[2] Krutyeva M, Grinberg F, Furtado F, Galvosas P, Karger J, Silvestre-Albero A, et al. Characterization of carbon materials with the help of NMR methods. Microporous Mesoporous Mat. 2009;120(1-2):91-7.

[3] Furtado F, Galvosas P, Goncalves M, Kopinke FD, Naumov S, Rodriguez-Reinoso F, et al. The evidence of NMR diffusometry on pore space heterogeneity in activated carbon. Microporous Mesoporous Mat. 2011;141(1-3):184-91.

[4] Jackson CL, McKenna GB. The melting behavior of organic materials confined in porous solids. J Chem Phys. 1990;93(12):9002-11.

[5] Brownstein KR, Tarr C. Importance of classical diffusion in NMR studies of water in biological cells. Physical Review A. 1979;19(6):2446.

[6] Karge HG, Weitkamp J. Adsorption and Diffusion: Springer; 2008.

[7] Schleyer PV, Maerker C, Dransfeld A, Jiao HJ, Hommes N. Nucleus-independent chemical shifts: A simple and efficient aromaticity probe. Journal of the American Chemical Society. 1996;118(26):6317-8.

[8] Jonathan N, Dailey BP, Gordon S. Chemical Shifts and Ring Currents in Condensed Ring Hydrocarbons. J Chem Phys. 1962;36(9):2443-8.

[9] Pople JA, Untch KG. Induced Paramagnetic Ring Currents. Journal of the American Chemical Society. 1966;88(21):4811-5.

[10] Pople JA. Proton Magnetic Resonance of Hydrocarbons. J Chem Phys. 1956;24(5):1111-.

[11] Anderson RJ, McNicholas TP, Kleinhammes A, Wang A, Liu J, Wu Y. NMR Methods for Characterizing the Pore Structures and Hydrogen Storage Properties of Microporous Carbons. Journal of the American Chemical Society. 2010;132(25):8618-26.

[12] Dickinson LM, Harris RK, Shaw JA, Chinn M, Norman PR. Oxygen-17 and deuterium NMR investigation into the adsorption of water on activated carbon. Magn Reson Chem. 2000;38(11):918-24.

[13] Tabony J. Nuclear magnetic resonance studies of molecules physisorbed on homogeneous surfaces. Prog Nucl Magn Reson Spectrosc. 1980;14:1-26.

[14] Lazzeretti P. Ring currents. Prog Nucl Magn Reson Spectrosc. 2000;36(1):1-88.

[15] Gomes J, Mallion RB. Aromaticity and ring currents. Chem Rev. 2001;101(5):1349-83.

[16] M. J. Frisch GWT, H. B. Schlegel, G. E. Scuseria, , M. A. Robb JRC, G.

Scalmani, V. Barone, B. Mennucci, , G. A. Petersson HN, M. Caricato, X. Li, H. P. Hratchian, , A. F. Izmaylov JB, G. Zheng, J. L. Sonnenberg, M. Hada, , M. Ehara KT, R. Fukuda, J. Hasegawa, M. Ishida, T. Nakajima, , Y. Honda OK, H. Nakai, T. Vreven, J. A. Montgomery, Jr., , et al. Gaussian 09. Revision B.01 ed. Wallingford CT: Gaussian, Inc. 2010.

[17] Pople J. Sir John A. Pople, 1925–2004. 2004.

[18] W. J. Hehre WAL, R. Ditchfield, M. D. Newton, and J. A. Pople. Gaussian 70. Quantum Chemistry Program Exchange. 1970;Program No. 237.

[19] Segall M, Lindan PJ, Probert Ma, Pickard C, Hasnip P, Clark S, et al. First-principles simulation: ideas, illustrations and the CASTEP code. Journal of Physics: Condensed Matter. 2002;14(11):2717.

[20] Burkert U, Allinger NL. Molecular mechanics: American Chemical Society Washington, DC; 1982.

[21] R. Krishnan JSB, R. Seeger, and J. A. Pople Self‐consistent molecular orbital methods. XX. A basis set for correlated wave functions J Chem Phys. 1980;72(1):5.

[22] Kim K, Jordan K. Comparison of density functional and MP2 calculations on the water monomer and dimer. The Journal of Physical Chemistry. 1994;98(40):10089-94.

[23] Stephens P, Devlin F, Chabalowski C, Frisch MJ. Ab initio calculation of vibrational absorption and circular dichroism spectra using density functional force fields. The Journal of Physical Chemistry. 1994;98(45):11623-7.

[24] London F. The quantic theory of inter-atomic currents in aromatic combinations. J Phys Radium. 1937;8:397-409.

[25] McWeeny R. Perturbation Theory for the Fock-Dirac Density Matrix. Physical Review. 1962;126(3):1028-34.

[26] Ditchfie.R. Self-consistent perturbation theory of diamagnetism. 1. Gauge-invariant LCAO method for N.M.R. chemical shifts. Mol Phys. 1974;27(4):789-807.

[27] Wolinski K, Hinton JF, Pulay P. Efficient Implementation of the Gauge-Independent Atomic Orbital Method for NMR Chemical Shift Calculations. Journal of the American Chemical Society. 1990;112(23):8251-60.

[28] Cheeseman JR, Trucks GW, Keith TA, Frisch MJ. A comparison of models for calculating nuclear magnetic resonance shielding tensors. J Chem Phys. 1996;104(14):5497-509.

[29] Stanger A. Nucleus-independent chemical shifts (NICS): distance dependence and revised criteria for aromaticity and antiaromaticity. The Journal of Organic Chemistry. 2006;71(3):883-93.

[30] Forse AC, Griffin JM, Presser V, Gogotsi Y, Grey CP. Ring Current Effects: Factors Affecting the NMR Chemical Shift of Molecules Adsorbed on Porous Carbons. J Phys Chem C. 2014;118(14):7508-14.

[31] Moran D, Stahl F, Bettinger HF, Schaefer HF, Schleyer PV. Towards graphite: Magnetic properties of large polybenzenoid hydrocarbons. Journal of the American Chemical Society. 2003;125(22):6746-52.

[32] Texier-Mandoki N, Dentzer J, Piquero T, Saadallah S, David P, Vix-Guterl C. Hydrogen storage in activated carbon materials: Role of the nanoporous texture. Carbon. 2004;42(12-13):2744-7.

[33] Jensen TR, Østergaard Jensen M, Reitzel N, Balashev K, Peters GH, Kjaer K, et al. Water in Contact with Extended Hydrophobic Surfaces: Direct Evidence of Weak Dewetting. Phys Rev Lett. 2003;90(8):086101.

[34] Steele WA. The Interaction of Gases with Solid Surfaces. Oxford, New York: Pergamon Press; 1974.

[35] Levitt MH. Spin dynamics: basics of nuclear magnetic resonance: John Wiley & Sons; 2008.

[36] Kärger J, D.M. Ruthven, and D. Theodorou. Diffusion in zeolites and other nanoporous materials. Weinheim: Wiley-VCH; 2012.

[37] Zuleta M, Bjornbom P, Lundblad A, Nurk G, Kasuk H, Lust E. Determination of diffusion coefficients of BF_4^- inside carbon nanopores using the single particle microelectrode technique. J Electroanal Chem. 2006;586(2):247-59.

[38] McNicholas TP, Wang AM, O'Neill K, Anderson RJ, Stadie NP, Kleinhammes A, et al. H(2) storage in microporous carbons from PEEK precursors. J Phys Chem C. 2010;114(32):13902-8.

CHAPTER 3. A NOVEL NMR-BASED METHOD TO EVALUATE HIGH-PRESSURE METHANE STORAGE CAPABILITY IN GAS SHALE

3.1 Introduction

In this chapter, a novel method to evaluate the methane gas storage capability of shale samples based on NMR T_2 contrast and the Hahn Echo pulse sequence is introduced. Because the method utilizes the Hahn Echo pulse sequence, for the first time in a gas shale study, the Fourier-transform spectra signature of gas stored inside the shale rock is observed experimentally. Combining information from both the Fourier-transform spectra and the transverse relaxation mechanism allows the quantity of gas stored in shale to be estimated directly, without introducing uncertainty from other measurements. This method requires much shorter equilibrium time since it can be applied to gas shale particles instead of core plugs. Moreover, combining spectral, longitudinal relaxation, and transverse relaxation information not only offers more direct evidence for the stored gas, it also provides valuable information related to the storage mechanism and is a foundation for further research.

3.1.1 Unconventional Petroleum Systems

Petroleum systems are usually categorized as conventional resources or unconventional resources. In the early stages of the petroleum industry in United States, the distinctions between these two types were mainly based on economic considerations. Petroleum systems which had commercial value were called conventional resources, and those with no commercial value were called unconventional. With the increase of oil price and improvement in technology, however, some resources previously designated as unconventional were seen as conventional by certain exploration companies.

Although there are different perceptions of what is conventional or not for the economic

purposes, there is a fundamentally important distinction under geological view: conventional gas resources occur as discrete accumulations in structural and/or stratigraphic traps which are driven by buoyancy, but unconventional gas resources, which are generally not accumulated because of buoyancy, are regionally pervasive accumulations and commonly independent from structural and stratigraphic traps [1].

Unconventional petroleum resources generally consist of tight oil/gas, shale oil/gas, and sand oil. They are becoming more important to the annual oil/gas production in the United States. For example, the production of shale gas has grown from only 1% to over 20% of U.S. natural gas production and been predicted to reach 46% by 2035 [2].

3.1.2 Gas Shale

One of the important unconventional petroleum resources is gas shale, which is both the source of and the reservoir for natural gasses. Nature gas stored in gas shale systems is derived from the organic matter within the shale through biogenic and/or thermogenic processes. It is suggested that organic-rich shale, which is defined as fine-textured sedimentary rock containing $5 \sim 56$ percent combustible organic matter [3], could contain sufficient natural gas for commercial production according to the annual production distribution of shale gas in the United States [4].

Natural gas in organic-rich shale may be stored in three different locations in the material: matrix pores, organic matter (OM)-hosted pores, and fractures, as shown in Figure 3.1. OM-hosted pores, which have nanometer-scale pore size, are generally the most important contributors of nature gas storage in organic-rich shale formations. An example is the *Marcellus Formation of Pennsylvania*, of which average OM-hosted pore sizes are about 10~40 nm [5]. Therefore it is crucial to develop a method to characterize and estimate the natural gas stored in those pores.

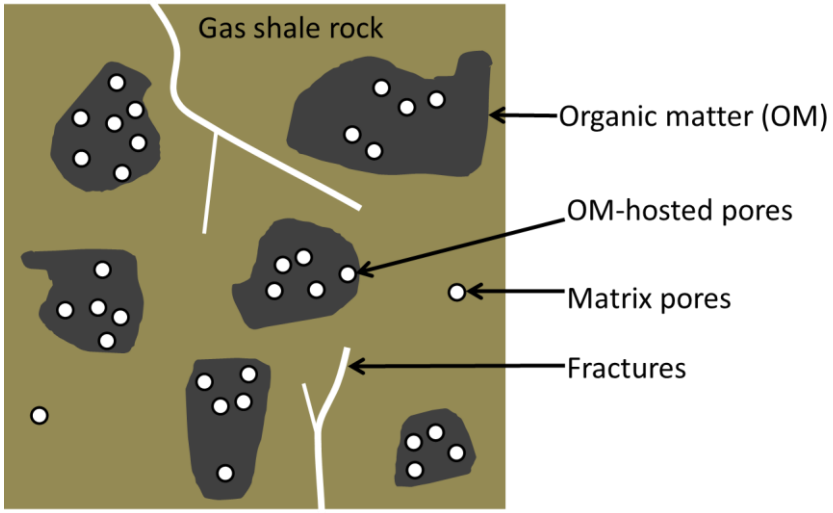

Figure 3.1 An illustration of gas shale porous system.

3.1.3 Application of NMR in Oil Industry

Nuclear Magnetic Resonance (NMR) is a versatile and noninvasive analytical technique which is suitable for characterizing fluid adsorbed inside porous materials. It has been widely adopted for well-logging in oil industry [6, 7]. Because of the complexity of the real well environment underground and the low signal-noise ratio of the downhole probes used onsite, the NMR well-logging analysis method commonly uses T_1/T_2 contrast and/or 2D mapping with the help of *Carr–Purcell–Meiboom–Gill* (CPMG) pulse sequence [8, 9] and Inverse-Laplace transforms techniques [10, 11].

Recently NMR has been employed to studies of shale gas systems using both well-logging tools and high field magnets [12-14]. Both artificial porous materials [15] and shale core plugs [16-18] have been used to study the storage mechanism and to determine the amount of methane stored inside the pores. The conventional NMR well-logging analysis methods based on T_2 contrast and Inverse-Laplace transformation have been introduced to shale gas systems too [13, 14, 19]. However, the extremely low permeability of methane inside shale rock dramatically slows down the measurement on shale core plug experiments [20, 21]. Generally, it may take up to several days for the system to reach equilibrium at each pressure for a core plug sample, but much less time is required when using small particles

(hundreds of micrometer of diameter). The conventional CPMG combined with Inverse-Laplace transformation methods, however, can fail to obtain the methane storage information in some gas shale samples due to an intrinsic property which reduces the molecular diffusion effect through field gradient space. More details will be introduced in Section 3.5.6.

3.1.4 Diffusion of Methane

The self-diffusion behavior of methane gas is introduced briefly in this section for a better understanding of the NMR methods and data analysis in the following sections which rely on the self-diffusion coefficient of methane under experimental conditions and environments.

The diffusion coefficient of gas at a certain temperature depends on the density. For a rough estimation of the density and pressure dependence of the diffusion coefficient of gas, the following empirical equation has been suggested [22]:

$$\frac{D_{P1}}{D_{P2}} = \frac{\rho_{P2}}{\rho_{P1}} \tag{3.1}$$

where D is diffusion coefficient, ρ is the gas mass density, and P_1 and P_2 are the corresponding pressures. Equation 3.1 shows that at high pressure/density the molecular diffusion of gas will slow down due to the smaller self-diffusion coefficient.

The classic Chapman-Enskog theory for a dense gas sphere [23] describes the diffusion behavior of high-density gas. It gives a reasonable prediction of viscosity but fails to predict the diffusion coefficient [24]. *K.R.Harris* reported an empirical polynomial fitting of the real experimental data of self-coefficient of methane gas based on an NMR spin-echo technique [25]. It is expressed:

$$\rho D = b_1 + b_2\rho + b_3\rho^2 + b_4\rho^2 \ln \rho \tag{3.2}$$

where D is diffusion coefficient, ρ is the gas mass density, and b_1 : b_4 are fitting

parameters. At 25°C , the fitting parameters are $b_1 = 0.6800$, $10^2 b_2 = -0.57770$, $10^2 b_3 = 0.09324$, and $10^3 b_4 = -0.42106$. The experimental value of the self-diffusion coefficient of methane at 4500PSI and 25°C is about $5.9 \times 10^{-8} \mathrm{m^2 s^{-1}}$.

The *diffusion length* provides a measure of how far the gas molecules have propagated during a certain time duration t and it is useful for analyzing the relaxation mechanism of NMR results. It can be estimated by solving Fick's law in one dimension [26]:

$$L_{diff} = 2\sqrt{Dt} \tag{3.3}$$

where D is self-diffusion coefficient.

3.1.5 Surface Relaxation

Surface relaxation is one of the major mechanisms of T_1 and T_2 relaxations in the shale gas system mentioned in the following sections. A simplified illustration of surface relaxation inside planar geometry pores is shown in Figure 3.2. When the molecules (red circle) diffuse through the pore space and get close to the relaxation center (purple half disk), relaxation can occur. As K. R. Brownstein and C.E. Tarr discuss [27], the general relaxation problem can be described:

$$\vec{\nabla} \cdot \left(\vec{D} \cdot \vec{\nabla} \rho \right) - \gamma \rho = \frac{\partial \rho}{\partial t} \tag{3.4}$$

$$\left(\hat{n} \cdot \vec{D} \cdot \vec{\nabla} \rho + \mu \rho \right) \Big|_S = 0 \tag{3.5}$$

$$\rho(\vec{r}, 0) = m(0)/V \tag{3.6}$$

Equation (3.4) is the diffusion equation allowing for bulk relaxations due to volume-like sink. Equation (3.5) is a boundary condition on the bounding surface S taking into account surface relaxations due to surface-like sink. Equation (3.6) is the presumed initial condition corresponding to an initial uniform magnetization of the sample. $\rho(\vec{r}, 0)$ is the magnetic moment per unit volume ($\mathrm{cm^{-3}}$), V is the sample volume ($\mathrm{cm^3}$), S is the sample surface (

cm^2), $\gamma(\vec{r})$ is the volume sink strength density (s^{-1}), which is assume to be 0, since only the surface relaxation are considered, $\mu(\vec{r})$ is the surface sink strength density ($cm \cdot s^{-1}$), $m(0)$ is the total nuclear magnetization of sample at initial state, $\ddot{D}(\vec{r})$ is the diffusion coefficient tensor ($cm^2 s^{-1}$), and $\hat{n}$ is the unit outward normal at the bounding surface. The equations can be solved with a sum of "normal modes" which has eigenvalues that can be ordered:

$$T_0 > T_1 \geq T_2 \geq T_3 \geq \cdots > 0 \tag{3.7}$$

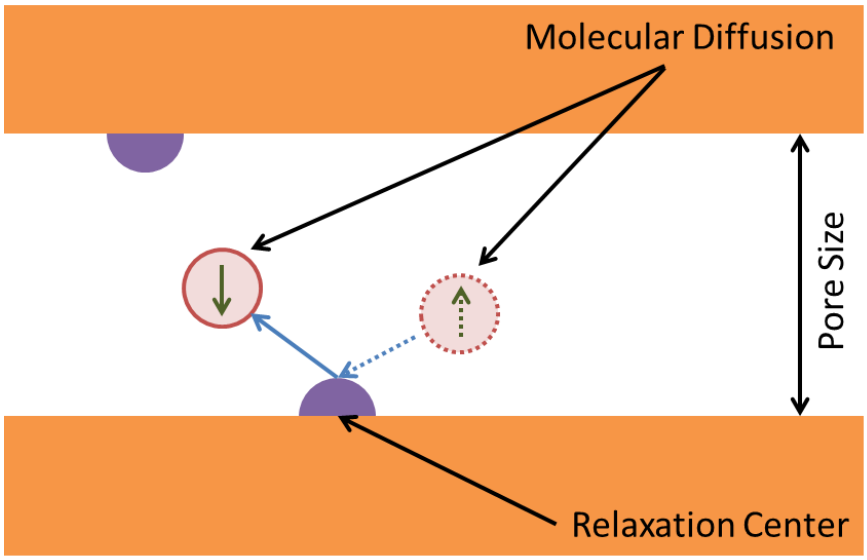

Figure 3.2 An illustration of surface relaxation procedure.

The details of solving these equations are presented in Brownstein and Tarr's paper [27], so it is omitted here. The solution is determined by the value of Ma/D, where M is the surface sink strength density, which depends on surface properties, a is the characteristic length, which is pore size in planar pore model, and D is diffusion coefficient of the probing molecules [27]. When $Ma/D \ll 1$ is satisfied, "fast-diffusion", the surface relaxation time is dominated by the zero-order solution, which in the planar pore model is

$$T_0 = \frac{a}{M} \tag{3.8}$$

In this case, the surface relaxation time is proportional to the pore size and is not correlated to diffusion coefficient. For "slow-diffusion" ($Ma/D \gg 10$), however, the solution of the planar pore model is:

$$T_0 = \frac{a^2}{D\left(0+\frac{1}{2}\right)^2 \pi^2} \tag{3.9}$$

$$T_n = \frac{a^2}{D\left(n+\frac{1}{2}\right)^2 \pi^2} \tag{3.10}$$

Both zero-order and higher order parts of solution need to be considered and the relaxation times depend on diffusion coefficient instead. The higher order terms will contribute about 19% of total intensity [27].

3.1.6 Magnetic Field in a Packed System

There is a lot of interest in understanding the effect of magnetic inhomogeneity on the NMR response and how this affects the magnetic resonance image, chemical shift, relaxation mechanism and so on [28-30]. A packed system of gas shale particles filled by methane gas, which is studied in this chapter, is a typical solid matrix system that can induce significant magnetic field inhomogeneity. A simplified model which consists a system of packed solid spheres with magnetic susceptibility χ_s and fluid media with magnetic susceptibility χ_m filling in the empty space is used for a basic study [31]. The magnetic moment $\mathbf{m}$ of a single sphere can be expressed as:

$$\mathbf{m} = \frac{\mu_s - \mu_m}{\mu_s + 2\mu_m} R^3 \mathbf{B_0} \tag{3.11}$$

where the μ_s and μ_m are the magnetic permeability for the sphere and fluid media respectively. Since only the isotropic susceptibilities are considered, $\mathbf{m} \approx 4\pi R^3 \cdot \delta\chi \cdot \mathbf{B_0}/3$

which is along the $\mathbf{B_0}$ direction. The origin of the non-uniform internal field is the contrast in susceptibilities, $\delta\chi \equiv \chi_s - \chi_m$.

The magnetic field generated by a magnetic dipolar moment $\mathbf{m}$ at position $\mathbf{r}$ can be expressed as

$$\mathbf{B^i} = \frac{\mathbf{3(m \cdot r)r - |r|^2 m}}{\mathbf{|r|^5}} \tag{3.12}$$

Then the total magnetic field contribution of the packed system of spheres can be calculated by a superposition of fields from each dipole:

$$B_z = \sum_k B_z^i \left(\mathbf{r - r_k}\right) \tag{3.13}$$

where $\mathbf{r_k}$ is the center of the dipole $\mathbf{k}$.

Though, in principle, the method described above can be used to calculate the magnetic field inhomogeneity in and field gradient in any system, the complexity of the shape and the susceptibility distribution of packed solids in the real sample will alter the result significantly [32], and is beyond the discussion scope here.

3.1.7 Magnetic Field inside Pores

Since the pore size (<100 nm) of gas shale samples is much smaller than the size (>100 μm) of sample particles used in the following experiments, only the contribution of the particle containing the pore is necessary to estimate the magnetic field response inside the pore. The classic model of magnetic shielding by a spherical shell of permeable material in a uniform field [33] can be used, as shown in Figure 3.3.

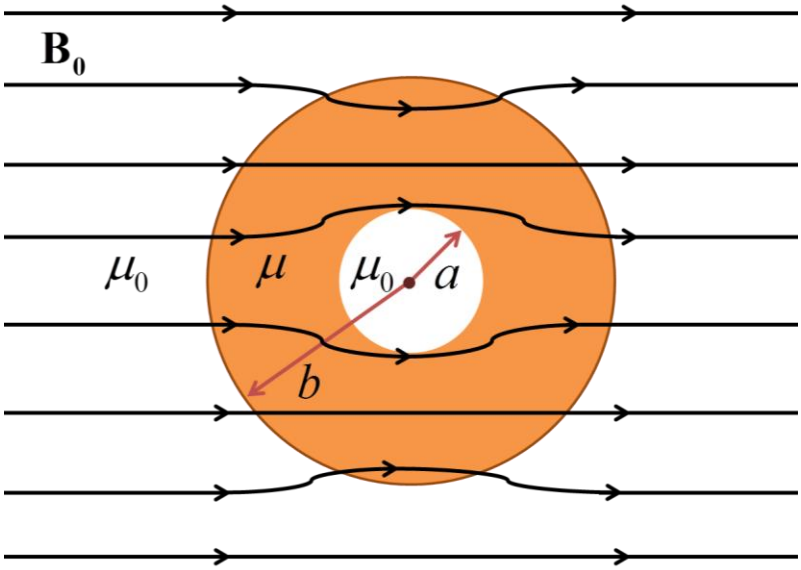

Figure 3.3 An illustration of magnetic shielding by a spherical shell of permeable material in a uniform field.

A hollow spherical shell with an inner radius a and an outer radius b is placed in a homogeneous external magnetic field $\mathbf{B_0} = \mu_0 \mathbf{H_0}$. μ_0 is the magnetic permeability of the outer and inner space, and μ is the magnetic permeability of the spherical shell. Since there are no currents present, a scalar potential Φ_M is used to derive the magnetic field $\mathbf{H} = -\nabla \Phi_M$. Since $\nabla \cdot \mathbf{B} = 0$ and $\mathbf{B} = \mu \mathbf{H}$, $\nabla \cdot \mathbf{H} = 0$ is satisfied in the various regions. Thus the potential Φ_M satisfies the Laplace equation everywhere and the problem reduces to finding the proper solutions in the different regions to satisfy the boundary conditions.

For $r > b$,

$$\Phi_M = -H_0 r \cos\theta + \sum_{l=0}^{\infty} \frac{\alpha_l}{r^{l+1}} P_l \quad (\cos\theta \quad (3.14)$$

For $a < r < b$,

$$\Phi_M = \sum_{l=0}^{\infty} \left(\beta_l r^l + \frac{\gamma_l}{r^{l+1}} \right) P_l(\cos\theta) \quad (3.15)$$

For $r < a$,

$$\Phi_M = \sum_{l=0}^{\infty} \delta_l r^l P_l(\cos\theta) \quad (3.16)$$

The boundary condition at $r = a$ and $r = b$ requires H_θ and B_r to be continuous, so it can be expressed by the potential Φ_M as,

$$\frac{\partial \Phi_M}{\partial \theta}(b_+) = \frac{\partial \Phi_M}{\partial \theta}(b_-) \tag{3.17}$$

$$\frac{\partial \Phi_M}{\partial \theta}(\mathrm{a}_+) = \frac{\partial \Phi_M}{\partial \theta}(\mathrm{a}_-) \tag{3.18}$$

$$\mu_0 \frac{\partial \Phi_M}{\partial r}(b_+) = \mu \frac{\partial \Phi_M}{\partial r}(b_-) \tag{3.19}$$

$$\mu \frac{\partial \Phi_M}{\partial r}(\mathrm{a}_+) = \mu_0 \frac{\partial \Phi_M}{\partial r}(\mathrm{a}_-) \tag{3.20}$$

The solution of the magnetic field inside the hollow space of the shell ($r < a$) is:

$$-\delta_1 = \left[\frac{9\mu'}{(2\mu'+1)(\mu'+2) - 2\frac{a^3}{b^3}(\mu'-1)^2} \right] H_0 \tag{3.21}$$

where $\mu' = \mu/\mu_0$.

Since $a \ll b$ and $B_1 = -\mu_0 \delta_1$, the solution can be simplified as,

$$\begin{aligned} B_1 &= \left[\frac{9\mu'}{(2\mu'+1)(\mu'+2)} \right] \cdot \mu_0 H_0 \\ &= \left[\frac{9\mu'}{(2\mu'+1)(\mu'+2)} \right] B_0 \end{aligned} \tag{3.22}$$

When $\mu' \approx 1$, the ratio of magnetic field shielding can be estimated as,

$$\begin{aligned} \sigma &= \frac{B_0 - B_1}{B_0} \\ &= \frac{2(\mu'-1)^2}{(2\mu'+1)(\mu'+2)} \\ &\approx \frac{1}{3}\chi^2 \end{aligned} \tag{3.23}$$

where $\chi \equiv \mu' - 1$ is the magnetic susceptibility of the spherical shell.

3.1.8 Relaxation Mechanisms of Free Methane Gas

Methane is complicated by the fact that it has four protons (spin $1/2$) in a molecule, therefore, there are three nuclear spin isomers $I = 0,1,2$. At relative low pressure, the *longitudinal relaxation* mechanism of methane is dominated by spin-rotational relaxation. It is given as [34]

$$T_1^{-1} \approx \gamma_n{}^2 \left\langle H'^2 \right\rangle \left\langle J\left(J+1\right)\right\rangle + \left\langle H''^2 \right\rangle \tau_c \tag{3.24}$$

where J is the rotational quantum number of molecular states, γ_n is the magnetic susceptibility of a proton nucleus, τ_c is the correlation time of molecular reorientation, H' is the field at a proton arising from rotation of the molecule, and H'' is the corresponding dipolar field at one proton arising from the others. In the equation there are two major interactions in the spin system of a methane molecule: spin-rotational interactions and direct dipolar interactions among proton spins. However, in methane molecules, the contribution of the latter part is much smaller than the former. Therefore, the spin-rotation interaction provides the dominant relaxation mechanism in methane. The probability per unit time of a transition between rotational states induced by molecular colliding can be described roughly as [34]

$$W \sim \left(t_0{}^2 \left| \left\langle m_J \left| V_1 \right| m_J{}' \right\rangle \right|^2 Z \right) \Big/ \hbar^2 \tag{3.25}$$

where Z is the number of collisions per second made by a molecule, d is the molecular diameter, v is the relative velocity, $t_0 \sim d/v$ is the duration of a collision, and V_1 is the anisotropic intermolecular potential leading to a transition. In a kinetic model of gasses, the pressure is equal to the force exerted by the atoms hitting and rebounding from a unit area of the container wall [35], therefore, the collision rate Z is proportional to the pressure of the gas. At room temperature, the correlation time of spin-rotational interaction of methane molecule is in the fast limit regime of protons T_1 relaxation [36], so a higher transition rate of

molecular rotational states will induce a longer T_1.

At sufficiently high pressure, intermolecular dipolar couplings during collisions should become important as the collision frequency increases. This induces a deviation from the linear increase of T_1 with pressure. However, the dipolar couplings are very weak and it is not clear that other transient relaxation mechanisms can be neglected [37]. The details will not be discussed here.

3.2 Relaxation Mechanisms of Methane Gas in a Packed Sample System

3.2.1 Model of a Packed Gas Shale System

A packed system with high-pressure methane gas is shown in Figure 3.4. The ^{1}H NMR signal from the system consists of three parts: protons of organic matters in gas shale sample, methane gas in the inter-particle space, and methane gas stored inside pores. The sample ^{1}H NMR signal has been measured under vacuum and then been subtracted from the signal after loading methane to eliminate the signal from organic matters. The empty space among sample particles is comparable to the particle size, which is $150 \sim 400\mu m$. The pore size of gas shale is generally less than $100nm$ [5], it is possible to distinguish the signal of methane gas stored in pores from the methane in the inter-particle space based on dynamic properties.

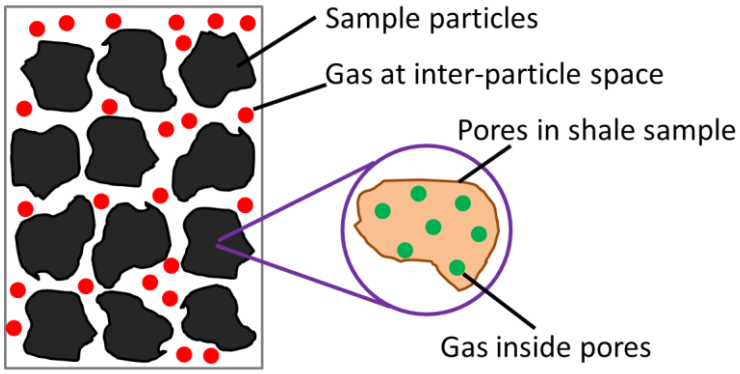

Figure 3.4 Schematic representation of gas shale sample particles packing system.

3.2.2 Longitudinal Relaxation (T_1)

As discussed in Section 3.1.8, the longitudinal relaxation mechanism of free gas in the empty sample tube is dominated by the spin-rotation mechanism at low-to-moderate pressures; at high pressures, intermolecular dipolar interactions play a role [15, 34]. The T_1 pressure dependences of both free methane gas in an empty sample tube and methane with gas shale samples have been measured (Figure 3.5). The free gas result is consistent with existing literature[38].

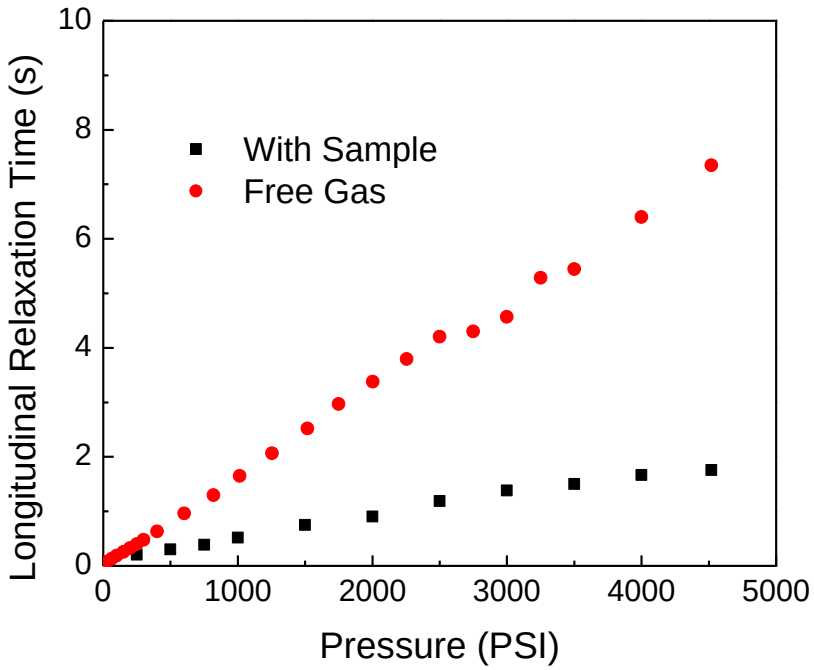

Figure 3.5 Pressure dependence of longitudinal relaxation time.

The difference in T_1 times between free gas in an empty sample tube and gas in the inter-particle space of gas shale sample is due to the surface relaxation (Section 3.1.5) induced by paramagnetic impurities in the mineral composition of gas shale samples [13, 27]. As discussed in Section 3.1.4, the *diffusion length* L can be calculated by Equation 3.3: $L_{diff} = 2\sqrt{Dt}$. The diffusion coefficient of methane gas at 4500 PSI is 5.9×10^{-8} m^2/s, and the measured T_1 time in Figure 3.5 is 1.3s. Plugging this into Equation 3.3, the estimated

diffusion displacement $L_{diff} = 0.55\ \text{mm}$, which is comparable to the space dimension among sample particles ($\sim 300\ \mu\text{m}$). From this we understand the molecular diffusion is fast enough for a significant increment of longitudinal relaxation rate by surface relaxation.

3.2.3 Transverse Relaxation (T_2)

In contrast to T_1, the transverse relaxation time (T_2) is sensitive to slow motions [36]. For the free gas in the empty sample tube, the collision between gas molecules and the sample tube walls dominates the T_2 relaxation mechanism [15]. For the packed gas shale system, the presence of paramagnetic impurity from gas shale sample induces field gradients under high static field, as shown in Figure 3.6.

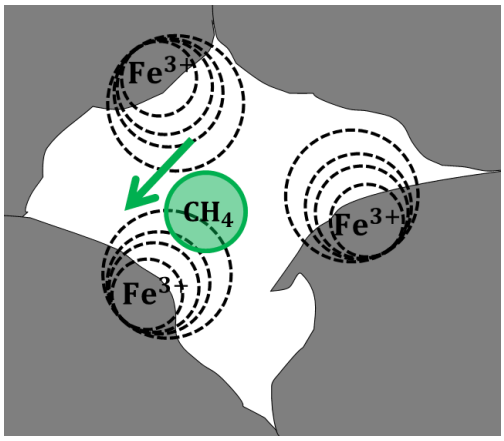

Figure 3.6 An illustration of methane diffusion under magnetic field gradient induced by paramagnetic impurities.

Molecular diffusion through field gradient dominates the transverse relaxation and it can be expressed as

$$M_{\text{int}}(t) = M_{\text{int}}^{0} \cdot \exp\left(-\left(\frac{1}{T_{\text{int}}^{B,S}} + a \cdot t^{2} \right) \cdot t \right) \tag{3.26}$$

where M_{int}^{0} is the NMR amplitude of methane molecules in the inter-particle space, $T_{\text{int}}^{B,S}$ is the relaxation time from bulk and surface relaxation, and $a = D \cdot (\gamma G)^2 / 12$ where D is the self-diffusion coefficient of gas molecules, γ is gyromagnetic ratio, and G is the magnetic field gradient [39].

Since the majority of the pores in gas shale are less than 100nm, the molecular diffusion of gas inside pores is negligible. The transverse relaxation mechanism of gas stored inside pores is dominated by surface relaxation [27] and can be expressed as

$$M_{\text{stor}}(t) = M_{\text{stor}}^{0} \cdot \exp\left(-\frac{t}{T_{\text{stor}}^{B,S}}\right) \tag{3.27}$$

where M_{stor}^{0} is the NMR amplitude from the gas stored inside pores, and $T_{\text{stor}}^{B,S}$ is the relaxation time from bulk and surface relaxation inside pores.

3.3 Estimation of High-Pressure Methane Gas Storage

3.3.1 Hahn Echo-Spectra Correlation

Use of the HahnEcho pulse sequence provides information regarding the evolution of NMR Fourier-transform spectra as a function of 2τ. The Fourier-transform spectra of methane gas at 4520PSI are presented as a function of 2τ in a 3-D figure as Figure 3.7.

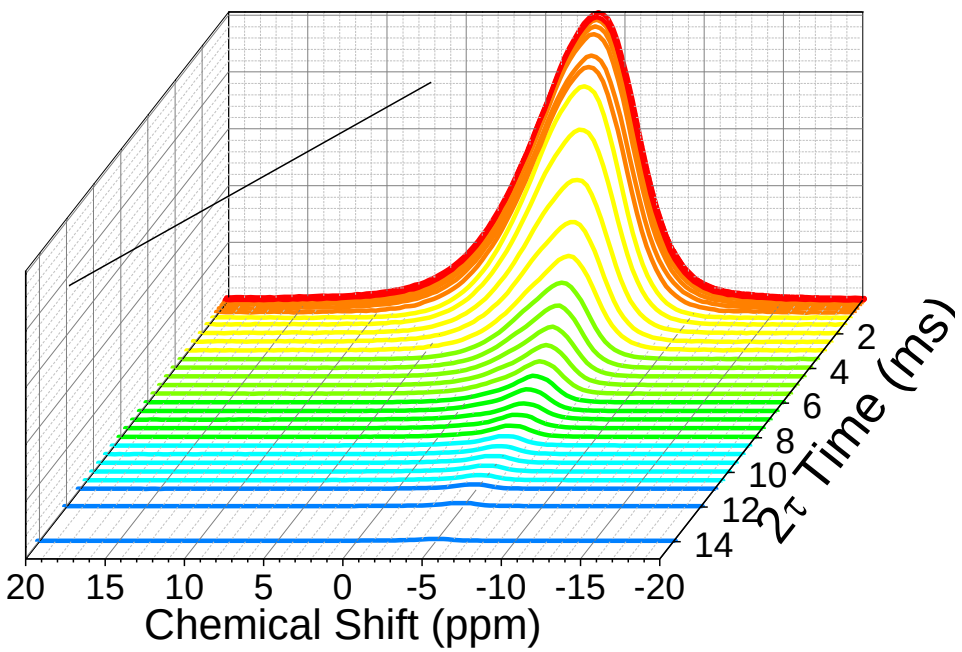

Figure 3.7 3-D plot of spectra evolution in 2τ space at 4520PSI. The x-axis is chemical shift in ppm (parts per million), the y-axis is 2τ in ms (microsecond) and the z-axis is the height of NMR spectra in arbitrary units.

The peak widths and centers of spectra change continuously with the 2τ value, which reflects the environmental difference of the inter-particle space and pore space. Meanwhile, the integration area of each spectrum is proportional to the amplitude of NMR signal at that 2τ position. The transeverse relaxation mechanism information can be acquired by the decay of NMR amplitude depending on 2τ, as shown in Figure 3.8.

3.3.2 NMR Amplitude vs. 2τ Space

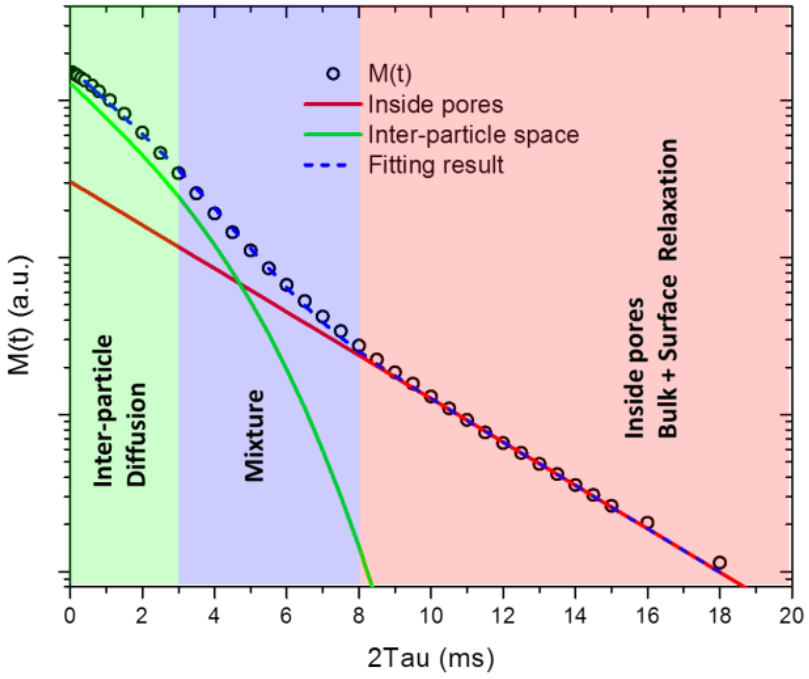

Figure 3.8 NMR amplitude vs. 2τ at 4520PSI. The y-axis is NMR amplitude with arbitrary units presented in a logarithm scale. The x-axis is 2τ in units of ms. Black hollow circles are experimental data points; blue dash line is the fit from Equation 3.28; the green line is the gas in the inter-particle space (Equation 3.26), which is dominated by diffusion; the red line indicates the gas stored inside the pores (Equation 3.27).

The data in Figure 3.8 can be separated into three regions based on relaxation mechanisms. From 0 to 3ms, the relaxation is dominated by diffusion of the gas in the inter-particle space. Then it follows an intermediate region from 3 to 8ms where the contributions of the gas in the inter-particle space and inside pores are comparable. For $2\tau \geq 8\text{ms}$, the diffusion part is negligible and only the gas stored inside pores is observable.

The data can be fitted by Equation 3.28, which is a combination of Equation 3.26 and Equation 3.27:

$$\begin{aligned} M(\mathrm{t}) &= M_{\mathrm{int}}(t) + M_{\mathrm{stor}}(t) \\ &= M_{\mathrm{int}}^{0} \cdot \exp\left(-\left(\frac{1}{T_{\mathrm{int}}^{B,S}} + a \cdot t^{2} \right) \cdot t \right) + M_{\mathrm{stor}}^{0} \cdot \exp\left(-\frac{t}{T_{\mathrm{stor}}^{B,S}} \right) \end{aligned} \tag{3.28}$$

where $M(t)$ is the sum of the magnetization from the gas in the inter-particle space and inside the pores. The fitting result is $M_{\mathrm{int}}^{0} = 1.24\times10^{5}$ a.u. ; $M_{\mathrm{stor}}^{0} = 0.30\times10^{5}$ a.u. ; $a = 5.4\times10^{-3}$ s^{-3}; $T_{\mathrm{int}}^{B,S} = 2.0$ ms and $T_{\mathrm{stor}}^{B,S} = 3.2$ ms. By plugging in the probe calibration result 3.51×10^{-6} mmol/(NMR a.u.) (Section 3.4.4), the absolute molar number of methane gas in the inter-particle space and inside the pores can be estimated as $n_{\mathrm{int}} = 0.434$ mmol and $n_{\mathrm{stor}} = 0.100$ mmol. The volume ratio of empty space among gas shale particles to the total volume of the sample tube can be estimated as:

$$\theta = \frac{n_{\mathrm{int}}}{n_{\mathrm{free}}} \tag{3.29}$$

where n_{free} is the molar number of free methane gas. According to the calibration results of free methane gas in an empty sample tube (Section 3.4.4), this is 0.934 mmol. Therefore the ratio of the volume occupied by shale sample is $\theta = 46.4\%$.

Since the packing ratio of the system is independent of pressure, the isotherm of gas stored inside pores can be obtained by Equation 3.30:

$$\begin{aligned} n_{\mathrm{stor}}(p) &= n_{\mathrm{total}}(p) - n_{\mathrm{int}}(p) \\ &= n_{\mathrm{total}}(p) - \theta \cdot n_{\mathrm{free}}(p) \end{aligned} \tag{3.30}$$

where $n_{\mathrm{total}}(p)$ is the total molar number of methane, which can be measured by FID at each pressure. The isotherm result is shown in Figure 3.9:

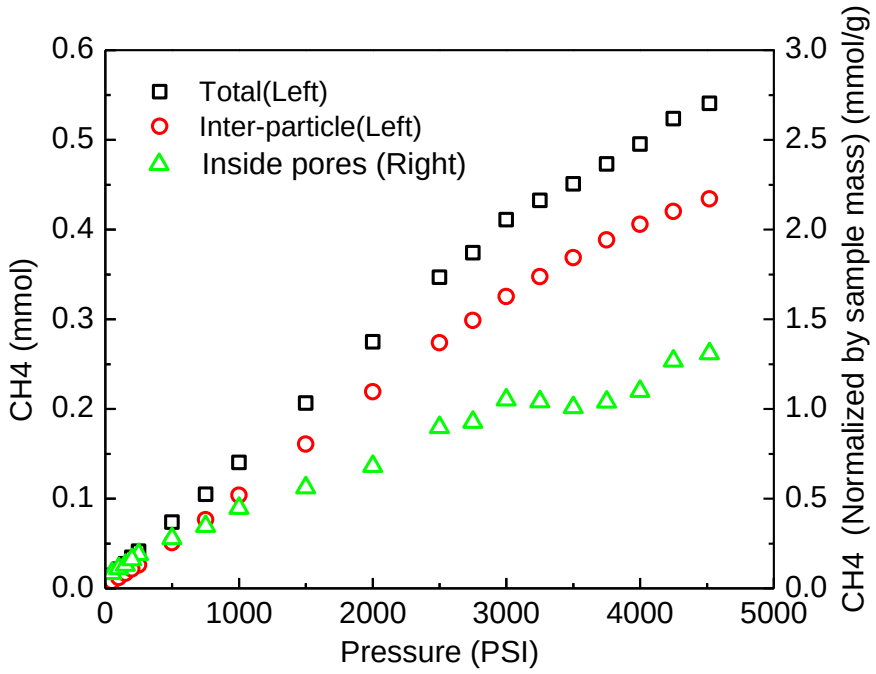

Figure 3.9 Pressure dependence of total methane (black square), inter-particle methane (red circle) and stored inside pores (green triangle). The amount of methane stored inside pores is normalized by gas shale sample mass.

A kink developed from pressure 3000 to 3500 PSI in the isotherm. One possible cause is the dissolution of methane molecules into the kerogen, which makes them undetectable due to strong dipolar interaction. The other possible cause is deformation of the OM-hosted pores at high pressure. There is a more detailed discussion in Section 4.3.4.

3.3.3 NMR Spectra vs. 2τ Space

As shown in Figure 3.10 (A), the NMR spectra at different 2τ show different features. The green spectrum ($2\tau = 10$ ms) is from the gas stored inside the pores, and the red spectrum ($2\tau = 50$ μs) is dominated by the gas in the inter-particle space. Comparing these two spectra, both the peak center and the peak width are different. That is due to the two different local environments. For a detailed analysis, both the peak center and the peak width, at different 2τ values, are presented in Figure 3.10 (B). Based on the curvature trends, both the peak width and peak center can be separated into two parts: the gas in the inter-particle space and the gas inside the pores.

The transverse relaxation mechanism of gas in the inter-particle space is dominated by the molecular diffusion through field gradients, so spins experiencing a stronger field gradient will relax faster and have a more positive chemical shift due to the higher environmental magnetic field. Consequently, both the chemical shift and the peak width of spectra will decrease dramatically when the NMR signal is dominated by inter-particle gas, as shown in Figure 3.10 (B). However, the spectra of gas stored inside pores are not sensitive to field gradient due to confinement, so only minor changes in peak center and width can be observed.

As discussed in Section 3.1.6, it is very difficult to precisely evaluate the magnetic field and field gradient in a packed shale sample due to the complexity of the real system. The NMR spectra, however, can provide valuable information about the magnetic field in the inter-particle space. Certain mineral components of the shale sample may produce paramagnetic centers, which can generate a strong magnetic field inhomogeneity in the high field of NMR system. The space closer to paramagnetic center has both a higher local magnetic field and a stronger field gradient. The spectrum for $2\tau = 0.05\text{ms}$ is dominated by the gas in the inter-particles space as has been discussed. The peak width is about 7.7 ppm, so the NMR detecting duration can be estimated by $T_2^* = 1/(\pi \cdot 7.7 \cdot 200) \approx 0.2$ ms for our 200MHz magnet system [36], as introduced in Section 1.4.4. During the T_2^* time, according to Section 3.1.4, the *diffusion length* of the gas molecules is only about $3.4\ \mu\text{m}$, which is much smaller than the inter-particle diameter. Therefore the peak width of the 0.05ms spectrum is dominated by the inhomogeneous broadening induced by gas shale particles, and the peak shape represents the distribution of magnetic field in the inter-particle space.

There is about a $2.5\ \text{ppm}$ chemical shift between the peak of inter-particle space and the peak of pores. This is due to shielding, as discussed in Section 3.1.7. The ratio of

magnetic field shielding is $\sigma \sim \chi^2/3$, where χ is the magnetic susceptibility of gas shale. Therefore the estimated magnetic susceptibility of the sample tested is $\chi = 2.7\times10^{-3}$, which is consistent with the literature vale $(0.01\sim15)\times10^{-3}$.

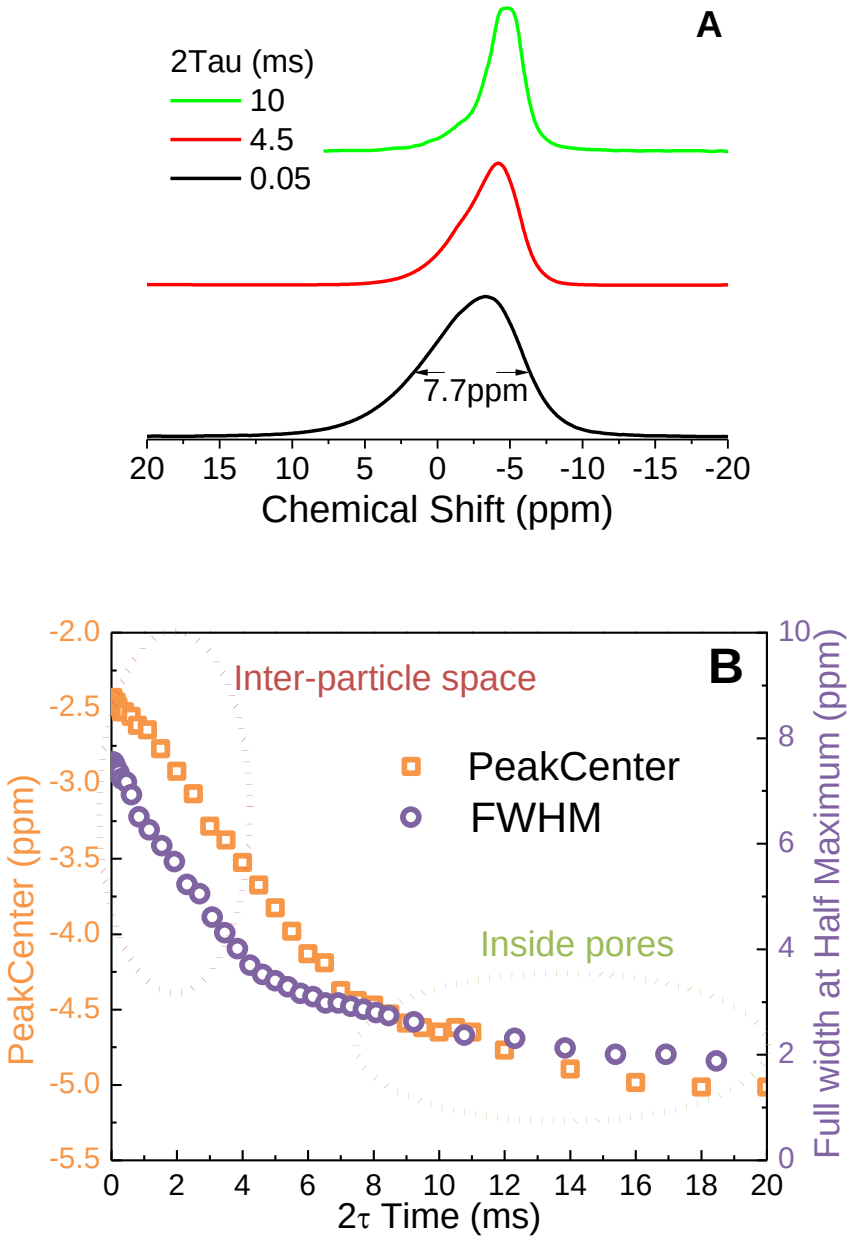

Figure 3.10 (A) is three selected spectra in 2τ space. (B) The evolution of spectra peak center and full width at half maximum (FWHM) in 2τ space.

3.3.4 In-Situ Pressure of Gas Shale

The HahnEcho measurement of the gas shale sample under vacuum (Figure 3.11) shows obvious long T_2 components. This is possible from the shale gas sealed in unopened pores [14].

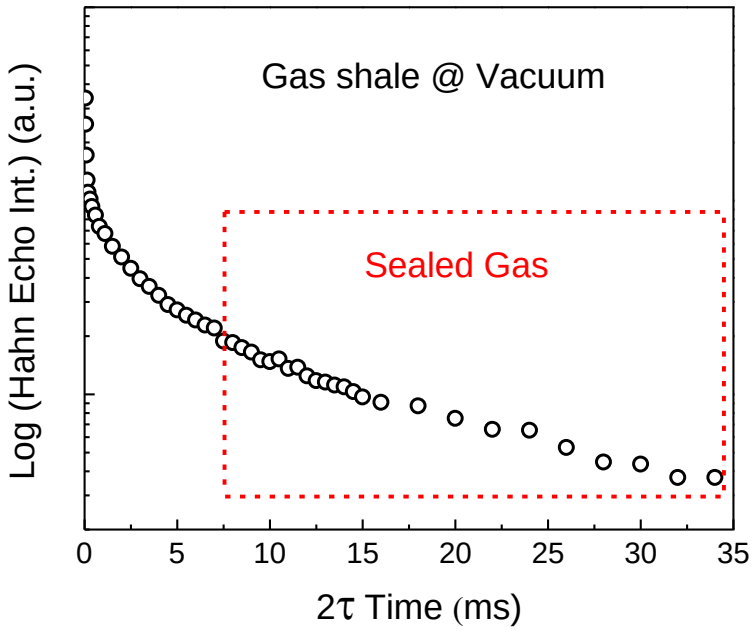

Figure 3.11 Hahn Echo Int. of gas shale sample under vacuum condition.

The longitudinal relaxation times for gas both sealed inside unopened pores and gas stored inside opened pores at different pressures are obtained by a T_1-T_2 correlation measurement (Section 3.4.3). The results are shown in Figure 3.12. A monotonous pressure dependence of T_1 is observed. With the assumption that the opened and unopened pores have similar environments, the pressure of sealed gas can be estimated to be below 1500PSI. More reliable results can be obtained by considering other components of shale gas in the real case, such as ethane, which may also effect on T_1 of methane. Since this part of the gas is sealed and well maintained inside pores, the pressure can provide valuable information related to gas generation and geologic evolution of the gas shale sample.

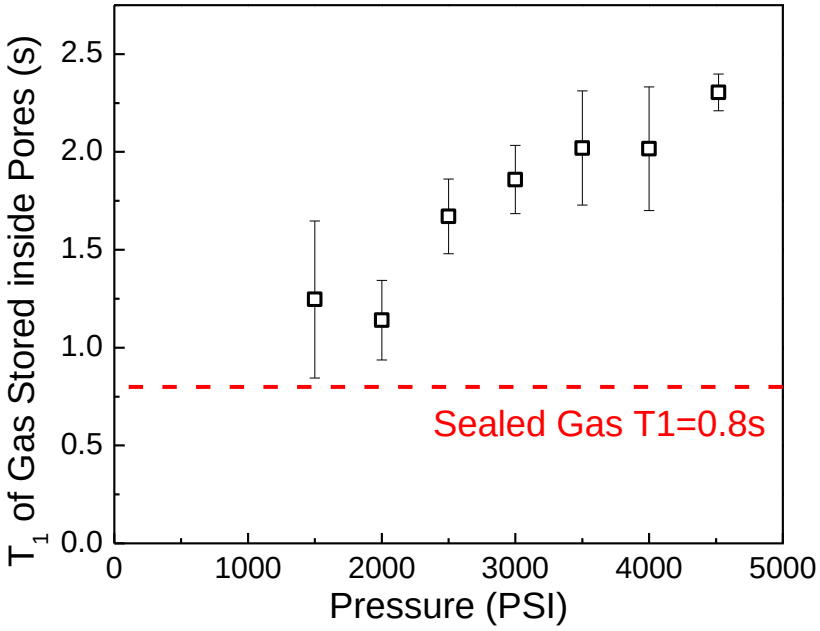

Figure 3.12 T_1 of gas stored inside pores (black square) and gas sealed inside gas shale sample (red dash line).

3.4 Experimental Details

3.4.1 High-Pressure NMR System

All NMR measurements are performed on a 200 MHz OXFORD magnet with a high-pressure system, as shown in Figure 3.13. The NMR spectrometer is from Tecmag and the amplifier is from AMT. The high-pressure system consists of a gas cylinder, a HiP high-pressure generator, an Edwards oil pump and a ceramic sample tube. The gas cylinder provides high purity methane gas (Air gas, 99.999%) whose pressure can be finely controlled by a regulator up to 1600 PSI. The system pressure can be further increased by the HiP high-pressure generator up to 5000PSI. The sample tube is made from zirconia with 2.96mm inner diameter, 5mm outer diameter, and 100mm length. It is well sealed within the high-pressure system by a rubber O-ring which is designed to hold pressure up to 10,000 PSI.

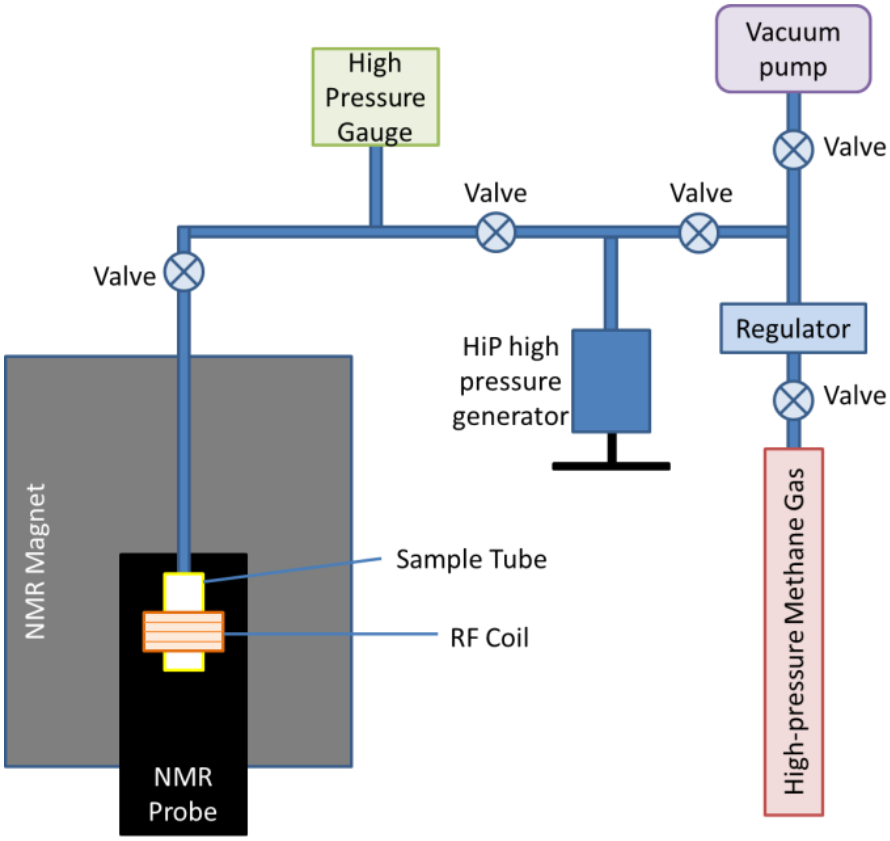

Figure 3.13 Schematic diagram of a high-pressure system used in this work. The up limit pressure of this system is 5000 PSI.

3.4.2 Sample Preparation

Gas shale samples are ground into particles and loaded into the ceramic sample tube. The loaded particle size is controlled around $150 \sim 400\mu m$ by sieves. After being connected and well-sealed into the high-pressure system, the sample tube is heated up to $85^{o}C$ under vacuum condition overnight to remove adsorbed air and water. Figure 3.14 shows the photos of gas shale samples before and after grinding.

Figure 3.14 Photos of the gas shale sample before and after grinding.

3.4.3 NMR Pulse Sequence

Besides the general pulse sequences introduced in Chapter 1, such as FID, CPMG and Hahn Echo pulse sequences, a T_1-T_2 correlation pulse sequence also has been applied. The pulse sequence is shown in Figure 3.15.

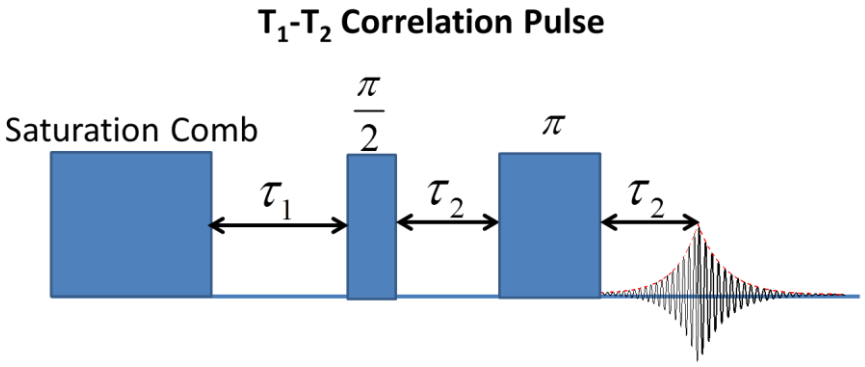

Figure 3.15 T_1-T_2 correlation pulse sequence.

The saturation comb pulse is composed of 16 $\pi/2$ pulses with certain phase cycling to eliminate both the longitudinal transverse components of magnetization [40]. After the T_1 spacing time τ_1, it follows a sequence which is similar to a Hahn Echo pulse.

3.4.4 NMR System Calibration

The sample tube volume and the inner diameter are calibrated by water loading measurements and the result is shown in Figure 3.16.

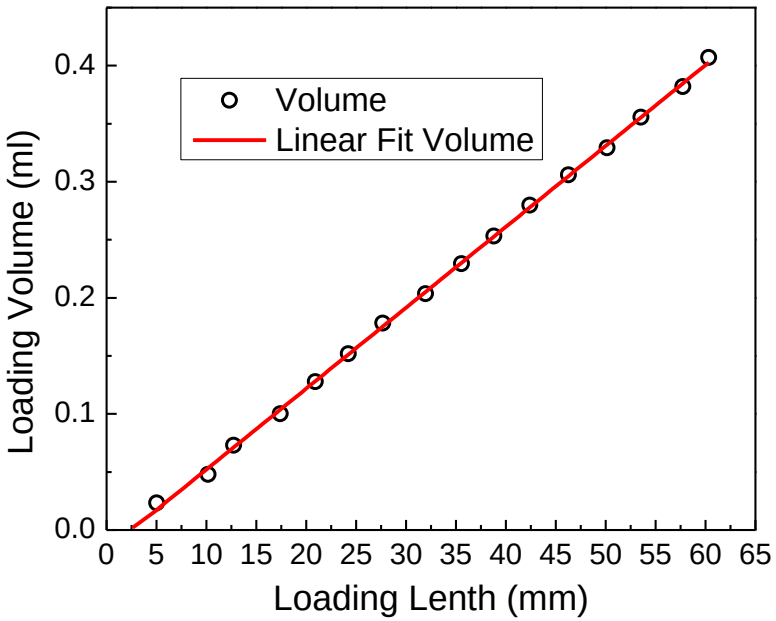

Figure 3.16 Calibration data of tube volume by water loading.

The data is fitted well by a line with a slope $k = 0.00697$ ml/mm = 6.97 mm^2. Since the loading length is measured from the outer bottom surface of the sample tube, the crossing point between the fitting line and the x-axis indicates the thickness of bottom wall which is 2.5 mm. The inner diameter of sample tube can be calculated according to slope by equation 3.31,

$$d = \sqrt{\frac{4k}{\pi}} = 2.98 \text{ mm} \tag{3.31}$$

Since the length of probe coil is $l = 10.1$ mm, the detection volume of the coil is $v = 70.7$ mm^3.

In order to acquire the absolute molar number of methane gas and protons in gas shale samples, the NMR system is calibrated by the measurement of free methane gas in the empty tube. The data is shown in Figure 3.17 (A)

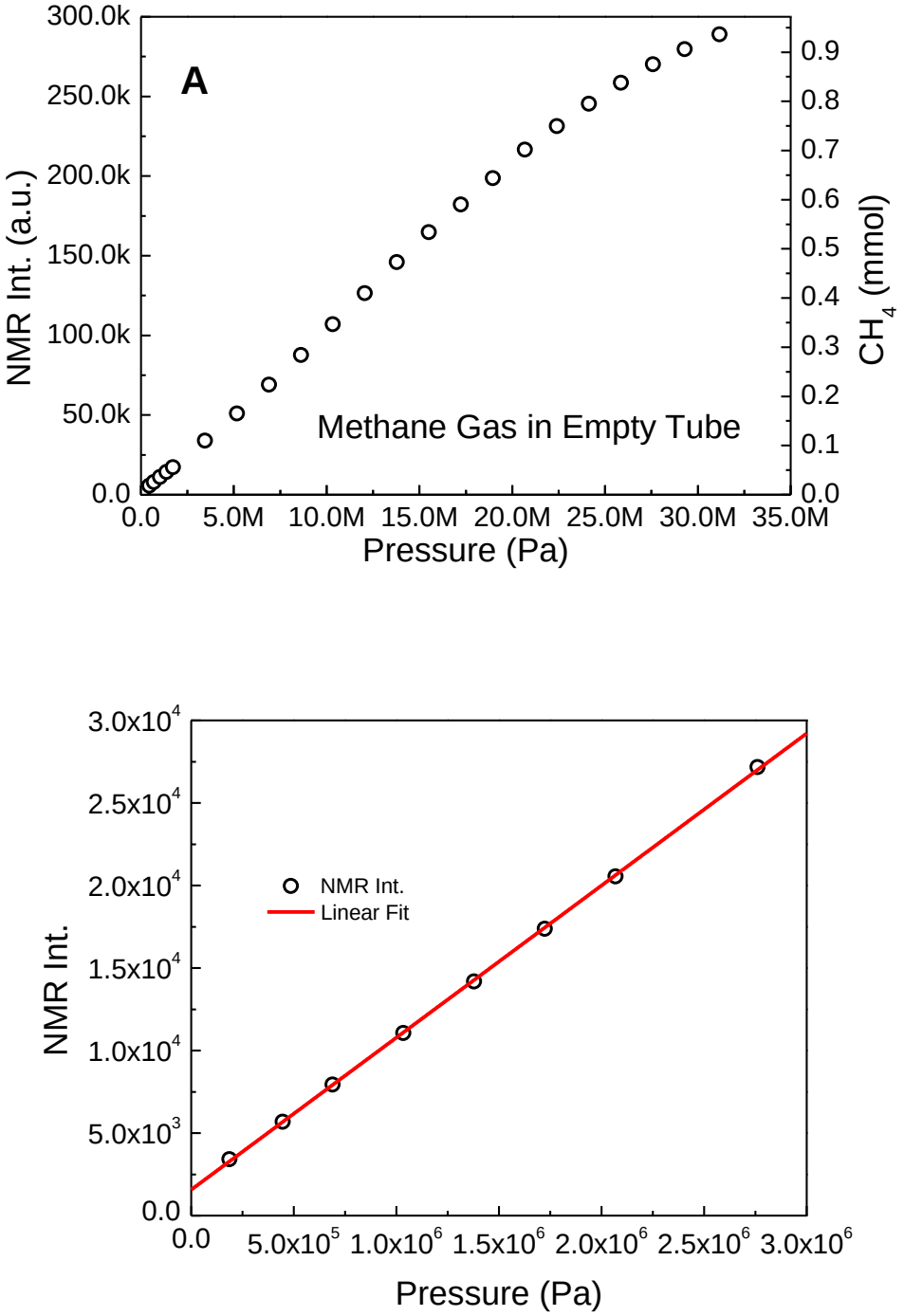

Figure 3.17 (A) NMR intensity of free methane gas in the empty sample tube. The label of Y-axis on the left is the NMR intensity and on the right is calculated based on the calibration data acquired in this section. (B) Zooming in on the data at low pressure for a linear fitting.

A linear fitting result is also shown in Figure 3.17(B). The slope is $k = 0.00922$ NMR Int./Pa . The intercept is from the probe background at 0 Pa. The

calibration ratio can be calculated by equation (3.32),

$$\alpha = \frac{v}{RTk} \tag{3.32}$$

where $v = 70.7\ \text{mm}^3$ is the coil detecting volume, R is ideal gas constant, $T = 285\text{K}$ is environmental temperature, and k is the fitting slope. The calculated ratio is $\alpha = 3.24\times10^{-6}$ mmol/NMR Int.

3.5 Uncertainty Analysis and Discussion

As introduced in Chapter 1, the intensity of the NMR signal is proportional to the total number of nuclei detected by the probe coil. The ratio of NMR signal intensity to nucleus number can be calibrated by the method mentioned in Section 3.4.4. However, the real experimental conditions generally are different from ideal assumptions, so several experimental and data processing issues, and also the uncertainty analysis, will be discussed in this chapter.

3.5.1 Solving the "Dead Time" Problem of FID Results

As introduced in Chapter 1, the NMR signals are generally acquired as the FID process. The single pulse is the most common pulse sequence to detect FID. It is composed by a 90° pulse immediately followed by an acquisition-time (AQ) during which the electronic receiver records the NMR signal. In the real case, however, a ring-down (RD) delay time between the pulse time and acquisition time is necessary to avoid receiver overloading [41] as shown in Figure 3.18.

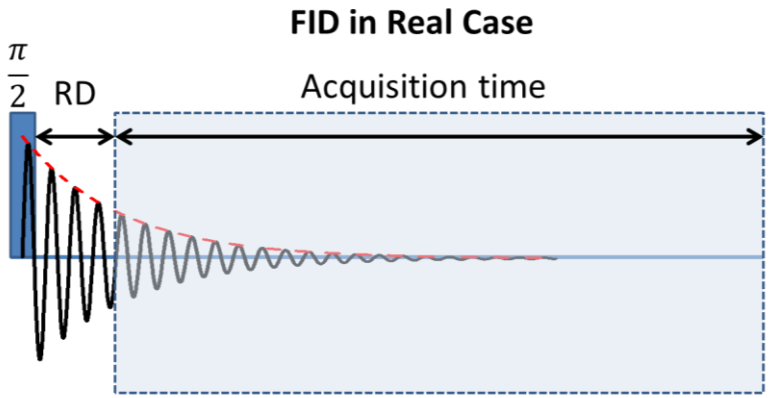

Figure 3.18 FID pulse sequence in a real case.

Therefore in order to retrieve the intensity of the NMR signal at the beginning of FID, it is important to extrapolate the FID data back to the zero point in the time domain. The extrapolation is shown in Figure 3.19. The y-axis is the NMR intensity, which is plotted as in a logarithm scale, and the x-axis is the FID time, which includes a 14.5 μs RD delay time at the beginning. A linear fit of the first 20 points is used to estimate the NMR intensity at the beginning of time domain. The log(*NMR Int.*) vs. *t* plot is based on the assumption that the decay rate of FID at the start is a single component exponential decay and it will induce a *Lorentz*-shaped spectrum in the frequency domain, which is usually seen in a gas or liquid system [42].

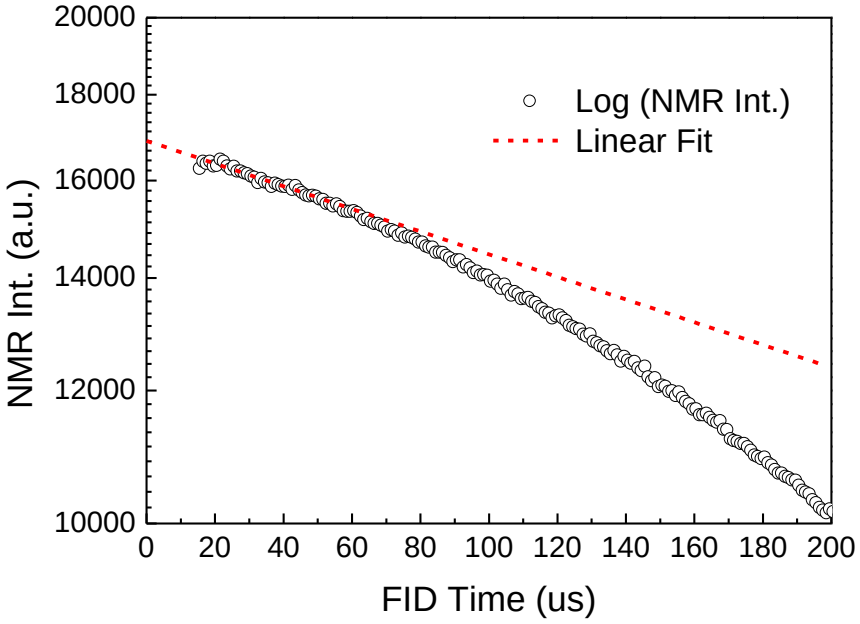

Figure 3.19 Extrapolation of FID data by linear fitting on log(*NMR Int.*) vs. t.

When the proton signal from the background of the gas shale sample dominates the start of FID, it will show a *Gaussian*-shaped spectrum. A plot of log(*NMR Int.*) vs. t^2 is required for a precise extrapolation, as shown in Figure 3.20.

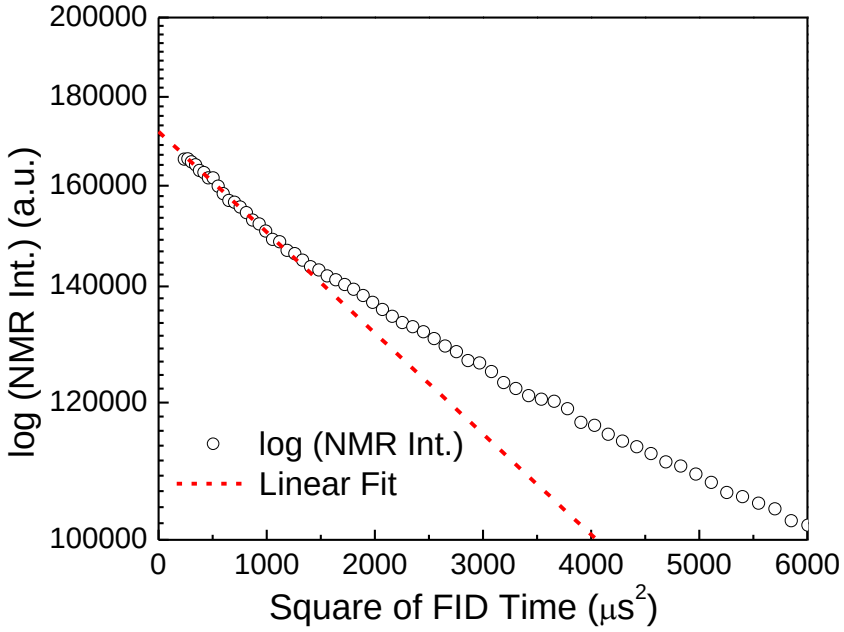

Figure 3.20 Extrapolation of FID data by linear fitting on log(*NMR Int.*) vs. t^2.

3.5.2 Solving the Fitting Issues of HahnEcho Results

As mentioned in Section 3.3.2, the NMR intensity of the HahnEcho data vs. 2τ can be fit with by Equation 3.28, which is the sum of a diffusion term (Equation 3.26) and a pore storage term (Equation 3.27). Because the y-axis is plotted on a logarithm scale, it is difficult to fit both parts precisely over the whole 2τ region. The diffusion part will dominate the overall fitting result since it is almost one order of magnitude larger than the pore storage part. Therefore a linear fit is applied to the long decay time region (red color area in Figure 3.8) and extrapolated back to estimate the storage part at short times. After this part has been subtracted from the original data, what remains is fitted with Equation 3.26 as shown in Figure 3.21.

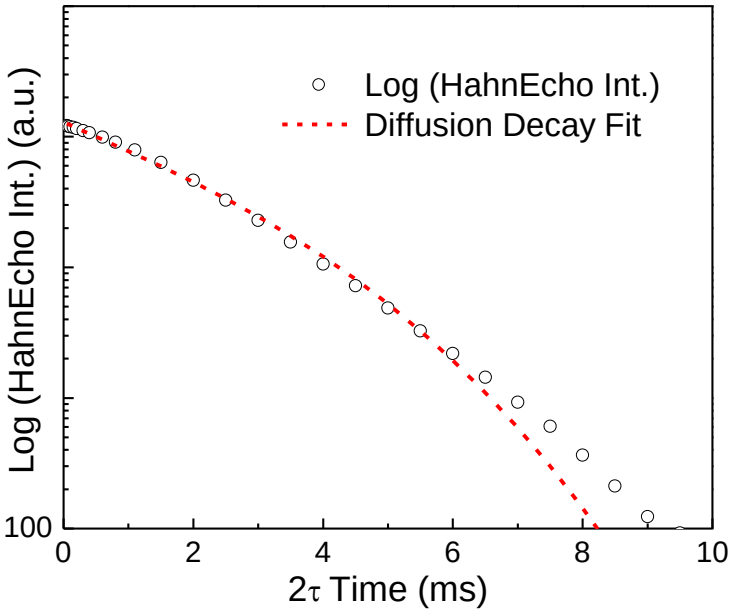

Figure 3.21 Fitting the Hahn Echo result of diffusion part.

There is a divergence of the fitting curve at the decay time longer than 6ms. One possible reason for this is the exchange of methane gas between the inter-particle space and the pore space. Since it is two orders of magnitude less than the value at short decay times, the divergence is negligible.

3.5.3 Calibration between FID and HahnEcho Results

As introduced in Chapter 1, the intensity of the NMR signal is proportional to the total number of probing nucleus spins. This means the intensity of the NMR signal should be independent of specific pulse sequence, as long as the system is fully excited. However, in the real experimental case, the number of spins detected may depend on specific pulse sequence for several reasons including molecular diffusion and imperfect coil.

Both the FID and the HahnEcho pulse sequences have been applied to the gas shale system as a function of pressure. The isotherms are shown in Figure 3.22.

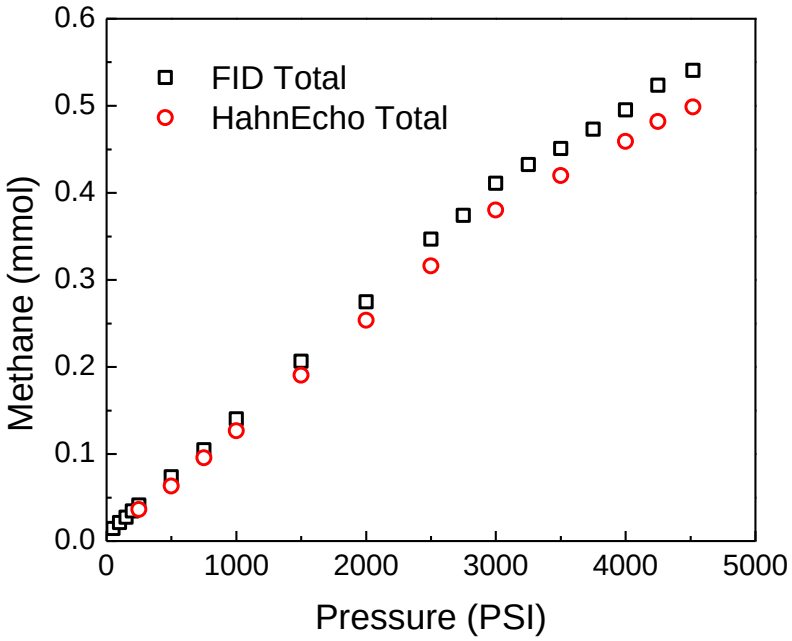

Figure 3.22 Comparison of FID and Hahn Echo intensity.

The ratio of the FID and the HahnEcho is shown in Figure 3.23.

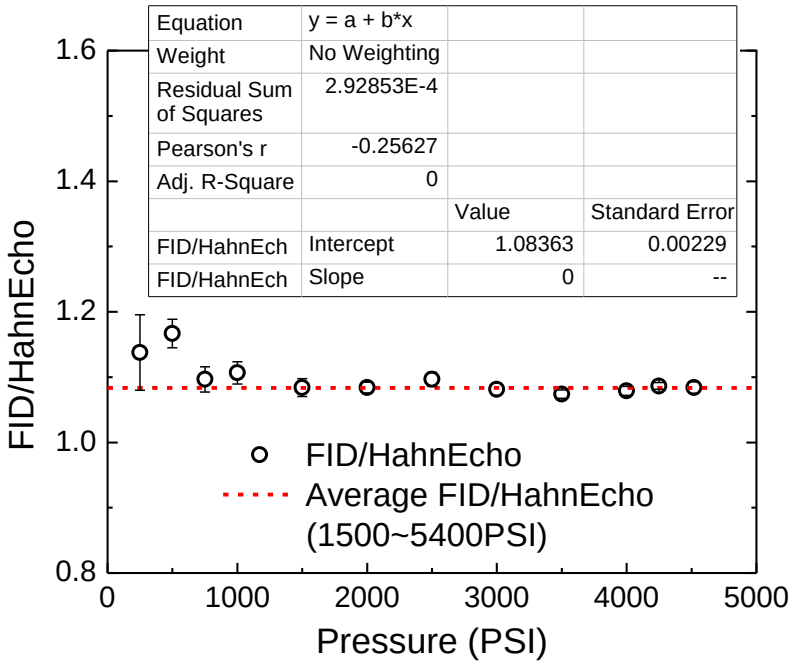

Figure 3.23 Ratio of FID intensity to Hahn Echo intensity.

It remains at a constant value for pressures greater than 1500PSI and increase slightly at lower pressure. The average value from $1500 \sim 4520$ PSI is 1.08, which is used for data processing in previous sections.

One possible explanation of the ratio is the "imperfect pulse space" of the probe coil, illustrated in Figure 3.24.

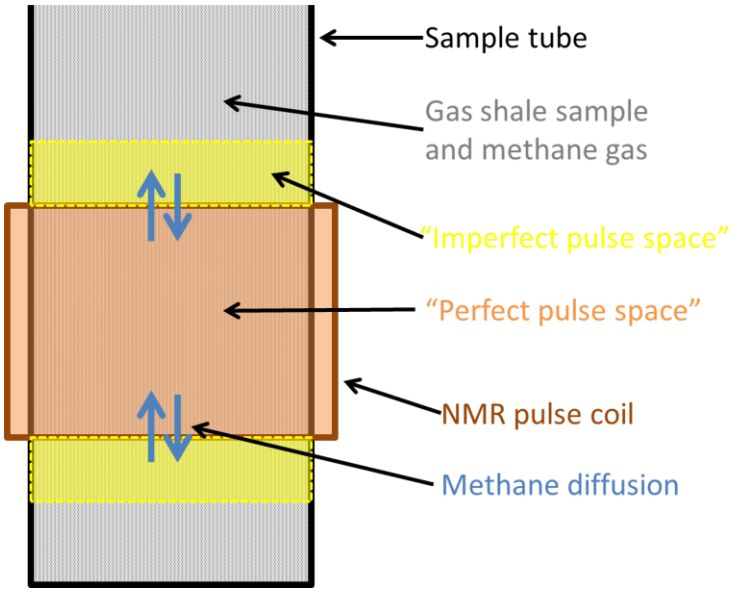

Figure 3.24 "Imperfect pulse space" of probe coil.

The NMR intensities measured in experiments are the sum of the signals from both the "perfect pulse space" and the "imperfect pulse space". The signals intensities of the FID and the HahnEcho should be identical in the "perfect pulsing space". However, in the "imperfect pulse space", since the pulse field is weaker than the pulse field inside the coil space, the echoes in the Hahn Echo pulse signal cannot be refocused perfectly and, therefore, are reduced. The FID signal doesn't have this part of reduction, so the intensity of the FID is larger than the intensity of the Hahn Echo pulse. Since this difference is only related to the geometry of the "imperfect pulse space" and the packed sample system, it is independent of pressure at the high pressure region, as shown in Figure 3.23.

When the system pressure is low enough, the self-diffusion coefficient of the methane gas will increase dramatically (Section 3.1.4), so the exchange of gas molecules between the "perfect pulse space" and the "imperfect pulse space" needs to be taken into account. In this case, the intensity of Hahn Echo sequence is further reduced due to the exchange of methane molecules, so the ratio of the FID intensity to the Hahn Echo intensity will increase at low pressure region, as shown in Figure 3.23.

3.5.4 Uncertainty Analysis

There are two main sources of uncertainty in the isotherm of gas stored in pores: the extrapolation of the FID data, and the extrapolation of the Hahn Echo data.

For the FID, the data is extrapolated back to the beginning in the time domain to acquire the total amount of methane in the system, as mentioned in Section 3.5.1. The uncertainty of extrapolation provides a part of the uncertainty in the amount of gas stored at each pressure, as shown in Figure 3.25.

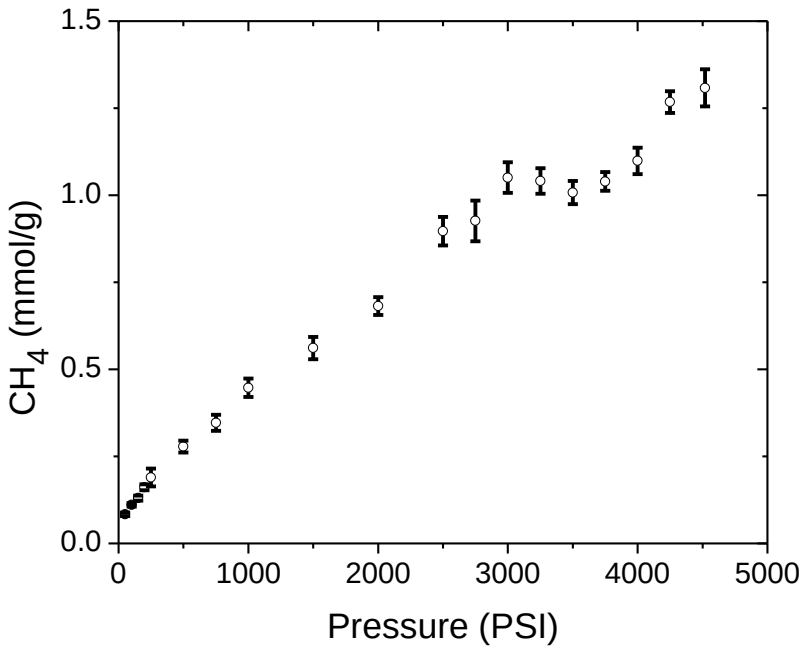

Figure 3.25 Uncertainty from FID extrapolation.

For the Hahn Echo data, as discussed in Section 3.3.2 and Section 3.5.2, a linear extrapolation is used to estimate the amount of methane stored in the pores and the packing ratio of the sample system. Due to the broad pore size distribution and the exchange of methane gas between the inter-particle space and the pore space, there is some discretion involved in determining the linear fitting range. Our method is as follows. Three continuous points around the boundary of the transition region and surface relaxation region (Figure 3.8) are extrapolated linearly. The average of three extrapolation results is used to estimate the gas

storage amount and the packing ratio of the sample. The difference among the results is used as the uncertainty of the packing ratio, as shown in Figure 3.26.

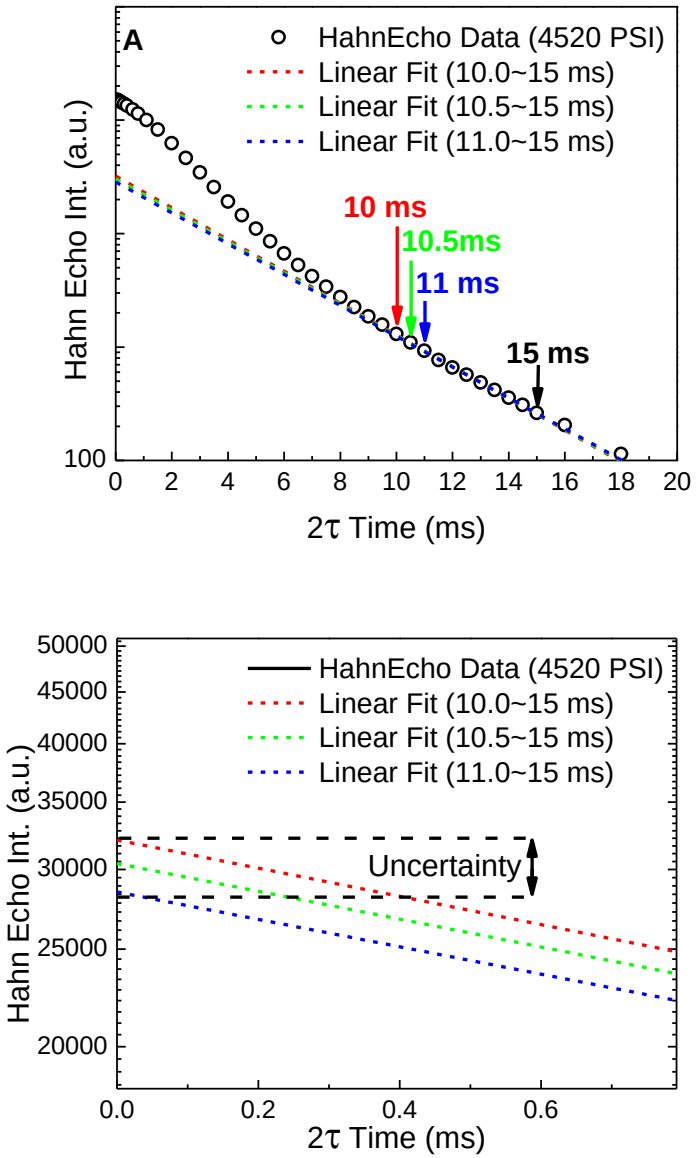

Figure 3.26 (A) Three linear fitting to evaluate the uncertainty of Hahn Echo extrapolation. (B) Zooming in to show the uncertainty due to the different fitting results.

The packing ratio result with uncertainty is $\Theta = 53.6\% \pm 0.6\%$. The isotherm including both uncertainties for the FID extrapolation and the Hahn Echo extrapolation are shown in Figure 3.27.

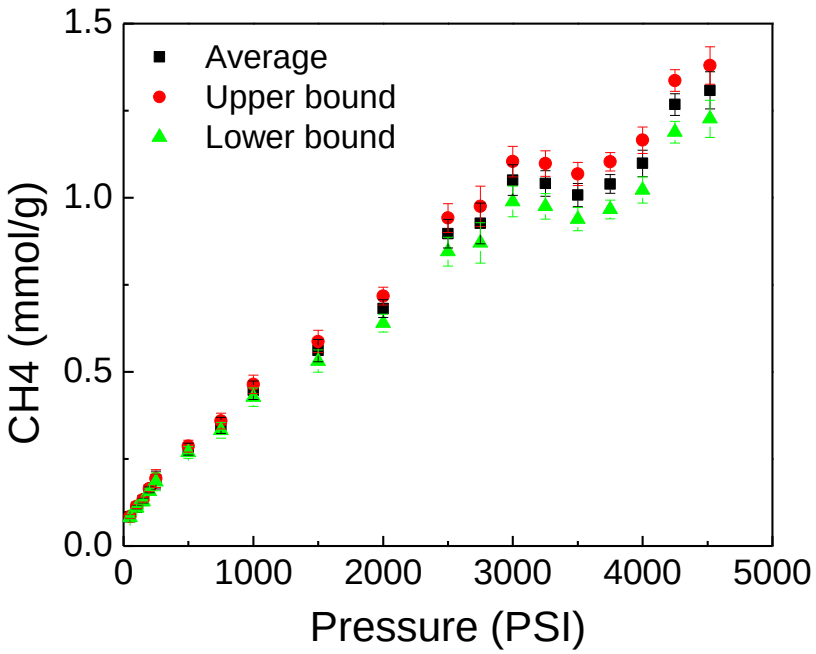

Figure 3.27 Isotherm with both uncertainties from FID and Hahn Echo extrapolations.

The uncertainty in the FID extrapolation describes the fluctuation of each point independently, so it needs to be taken into account when studying the details of the isotherm, such as the kinks at certain pressures. However, the uncertainty in the Hahn Echo extrapolation provides the upper and lower bounds, and it only effects on the overall data as it is from the multiplication of the packing ratio.

3.5.5 Effect of Methane Diffusion

The self-diffusion coefficient of methane gas strongly depends on the density and pressure, as introduced in Section 3.1.4. The larger self-diffusion coefficient of methane gas at lower pressure will also induce an enhancement of molecular exchange between the gas in the inter-particle space and the gas inside the pores. This can be observed in the pressure dependence of the Hahn Echo intensity, shown in Figure 3.28.

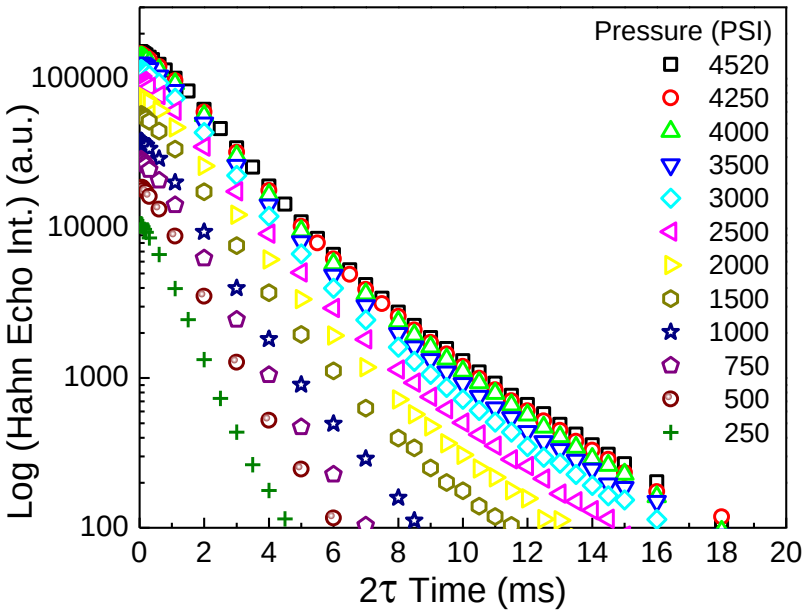

Figure 3.28 Pressure dependence of Hahn Echo intensity.

As the pressure decreases, the intensity of methane in the inter-particle space decays more quickly. This is most apparent in the region of $0 \sim 3$ ms in Figure 3.28. The enhancement of the self-diffusion coefficient of methane gas at a lower pressure induces faster relaxation according to Equation 3.26. Meanwhile, as the pressure gets lower, the Hahn Echo responses of methane in the inter-particle space and inside the pores are getting closer to each other. This makes it more difficult to distinguish these two species and to estimate the amount of methane storage.

Additional evidence of exchange enhancement is provided by the T_2 of the methane gas stored inside the pores. This can be calculated based on the slope of the linear fit, as discussed in Section 3.5.2. The results are shown in Figure 3.29. The pressure dependence of T_2 is observed clearly.

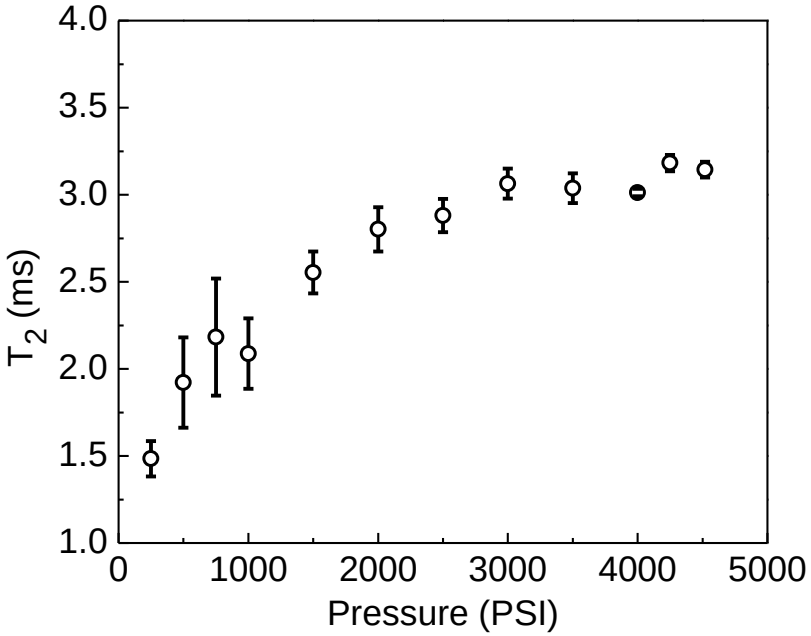

Figure 3.29 Pressure dependence of T_2 inside pores.

Under the fast-diffusion assumption, as discussed in Section 3.1.5, the surface relaxation rate does not depend on the self-diffusion coefficient of the probing molecules. One of the possible explanations is that the fast-diffusion assumption is not satisfied inside the gas shale pores system under the experimental conditions. This allows the surface relaxation rate to depend on the diffusion coefficient. But there are two pieces of evidence that prove this is not the case. First, as discussed in Section 3.1.4, when the density of methane gas increases at higher pressure, the self-diffusion coefficient will decrease, which should make the relaxation model diverge more strongly from the fast-diffusion assumption than the case at lower pressure. But the pressure dependence of the T_2 values, shown in Figure 3.29, only occurs at lower pressure, which is a contradiction of the prediction. Second, the packing ratio of the gas shale system should be independent of both the pressure and self-diffusion coefficient, so the estimated packing ratio should be a constant during the whole pressure region. However, the packing ratio data shows obvious pressure dependence at low pressures (Figure 3.30).

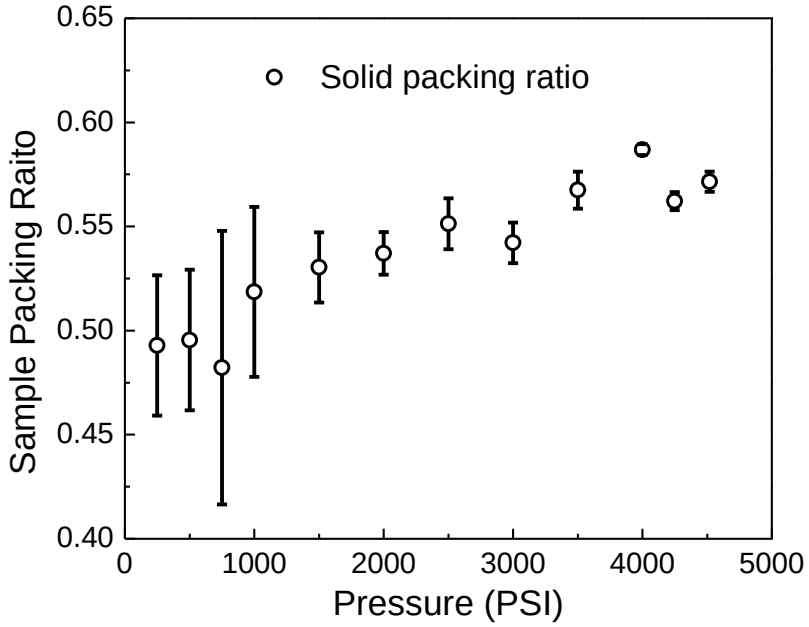

Figure 3.30 Pressure dependence of estimated solid packing ratio based on Hahn Echo intensity.

The pressure dependence of the estimated sample packing ratio indicates that, at low pressure, the Hahn Echo intensity of methane in the inter-particle space is overestimated and a partial signal of the gas inside the pores is underestimated due to exchange. The relatively large uncertainties, which occur at the low pressures, are also due to the enhanced molecular exchange which causes greater overlap in the Hahn Echo signals and makes the linear extrapolation more difficult. The exchange of molecules at low pressure also provides an explanation of the pressure dependence of T_2 in Figure 3.29 without violating the fast-diffusion assumption.

3.5.6 Issues of CPMG method

As discussed previously, in order to probe methane stored inside pores, it is crucial to distinguish the NMR signals of methane stored inside the pores from the signal of methane in the inter-particle space. The conventional CPMG Inverse-Laplace transformation method fails to distinguish the NMR signal accurately due to the reduction of the molecular diffusion effect.

The CPMG pulse sequence consists of a 90° excitation pulse and a train of 180° pulses, as discussed in Chapter 1. Each 180° pulse will reduce the diffusion effect during the interval time TE by refocusing the echo. The relaxation time of molecular diffusion through a magnetic field gradient as measured by the CPMG pulse sequence can be expressed [39]:

$$M_{Int}(t) = M_{\text{int}}^{0} \cdot \exp\left(-\left(\frac{1}{T_{Inter}^{B,S}} + a \cdot (\text{TE})^{2} \right) \cdot t \right) \tag{3.33}$$

where M_{int}^{0} is the NMR amplitude of methane molecules in the inter-particle space, $T_{\text{int}}^{B,S}$ is relaxation time based on bulk and surface relaxation, and $a = D \cdot (\gamma G)^{2} / 12$, where D is self-diffusion coefficient of gas molecular, γ is the gyromagnetic ratio, and G is the magnetic field gradient. By comparing Equation 3.33 with the Equation 3. 26 in Section 3.2.3, it is clear that the former decays more slowly since decay rate depends on t, but the latter one depends on t^{3}. The slower decay rate of the CPMG data causes the NMR signals of the inter-particle methane and the methane inside pores to mix together. This makes it too difficult to distinguish the storage part, as shown in Figure 3.31.

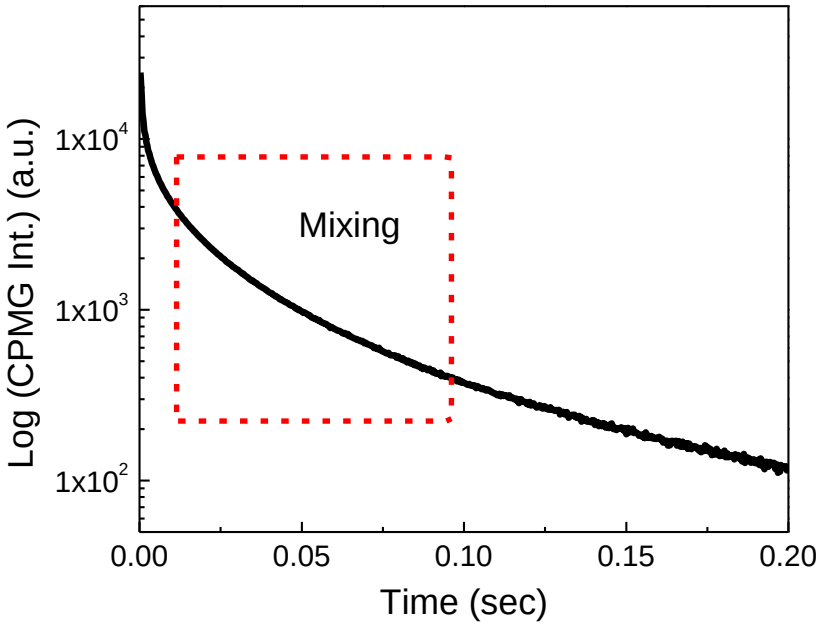

Figure 3.31 CPMG of gas shale sample.

3.5.7 Density Measurement Method and Issues

As mentioned earlier, the sample packing ratio is critical for the estimation of isotherms. Besides using the Hahn Echo method disscussed in Section 3.3.2, the packing ratio can also be estimated based on the sample density. Since the inner diameter of sample tube has been determined (Section 3.4.4), the packing ratio of the sample can be estimated:

$$\Theta = \frac{V_{sample}}{V_{total}} = \frac{4m_{sample}}{\rho_{sample} \cdot \pi d^2 l} \tag{3.34}$$

where V_{sample} and V_{total} are the volumes of sample and sample tube respectively, m_{sample} is the mass of the sample loaded into the sample tube, ρ_{sample} is the density of the gas shale sample, d is the inner diameter of sample tube, and l is the length of the packed sample system. In order to measure the sample density without filling the pores, 4-steps method is followed, shown in Figure 3.32.

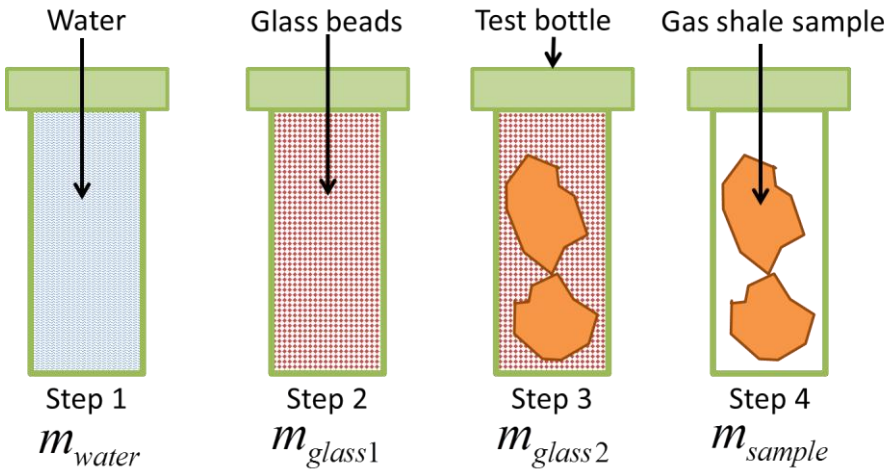

Figure 3.32 Glass beads filling method for density evaluation.

A sample bottle with cap is used in the density measurement. First, the bottle is fully filled with water. The volume of the bottle can be calculated by $V_{bottle} = m_{water} / \rho_{water}$, where m_{water} and ρ_{water} are the mass and density of water respectively. Second, the bottle is fully filled with glass beads (diameter $38 \sim 45\ \mu m$). The mass of the glass beads is measured (m_{glass1}). Third, two big sample chunks are loaded into the bottle and then the empty space is filled by glass beads again. The mass of filled glass beads without a sample is measured (m_{glass2}). Fourth, the mass of sample chunks is measured (m_{sample}). The density of sample can be calculated:

$$\rho_{sample} = m_{sample} \cdot \frac{\rho_{water}}{m_{water}} \cdot \frac{m_{glass1}}{m_{glass1} - m_{glass2}} \tag{3.35}$$

The whole measurement is repeated 5 times independently to evaluate the uncertainty. The estimated density is $2.30 \pm 0.09\ g/cm^3$; the relative uncertainty is about 4%. The packing ratio, based on the density measurement, is $\Theta_{density} = (47 \pm 2)\%$ (Equation 3.34). Compared with the packing ratio estimated by the Hahn Echo method, which is $\Theta_{HahnEcho} = (53.6 \pm 0.6)\%$, the result from density measurement is under-estimated and has much larger uncertainty, as shown in Figure 3.33.

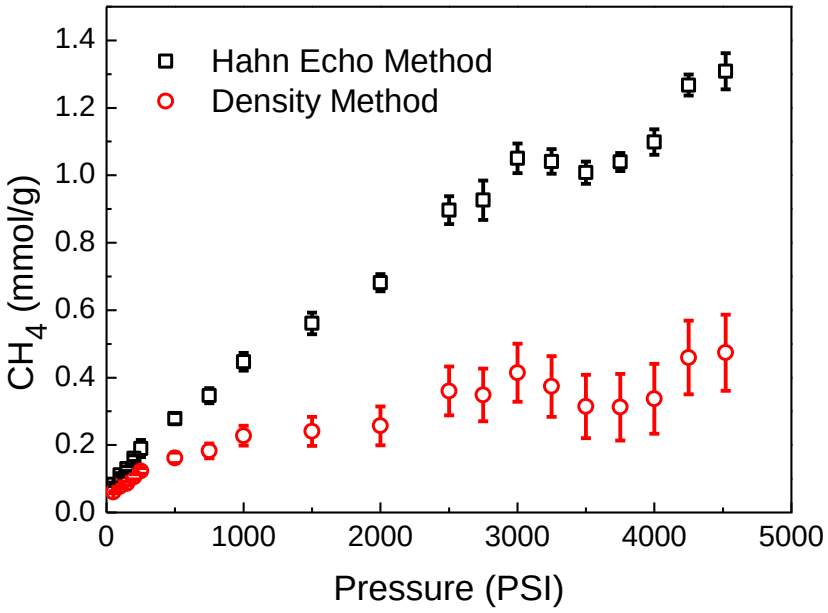

Figure 3.33 Comparison of Hahn Echo method and Density method.

One possible reason for the underestimation of storage gas using the density method is that the size of glass beads is too large for an accurate result. However, the method is difficult to execute when the size of glass beads gets smaller. The large uncertainty in the density is because most likely of the difficulty in packing the glass beads consistently. In light of these issues and disadvantages, we consider the density method to be unreliable.

REFERENCES

[1] Law BE, Curtis J. Introduction to unconventional petroleum systems. AAPG bulletin. 2002;86(11):1851-2.

[2] Stevens P. The 'Shale Gas Revolution': Developments and Changes. Chatham house. 2012.

[3] Duncan DC, Swanson VE. Organic-rich shale of the United States and world land areas: Geological Survey, Washington, DC; 1966.

[4] Hao F, Zou H, Lu Y. Mechanisms of shale gas storage: Implications for shale gas exploration in China. AAPG bulletin. 2013;97(8):1325-46.

[5] Milliken KL, Rudnicki M, Awwiller DN, Zhang T. Organic matter–hosted pore system, Marcellus formation (Devonian), Pennsylvania. AAPG bulletin. 2013;97(2):177-200.

[6] Gluyas J, Swarbrick R. Petroleum geoscience: John Wiley & Sons; 2013.

[7] Kenyon K, Straley, Gubelin, and Morris. Nuclear Magnetic Resonance Imaging: Technology for the 21st Century Oilfield Review. 1995;7(3).

[8] Coates GR, Xiao L, Prammer MG. NMR logging: principles and applications: Gulf Professional Publishing; 1999.

[9] Hürlimann M, Griffin D. Spin dynamics of Carr–Purcell–Meiboom–Gill-like sequences in grossly inhomogeneous B 0 and B 1 fields and application to NMR well logging. Journal of Magnetic Resonance. 2000;143(1):120-35.

[10] Venkataramanan L, Song Y-Q, Hurlimann MD. Solving Fredholm integrals of the first kind with tensor product structure in 2 and 2.5 dimensions. IEEE Transactions on Signal Processing. 2002;50(5):1017-26.

[11] De Hoog FR, Knight J, Stokes A. An improved method for numerical inversion of Laplace transforms. SIAM Journal on Scientific and Statistical Computing. 1982;3(3):357-66.

[12] Washburn KE, Birdwell JE. Updated methodology for nuclear magnetic resonance characterization of shales. Journal of Magnetic Resonance. 2013;233:17-28.

[13] Sun B, Wang H, Gidcumb S, Wu Y. NMR Isotherm Studies of Gas Shales. SPWLA 57th Annual Logging Symposium: Society of Petrophysicists and Well-Log Analysts.

[14] Kausik R, Fellah K, Rylander E, Singer PM, Lewis RE, Sinclair SM. NMR relaxometry in shale and implications for logging. SPWLA 56th Annual Logging Symposium: Society of Petrophysicists and Well-Log Analysts.

[15] Papaioannou A, Kausik R. Methane Storage in Nanoporous Media as Observed via High-Field NMR Relaxometry. Physical Review Applied. 2015;4(2):024018.

[16] Singer PM, Rylander E, Jiang T, McLin R, Lewis RE, Sinclair S. 1D and 2D

NMR core-log integration in organic shale. SCA2013-018 presented at the International Symposium of the Society of Core Analysts, Napa Valley, California; p. 16-9.

[17] Tan M, Mao K, Song X, Yang X, Xu J. NMR petrophysical interpretation method of gas shale based on core NMR experiment. Journal of Petroleum Science and Engineering. 2015;136:100-11.

[18] Lewis R, Singer P, Jiang T, Rylander E, Sinclair S, Mclin RH. NMR T_2 distributions in the Eagle Ford shale: reflections on pore size. SPE Unconventional Resources Conference-USA: Society of Petroleum Engineers.

[19] Fleury M, Romero-Sarmiento M. Characterization of shales using T 1–T 2 NMR maps. Journal of Petroleum Science and Engineering. 2016;137:55-62.

[20] Carey JW, Lei Z, Rougier E, Mori H, Viswanathan H. Fracture-permeability behavior of shale. Journal of Unconventional Oil and Gas Resources. 2015;11:27-43.

[21] Soeder DJ. Porosity and permeability of eastern Devonian gas shale. SPE Formation Evaluation. 1988;3(01):116-24.

[22] Cussler EL. Diffusion: mass transfer in fluid systems: Cambridge university press; 2009.

[23] Hirschfelder J, Bird RB, Curtiss CF. Molecular theory of gases and liquids. 1964.

[24] Oosting P, Trappeniers N. Proton-spin-lattice relaxation and self-diffusion in methanes: IV. Self-diffusion in methane. Physica. 1971;51(3):418-31.

[25] Harris K. The density dependence of the self-diffusion coefficient of methane at− 50°, 25° and 50° C. Physica A: Statistical Mechanics and its Applications. 1978;94(3):448-64.

[26] Bird RB, Stewart WE, Lightfoot EN. Transport phenomena: John Wiley & Sons; 2007.

[27] Brownstein KR, Tarr C. Importance of classical diffusion in NMR studies of water in biological cells. Physical Review A. 1979;19(6):2446.

[28] Drain L. The broadening of magnetic resonance lines due to field inhomogeneities in powdered samples. Proceedings of the Physical Society. 1962;80(6):1380.

[29] Glasel JA, Lee K. Interpretation of water nuclear magnetic resonance relaxation times in heterogeneous systems. Journal of the American Chemical Society. 1974;96(4):970-8.

[30] Majumdar S, Gore J. Studies of diffusion in random fields produced by variations in susceptibility. Journal of Magnetic Resonance (1969). 1988;78(1):41-55.

[31] Song YQ. Using internal magnetic fields to obtain pore size distributions of porous media. Concepts in Magnetic Resonance Part A. 2003;18(2):97-110.

[32] Sen PN, Axelrod S. Inhomogeneity in local magnetic field due to susceptibility contrast. Journal of applied physics. 1999;86(8):4548-54.

[33] Jackson JD. Electrodynamics: Wiley Online Library; 1975.

[34] Johnson Jr C, Waugh J. Nuclear relaxation in gases: Mixtures of methane and oxygen. J Chem Phys. 1961;35(6):2020-4.

[35] Kennard EH. Kinetic theory of gases. 1938.

[36] Levitt MH. Spin dynamics: basics of nuclear magnetic resonance: John Wiley & Sons; 2001.

[37] Streever R, Carr H. Nuclear magnetic resonance of Xe 129 in natural xenon. Physical Review. 1961;121(1):20.

[38] Hari P, Chang C, Kulkarni R, Lien J, Watson A. NMR characterization of hydrocarbon gas in porous media. Magnetic resonance imaging. 1998;16(5):545-7.

[39] Slichter CP. Principles of magnetic resonance: Springer Science & Business Media; 2013.

[40] Kudryavtsev A, Linert W. Physico-chemical Applications of NMR: A Practical Guide: World Scientific; 1996.

[41] Hrovat M, Patz S. Pulse Sequence for elimination of RF receiver coil ring down. Proc ISMRM, Glasgow, Scotland, UK. 2001.

[42] H.Levitt M. spin dynamics. Chichester, New York, Weinheim, Brisbane, Singapore, Toronto: John Wiley&Sons, Ltd; 2001.

CHAPTER 4. NMR STUDY OF GAS SHALE SAMPLES

4.1 Introduction

The NMR method introduced in Chapter 3 is applied to test several different gas shale samples. The results are presented and analyzed in this chapter.

In petrophysics, there are several specific parameters and measurements which are used to evaluate gas shale samples. In order to understand that preliminary information, these parameters are introduced at first.

4.1.1 Standard Measurement Methods

The total organic carbon (TOC) is the amount of carbon in an organic compound. It is usually presented as a weight percentage and quantifies the amount of organic material in gas shale samples.

The Rock-Eval (RE) pyrolysis experiment is used as a standard characterization method for petroleum samples. There are four basic parameters obtained:

1. S_1 is the amount of free hydrocarbons (gas and oil) in the sample. It is presented in milligrams of hydrocarbon per gram of rock.
2. S_2 is the amount of hydrocarbons generated through thermal cracking of nonvolatile organic matter. S_2 is an indication of the potential for producing oil and/or gas.
3. S_3 is the amount of CO_2 produced during pyrolysis of kerogen. The unit is milligrams of CO_2 per gram of rock. S_3 is also an indication of the amount of oxygen in the kerogen and it can be used to calculate the oxygen index.
4. T_{max} is the kerogen cracking temperature at which the maximum release of

hydrocarbons from cracking of kerogen occurs during pyrolysis (S2 peak). T_{max} is an indication of the stage of maturation of the organic matter.

There are four more parameters derived from those mentioned above. These are generally used to characterize the type and maturity of organic matter in petroleum source rocks:

1. HI is the hydrogen index. ($HI = [100 \times S2]/TOC$). HI is a parameter used to characterize the origin of the organic matter. Marine organic matter generally has higher HI than terrestrial. The typical range of HI values in geological samples is from ~100 to 600.
2. OI is the oxygen index. ($OI = [100 \times S3]/TOC$). OI is a parameter that correlates with the ratio of O to C. Generally OI is high for land plants. OI values range from near 0 to ~150.
3. PI is the production index. ($PI = S1/[S1 + S2]$). PI generally is used to characterize the evolution level of the organic matter.
4. PC is pyrolyzable carbon. ($PC = 0.083 \times [S1 + S2]$). PC corresponds to the carbon content of hydrocarbons volatilized and pyrolyzed during the analysis.

Generally, there are two measures to evaluate the maturation of the organic matter based on Rock-Eval (RE) pyrolysis:

1. The ratio of HI to OI, as shown in Figure 4.1[1].

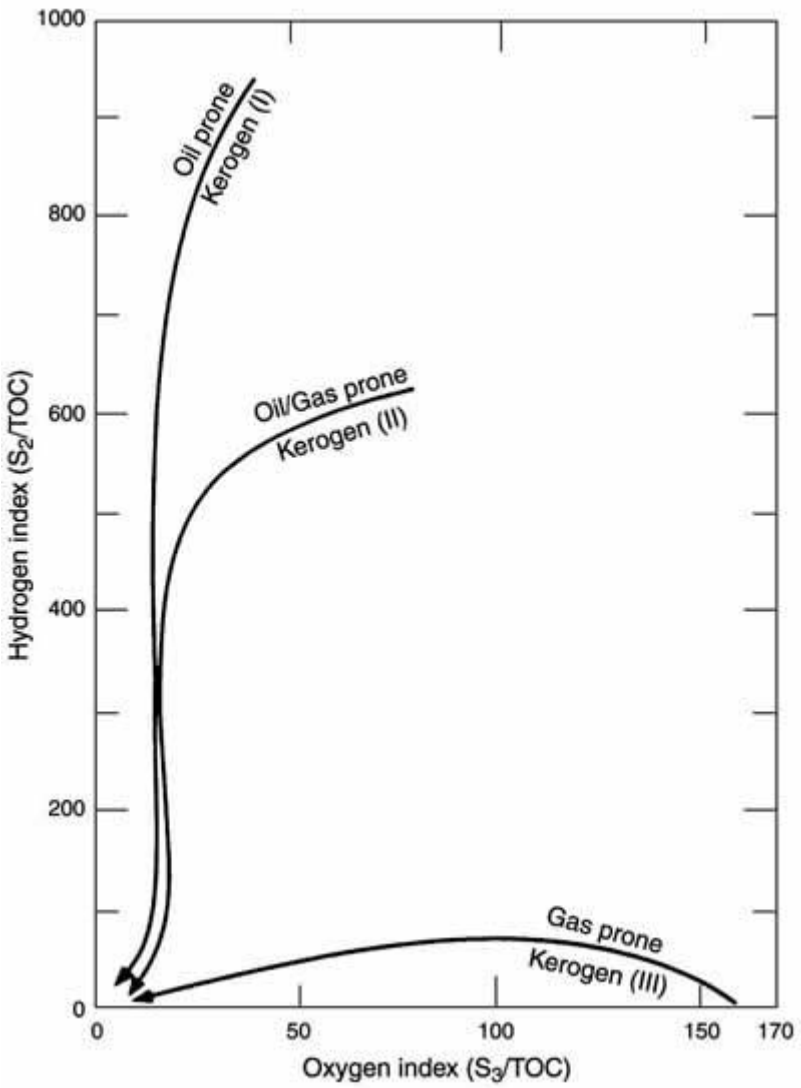

Figure 4.1 Hydrogen index/oxygen index plot from Rock-Eval pyrolysis data.

2. T_{max} range. $T_{max} \approx 400^{\circ} \sim 430^{\circ}$ represents immature organic matter; $T_{max} \approx 435^{\circ} \sim 450^{\circ}$ represents mature or an oil zone; $T_{max} > 450^{\circ}C$ represents the overmature organic matters.

The Ro value, also called Vitrinite reflectance, is a measure of the percentage of incident light reflected from the surface of vitrinite particles in a sedimentary rock. It is also referred to as %Ro. Generally, the Ro value results are presented as a mean value of all vitrinite particles measured in an individual sample.

4.1.2 Sample Information

All measured samples are listed in table 4.1. The source information of most is also

provided.

Sample Name	Sample Source
CN-SH-5-2	China-Sichuan-Changning-Longmaxi (Outcrop)
CN-SH-6-2	China-Sichuan-Changning-Longmaxi (Outcrop)
Marcellus 3-4	US-Marcellus (Outcrop)
T1	China-Liaohe-Shitan-Permian (well)
T9	China-Liaohe-Shitan-Permian (well)
ZET-1	Eerduosi-paleozoic (core)
DST-1	China-Sichuan-Doushantuo (Outcrop)
QZS	China-Sichuan-Qiongzhusi (Outcrop)
YS108	China-Sichuan-Zhaotong-Longmaxi (well)
Pyrolysis	Lab Aging
JY1#	China-Jiaoshiba-Jiaoye#1-Longmaxi
Coal	
SDTL-2014	

Table 4.1 Sample names and source information.

Most of the samples are from China. *Marcellus 3-4* is from the US and *Houston pyrolysis* is thermally aged in the lab.

The RE pyrolysis experiment results, TOC and Ro values of several samples are also provided and listed in Table 4.2. According to Section 4.1.1, *HI, OI, PI,* and *PC* are calculated based on the results in Table 4.2 and listed together with TOC and Ro values in table 4.3.

The pyrolysis results of several particular samples, such as *YS108, Z101-131, ZET-1, CH-SH-5-2*, only have one significant figure, which induce a large relative uncertainty. The Ro values are only provided for a few samples.

	T_{max} (C^o)	S1 (mg/g)	S2 (mg/g)	S3 (mg/g)	TOC (%)	Ro
ZET-1	591	0.01	0.02	0.01	10.00	
DST-1	607	0.02	0.09	0.09	13.00	
T1	563	0.02	0.55	0.22	3.44	
T9	576	0.01	0.06	0.10	3.90	2.00
CN-SH-5-2	607	0.01	0.02	0.11	3.55	
Z101-131		0.01	0.01	0.01		
YS108	607	0.00	0.01	0.06	4.10	4.70
Marcellus 3-4	468	0.09	0.19	0.11	9.00	1.77
JY1H	602	0.01	0.02	0.00	6.20	
CN-SH-6-2					6.7	
QZS					2	
pyrolysis					3.30	

Table 4.2 RE pyrolysis results, TOC and Ro values of several samples.

	T_{max} (C^o)	TOC (%)	Ro	HI	OI	PI	PC
ZET-1	591.00	10.00		20.00	10.00	0.33	0.00
DST-1	607.00	13.00		69.23	69.23	0.11	0.01
T1	563.00	3.44		1598.84	639.53	0.03	0.05
T9	576.00	3.90	2.00	153.85	256.41	0.06	0.01
CN-SH-5-2	607.00	3.55		56.34	309.86	0.08	0.00
Z101-131						0.50	0.00
YS108	607.00	4.10	4.70	24.39	146.34	0.00	0.00
Marcellus 3-4	468.00	9.00	1.77	211.11	122.22	0.30	0.02
JY1H	602.00	6.20		32.26	0.00	0.50	0.00
CN-SH-6-2		6.70					
QZS		2.00					
pyrolysis		3.30					

Table 4.3 Calculated RE pyrolysis results, TOC and Ro values of several samples.

According to the T_{max} value, the organic matters of all the samples are overmatured, which is expected for gas shale samples.

4.2 NMR Experimental Results

4.2.1 Spectra under Vacuum

Several samples were tested by NMR under vacuum conditions and the ^1H spectra are shown in Figure 4.2.

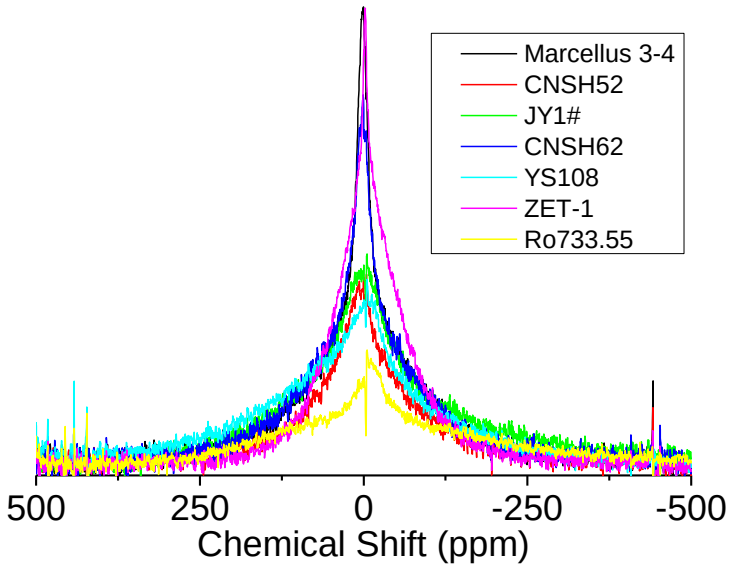

Figure 4.2 ^{1}H NMR spectra of gas shale samples under vacuum condition.

Since the intensity of the NMR signal is proportional to the total number of spins, the concentration of protons in a sample can be estimated through the integration area of the NMR spectra. The results are shown in Table 4.4.

Sample	Protons/Mass (mmol/g)	TOC (%)	Ratio (TOC/Protons)
CN-SH-5-2	2.55	3.55	1.39
CN-SH-6-2	2.28	6.70	2.94
JY1	3.31	6.20	1.88
Marcellus	2.89	9.00	3.11
QZS-1	0.34	2.00	5.86
pyrolysis	1.86	3.30	1.77
YS108	2.90	4.10	1.42
ZET-1	1.74	10.00	5.74

Table 4.4 Proton concentration of gas shale samples.

Each spectrum in Figure 4.2 can be separated into two peaks with different peak widths, as shown in Figure 4.3.

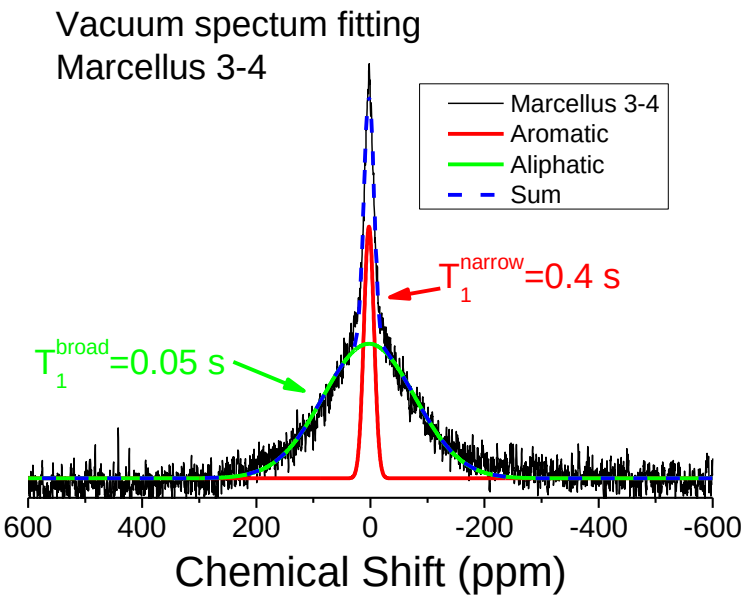

Figure 4.3 An illustration of peaks separation fitting of sample *Marcellus 3-4*

It is possible that the narrow peak is from the protons on aliphatic carbons and the broad one is from protons on aromatic carbons. The stronger mobility of aliphatic carbons may reduce the peak width [2]. However, the longitudinal relaxation time measurement argues against the two peak components. The protons on aromatic carbons generally have a longer T_1 time than those on aliphatic carbons [3, 4]. According to the experimental results shown in Table 4.5, the narrow peak has a longer longitudinal relaxation time ($T_1 = 0.4s$) than the broad peak ($T_1 = 0.05s$). The measurement result is shown in Figure 4.4.

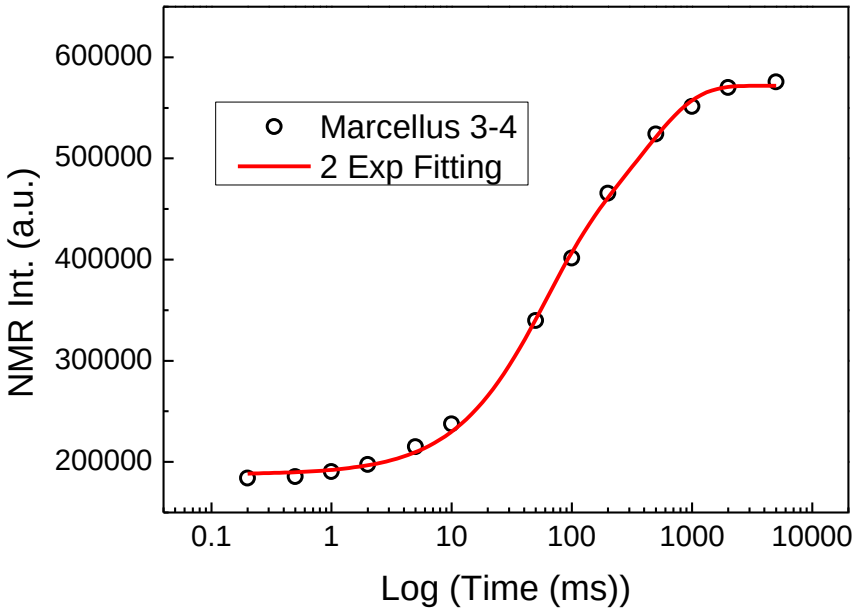

Figure 4.4 The measurement result of *Marcellus 3-4*.

All the spectra have been processed and the results are listed in Table 4.5.

	Narrow Peak			Broad Peak		
	Amplitude (a.u.)	Width (ppm)	Center (ppm)	Amplitude (a.u.)	Width (ppm)	Center (ppm)
CN-SH-5-2	234719	50	6.4	833644	199	-3.2
CN-SH-6-2	267739	26	2	1.25E+06	174	4.3
JY1	335413	64	3.3	1.20E+06	267	8.4
Marcellus	251245	18	2.6	1.23E+06	161	2.6
QZS-1	34427	21	-4.7	1.79E+05	143	-4.7
Ro733.55	104023	42	-11	7.33E+05	301	-20
YS108	206921	55	-7.3	1.20E+06	267	-12
ZET-1	139475	17	-2.2	1.44E+06	116	-6.6

Table 4.5 Vacuum spectra analyzed results.

4.2.2 Hahn Echo Data under Vacuum

Several samples are also measured with a Hahn Echo pulse under vacuum. The data is shown in Figure 4.5.

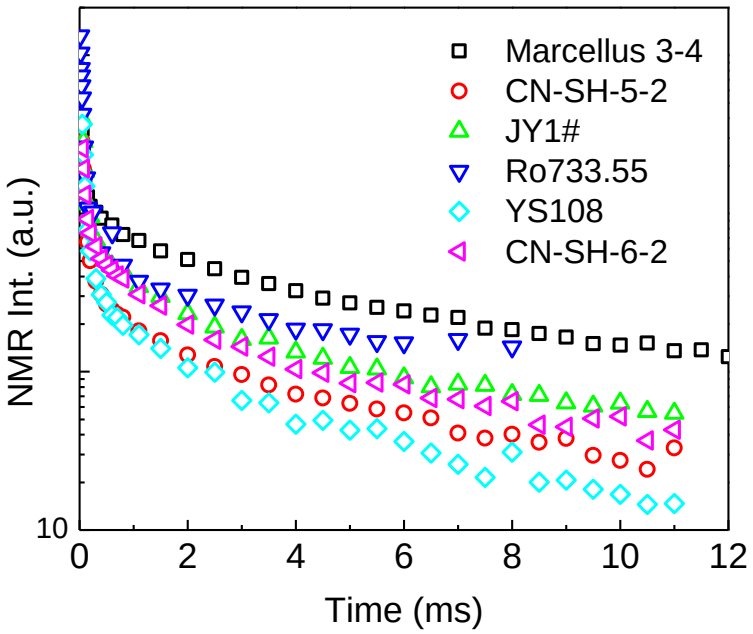

Figure 4.5 Hahn Echo data of gas shale samples under vacuum.

An empirical fitting with three exponential components is used to primarily analyze the Hahn Echo data and the results are listed in Table 4.6.

	Short T_2 NMR Amp. (a.u.)	Short T_2 (ms)	Medium T_2 NMR Amp. (a.u.)	Medium T_2 (ms)	Long T_2 NMR Amp. (a.u.)	Long T_2 (ms)
Marcellus 3-4	7631	0.041	738	1.5	360	10.1
CN-SH-5-2	8164	0.038	525	0.22	236	2.4
JY1	9531	0.04	962	0.21	462	2.2
pyrolysis	15728	0.03	1105	0.6	202	24
YS108	10512	0.037	828	0.19	241	2.2

Table 4.6 Empirical fitting results of Hahn Echo data.

These components may be from protons in different chemical environments. The short $_{T2}$ components may be from the protons in kerogen, and the long T_2 components are possibly from the gas trapped inside the shale samples. However, the previous studies of the Hahn Echo measures of gas shale samples under a high magnetic field are rare, so there isn't a confirmed conclusion at the current stage.

4.2.3 Spectra under High Pressure

Spectra of gas shale samples with high-pressure methane at 3500 PSI except for the *Coal* (175 PSI) and *T1M* (1600 PSI) are presented in Figure 4.6.

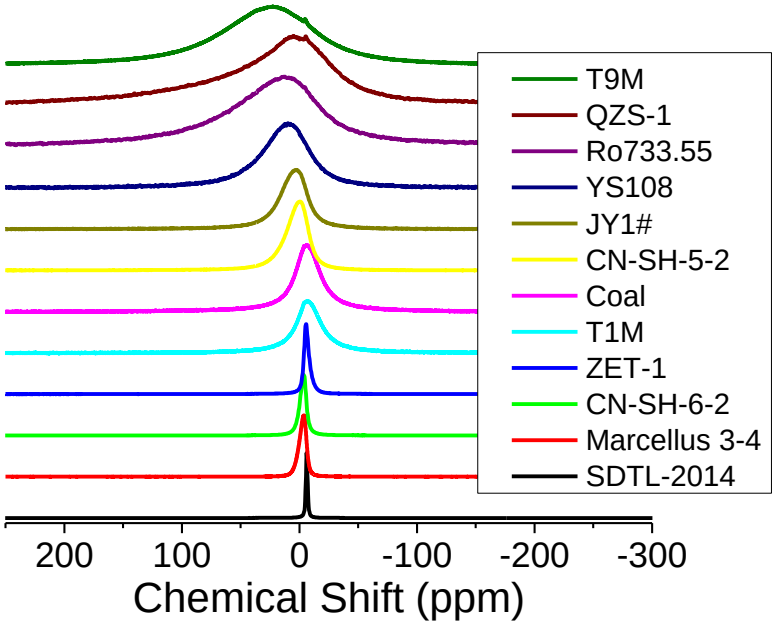

Figure 4.6 ^{1}H spectra of high-pressure methane-loaded gas shale samples at 3500 PSI except *Coal* (175 PSI) and *T1M* (1600 PSI)

As discussed in Section 3.3.3, the widths of the spectra reflect the magnetic field inhomogeneity, which is induced by the paramagnetic impurities in the gas shale samples. Therefore, it is possible to evaluate the strength of paramagnetic impurities inside gas shale samples.

4.2.4 Hahn Echo Data under High Pressure

The Hahn Echo data of several high pressure (4520 PSI) methane gas-loaded shale samples are shown in Figure 4.7.

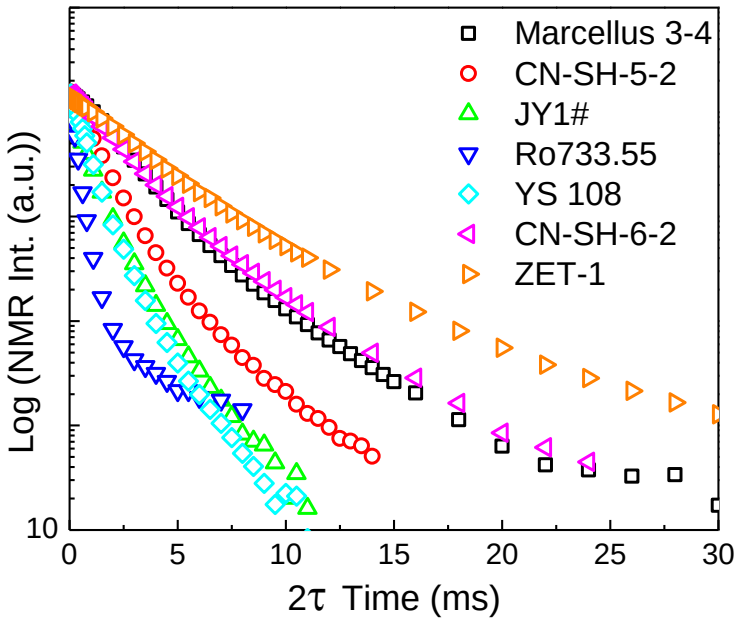

Figure 4.7 Hahn Echo data of high pressure (4520 PSI) methane gas loaded into several shale samples.

Based on the method introduced in Chapter 3, the Hahn Echo decay curves of each sample can be separated into two components. The longer component is from methane stored inside the pores. The T_2 values of the longer components are listed in Table 4.7.

Samples	Methane in pores	
	T_2 (ms)	Uncertainty (ms)
Marcellus 3-4	3.15	0.05
CN-SH-5-2	2.3	0.2
JY1	1.46	0.04
Pyrolysis	4.6	0.4
YS108	1.51	0.03
CN-SH-6-2	3.34	0.05
ZET	7.2	0.2

Table 4.7 T_2 values of methane (4520 PSI) stored in pores of gas shale samples.

4.2.5 Isotherms of Gas Shale Samples

The isotherms of samples are shown in Figure 4.8.

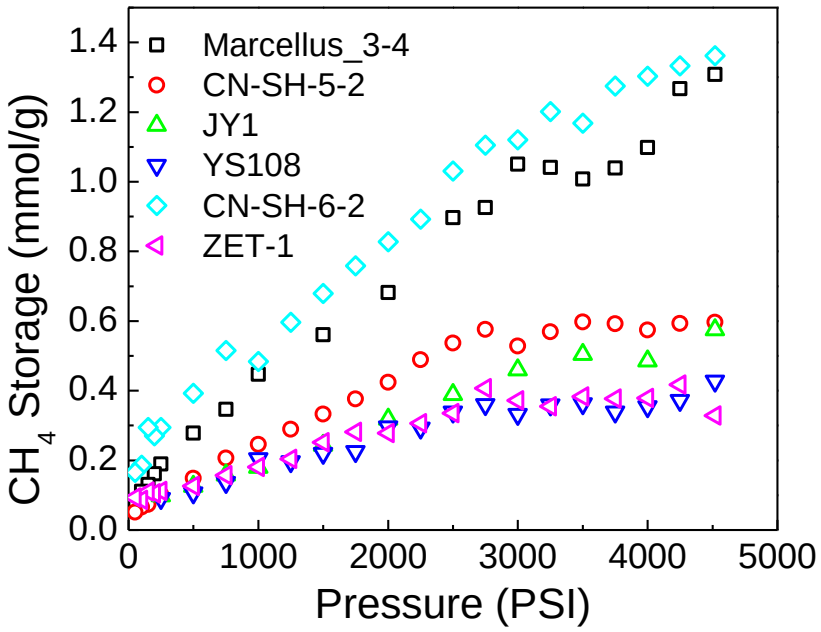

Figure 4.8 Isotherms of shale samples.

The isotherms of each sample with uncertainties from both the FID extrapolation and the Hahn Echo data fitting are also listed below (the isotherm of Marcellus 3-4 has been provided in Chapter 3). The error bar shown at each data point is the uncertainty from the FID extrapolation. The red and green lines are the upper and lower bonds derived from the Hahn Echo data fitting. The Θ value shown in each isotherm is the empty space packing ratio estimated from the Hahn Echo data.

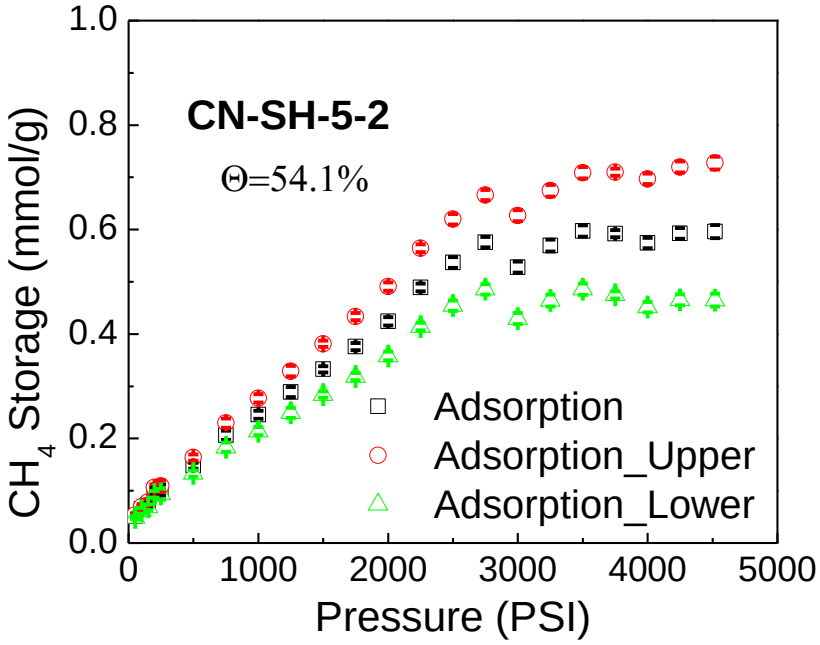

Figure 4.9 Isotherm and uncertainty of shale sample *CN-SH-5-2*.

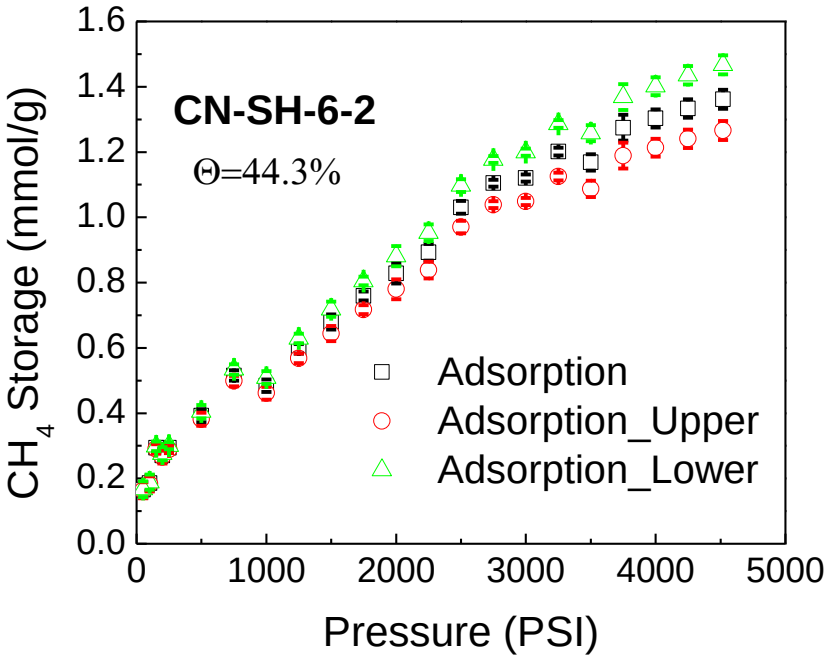

Figure 4.10 Isotherm and uncertainty of shale sample *CN-SH-6-2*.

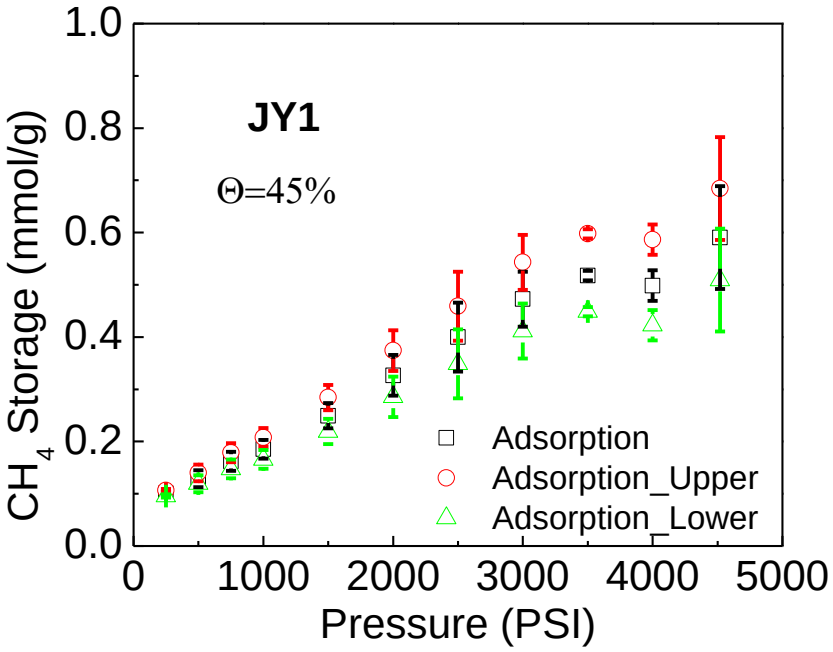

Figure 4.11 Isotherm and uncertainty of shale sample *JY1*.

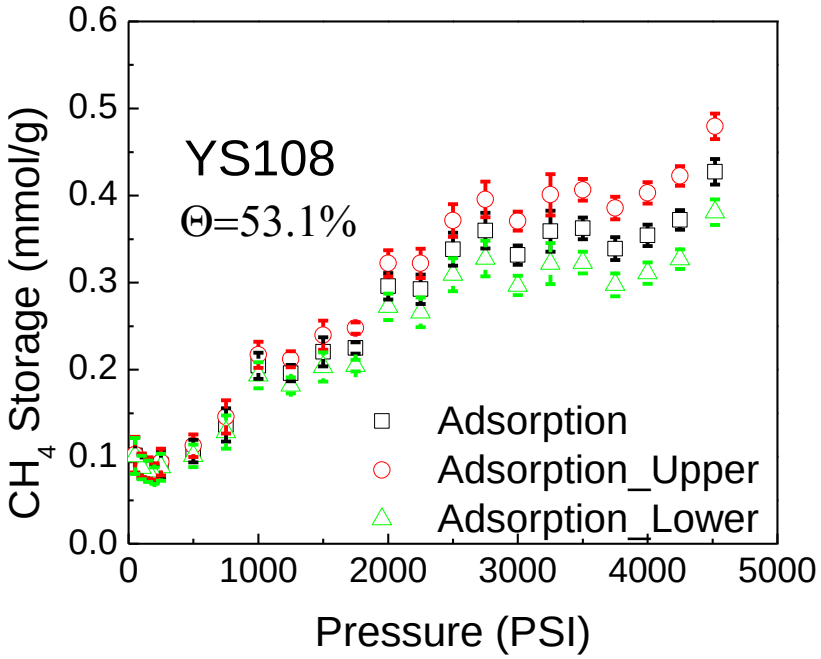

Figure 4.12 Isotherm and uncertainty of shale sample *YS-108*.

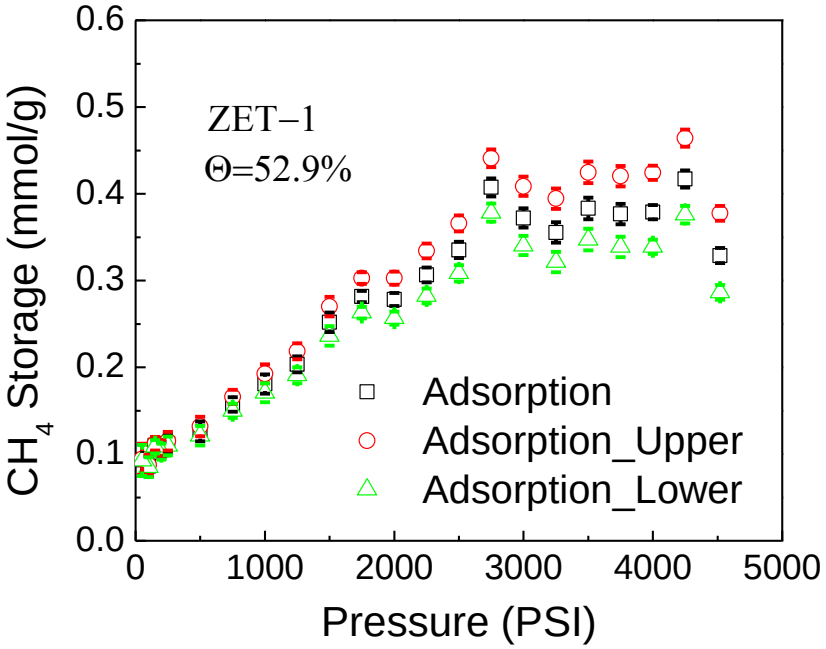

Figure 4.13 Isotherm and uncertainty of shale sample *ZET-1*.

4.3 Discussions

4.3.1 TOC/ Protons vs. Maturity

The ratio of carbon to protons ($\propto$ TOC/protons) is expected to relate to the maturities of samples. Generally, a higher maturity will result in a higher carbon to proton ratio. In order to check for a the correlation, a plot of T_{max} vs. TOC/protons, which is based on the data in Table 4.3 and 4.4, is shown in Figure 4.14.

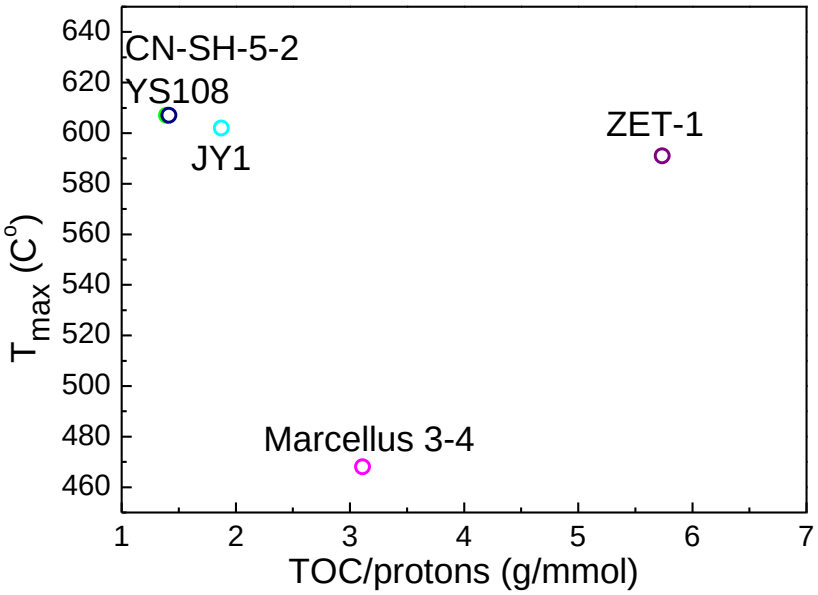

Figure 4.14 Plotting of T_{max} vs. TOC/protons.

If we treat *Marcellus 3-4* as an outlier and focus on the other samples, a good linear correlation can be observed, as shown in Figure 4.15.

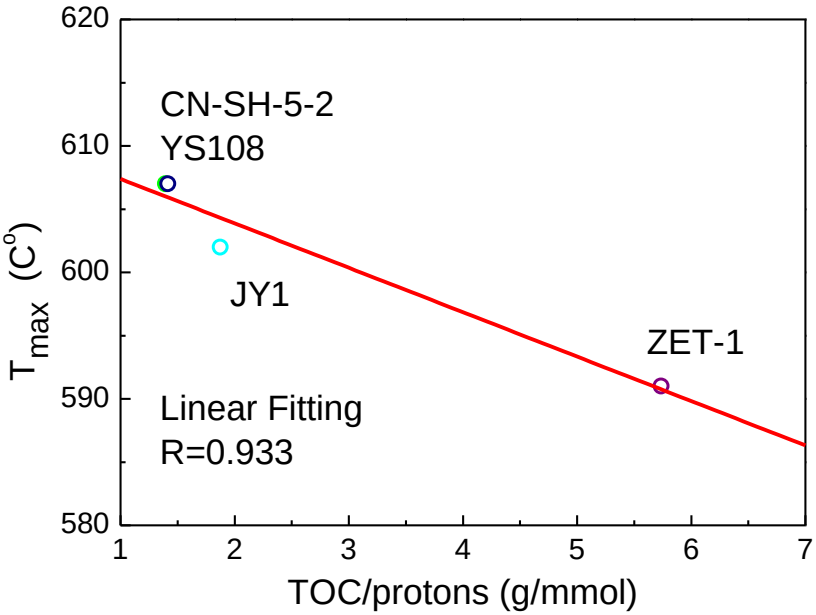

Figure 4.15 Correlation of T_{max} vs. TOC/protons.

The difference between *Marcellus 3-4* and the other samples is most likely due to

differences in the geological evolution of the formation.

4.3.2 Protons vs. HI

The HI parameter is expected to relate to the proton number tested by NMR. The plot of HI vs. Protons is shown in Figure 4.16.

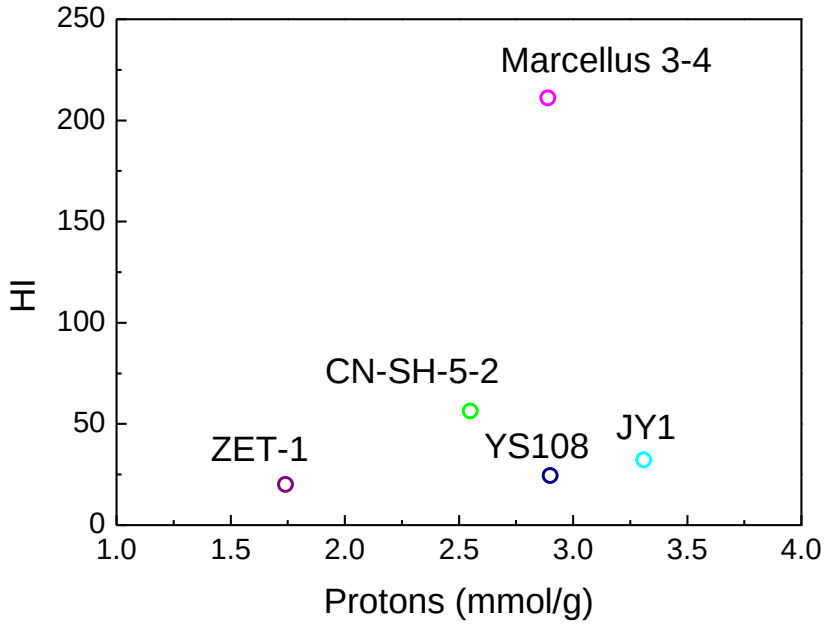

Figure 4.16 Plot of HI vs. protons.

Again, the *Marcellus 3-4* is an outlier due to the much higher HI value.

4.3.3 Hahn Echo Data under Vacuum

As discussed in Chapter 3, the transverse relaxation mechanism of the methane stored inside the pores of shale samples is dominated by surface relaxation. It highly depends on the pore surface properties (the surface relaxation sink strength). If it's assumed that the pore surface properties are affected by the prontons of the narrow peak in Figure 4.2, there may be a correlation between the T_2 values in Table 4.7 and the properties of the narrow peak shown. A plot of the high-pressure long component T_2 vs. vacuum narrow peak T_2^* is shown in Figure 4.17.

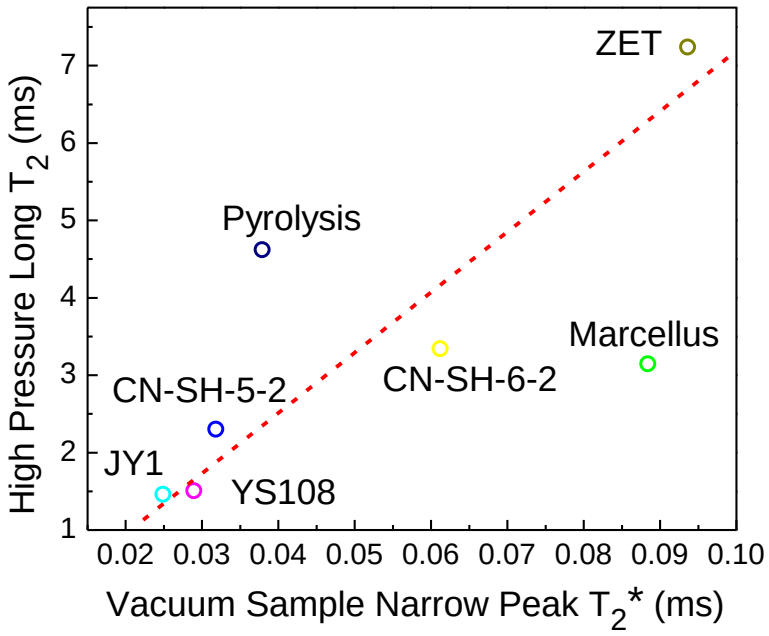

Figure 4.17 High-pressure long component T_2 vs. vacuum sample narrow peak T_2^*

There are two outliers: the *pyrolysis* and *Marcellus 3-4*. This is reasonable because the *Pyrolysis* is not real shale but a synthetic lab-aged sample; *Marcellus 3-4* is shale from the US, so it could be much different from all other samples which are from China.

4.3.4 Kinks in Isotherms

There are several kinks in the isotherms of Figure 4.13. They are summarized in Table 4.8.

Sample name	Kinks pressure (PSI)		
Marcellus 3-4	3500		
CN-SH-5-2	3000	4000	
CN-SH-6-2	1000	3500	
YS108	1750	3000	3750
ZET-1	2000	3250	4520

Table 4.8 Summary of kinks on isotherms.

These kinks are not normally observed in other measurements, therefore, some discussion is necessary.

The kinks are repeatable. For the same sample batch, if the high-pressure measurements

are repeated, the results show an identical isotherm. Therefore, these are not random errors from uncontrolled factors.

The kinks also depend on certain properties of samples which are different in various samples. According to Table 4.8, the kinks occur at different pressures in different samples. Therefore, they do not arise from any systematic flaws in the experimental method or set up.

One possible reason for this is that, at high pressure, methane may dissolve into kerogen and we lose some of the NMR signal due to much stronger dipolar interactions with the kerogen molecules.

The other possible reason is the deformation of the OM-hosted pores [5-8]. Kerogen is an organic material which is relatively ‘soft’ and can be deformed under high-pressure conditions. These deformations are reversible since the identical isotherm is achieved by multiple times of high-pressure measurements on the same batch of samples.

4.4 Correlation between Isotherms and other parameters

It would be very helpful in real applications if a parameter can be found to predict the methane storage capability. Several potential parameters were tested for any correlations.

4.4.1 TOC

TOC is one of the more popular controls when determining the storage capability of shale samples. The correlation between the methane storage at 4520 PSI and TOC is shown in Figure 4.18.

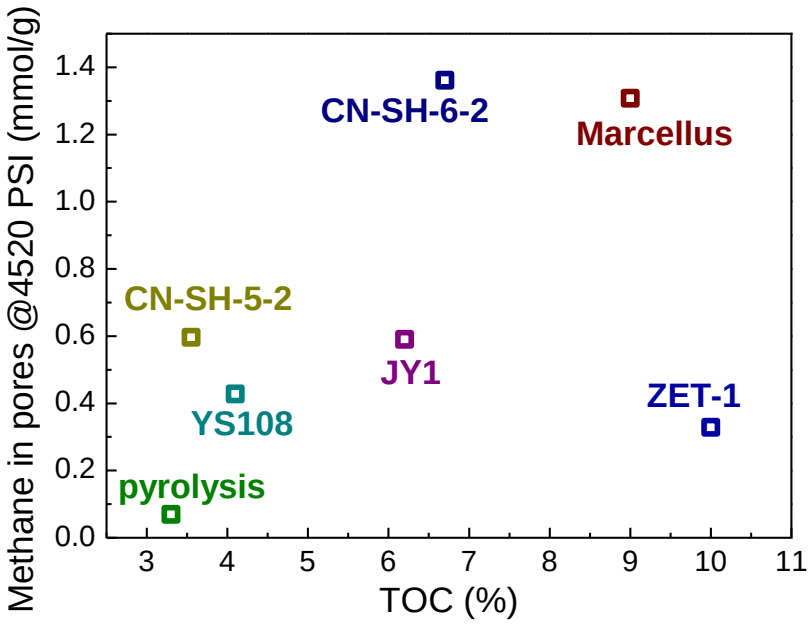

Figure 4.18 Methane storage at 4520 PSI vs. TOC.

According to the result, except for the *ZET-1* sample, the other samples show that the TOC has a positive correlation with the methane stored inside pores.

4.4.2 Total Protons Concentration

The correlation between the proton concentration in each sample and the methane storage amount at 4520 PSI is shown in Figure 4.19.

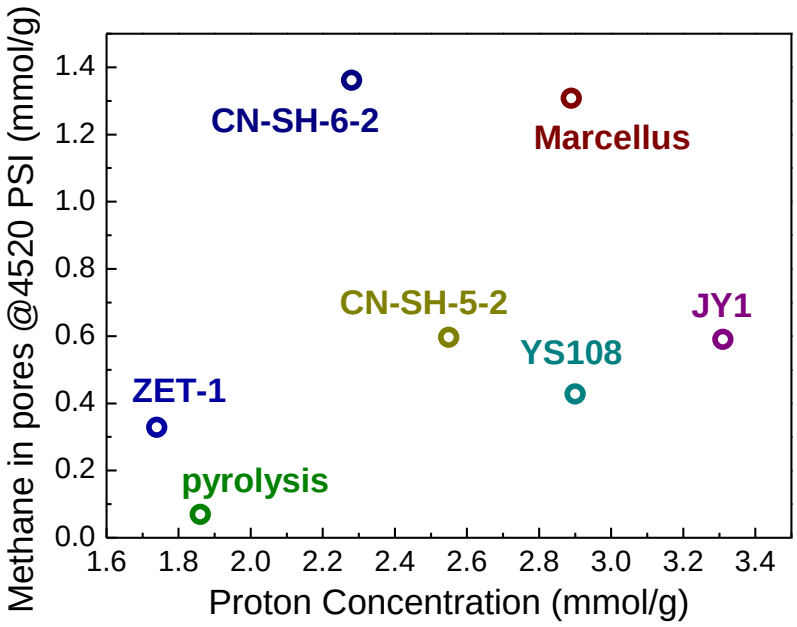

Figure 4.19 Methane storage at 4520 PSI vs. proton concentration.

4.4.3 Maturity

We don't have sufficient *Ro* data for the shale samples, so only the methane storage at 4520 PSI vs. T_{max} is shown in Figure 4.20.

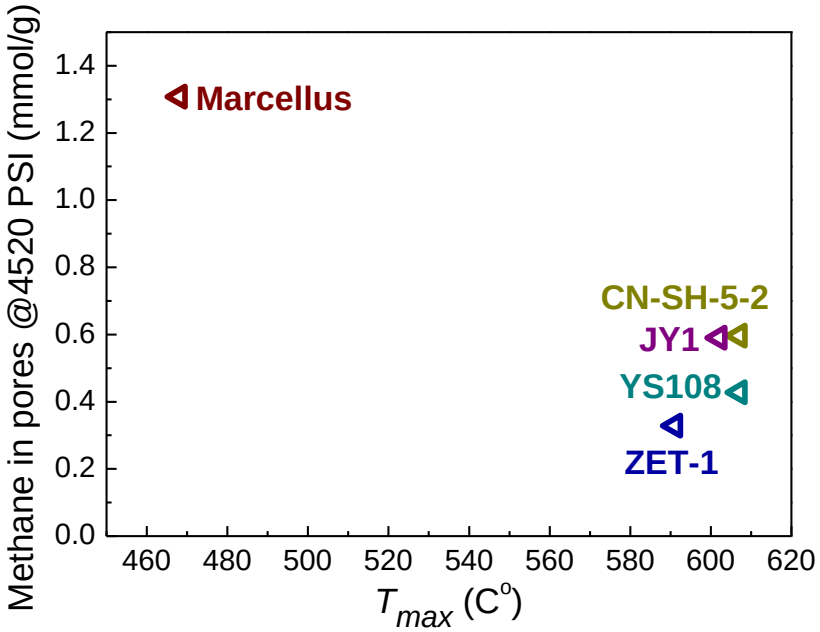

Figure 4.20 Methane storage at 4520 PSI vs. T_{max}.

As discussed in Section 4.3.1, the ratio of TOC to protons is also a parameter to evaluate

the maturity of samples, so the correlation between methane storage and TOC/protons is shown in Figure 4.21.

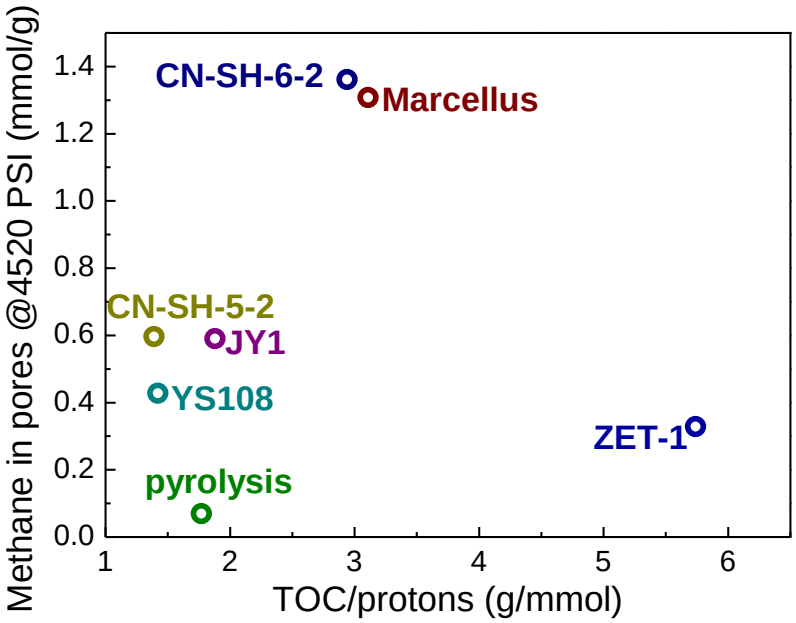

Figure 4.21 Methane storage at 4520 PSI vs. TOC/protons

According to the result, the samples (*CN-SH-6-2* and *Marcellus*) which are in the region of $\mathrm{TOC/protons} \sim 3$ show the highest methane storage. The *CN-SH-5-2*, *JY1*, *YS108* and the *pyrolysis* samples are sub-mature. The *ZET-1* sample is overmature.

4.4.4 Narrow Peak of Spectrum

Since there is a possible correlation between the high-pressure long component T_2 (Section 4.2.4) and the T_2^* of the narrow peak in the ^1H spectra of samples (Section 4.2.1), the storage properties may depend on the narrow peak. Therefore, both the proton concentration and T_2^* from the narrow peak are plotted as a function of methane storage at 4520 PSI to study the correlation.

The correlation between the concentration of the narrow peak protons and methane storage is shown in Figure 4.22.

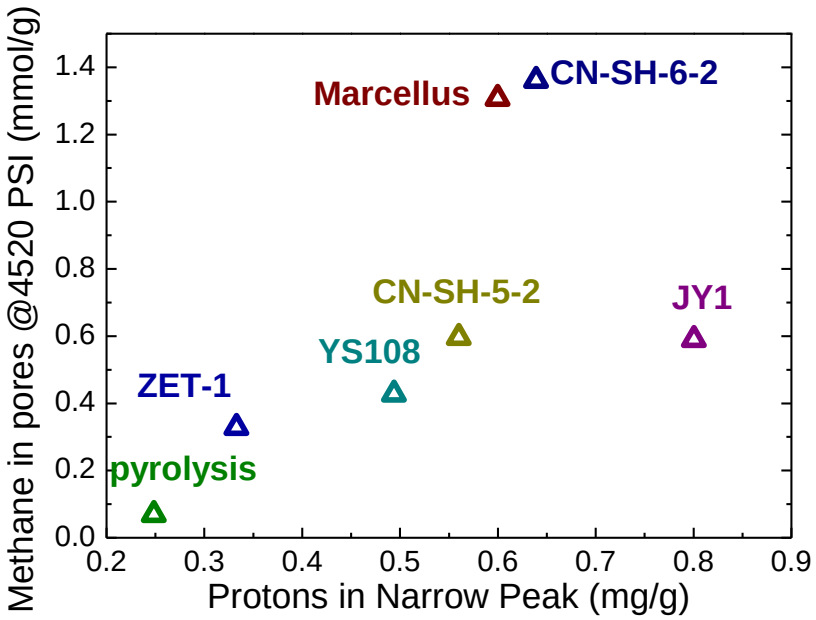

Figure 4.22 Methane storage at 4520 PSI vs. narrow peak proton concentration.

The correlation between the T_2^* value from the narrow peak and methane storage is shown in Figure 4.23.

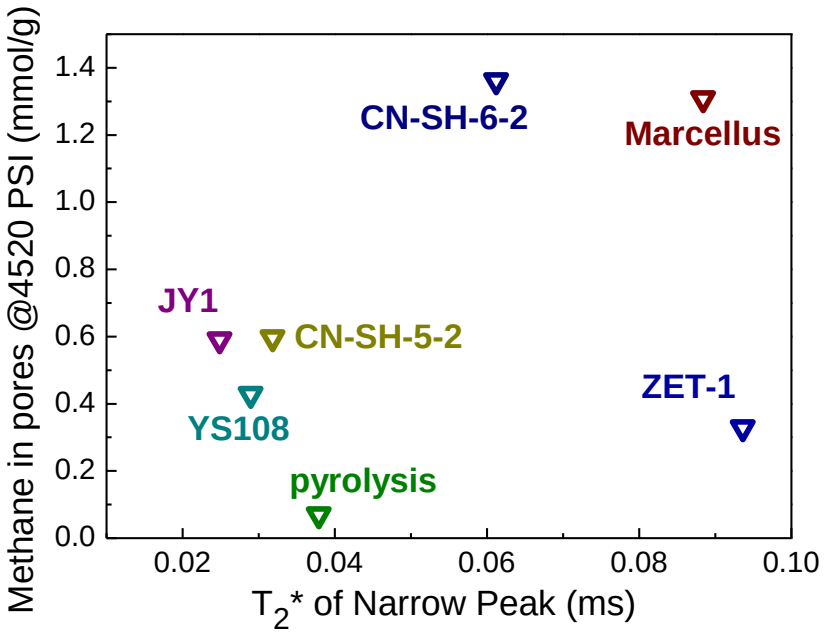

Figure 4.23 Methane storage at 4520 PSI vs. T_2^* of the narrow peak in spectra.

According to the results shown in Figure 4.22 and Figure 4.23, the narrow peak in the

^{1}H spectrum is possibly an indicator of methane storage capability in shale samples. The "best regions" are about $0.6 \sim 0.7$ mmol/g of the proton concentration and $0.6 \sim 0.9$ ms of the T_2^*

REFERENCES

[1] Tissot BP, Welte DH. Petroleum formation and occurrence: Springer Science & Business Media; 2013.

[2] Premović P, Jovanović LS, Michel D. Solid-State ^{13}C and ^{1}H NMR in Kerogen Research: Uncertainty of Aromaticity Estimation. Applied Spectroscopy. 1992;46(11):1750-2.

[3] Hirata S-i, Akiyama M. ^{1}H-NMR T_1 as a possible parameter to diagenesis. Geochemical Journal. 1982;16(2):97-8.

[4] Ujii é Y. Thermal alteration of kerogen as an indicator of contact metamorphism to sedimentary rocks; ^{1}H-NMR T_1 and elemental composition. Geochemical Journal. 1984;18(3):163-6.

[5] Yale DP, Nur A. Network modeling of flow, storage, and deformation in porous rocks. SEG Technical Program Expanded Abstracts 1985: Society of Exploration Geophysicists 1985, p. 91-4.

[6] Chen T, Feng X-T, Pan Z. Experimental study of swelling of organic rich shale in methane. International Journal of Coal Geology. 2015;150:64-73.

[7] Karacan CÖ. Heterogeneous sorption and swelling in a confined and stressed coal during CO_2 injection. Energy & Fuels. 2003;17(6):1595-608.

[8] Reucroft P, Patel H. Gas-induced swelling in coal. Fuel. 1986;65(6):816-20.

CHAPTER 5. CONCLUSIONS

5.1 Conclusions

As discussed in Section 1.3, although adsorption is the conventional characterization method of porous materials, it has two significant disadvantages: first, it can only produce an adsorption isotherm, without any direct dynamic information. Therefore, the result highly relies on the specific assumptions of adsorption models. Second, in evaluating the adsorption of high-pressure gas, such as methane at 4500 PSI, it can only provide the information on the adsorption, nothing about the whole pore space. This is because the adsorption measurement, whether it is the volumetric method or the gravimetric method, can only observe the adsorbate through the density difference between the vapor and the adsorption/condensation states. This information is generally not sufficient to solve complicated problems with multiple interaction mechanisms, such as micropore filling in a complex pore system. Once there is no density difference, such as occurs in high-pressure gas adsorption, the adsorption method cannot provide any useful information.

On the contrary, NMR is a much more powerful technique. It can probe materials through the chemical shift, which is based on the ‘contrast’ of the local magnetic field, and by the longitudinal and transverse relaxations, which provide information about system dynamics at different time scales.

In contrast to conventional NMR methods that study the nucleus of target material itself, the methods introduced in Chapter 2 and Chapter 3 are based on the detection of probe molecules loaded into the pores to reflect the properties of pore space. In Chapter 2, water is used as the probe molecule and the porous properties of ACs are detected based on the

chemical shift information. In Chapter 3, methane is used as a probe molecule and the porous properties of gas shale are studied according to information from both the chemical shift and the relaxation times.

Although the direct application of the method introduced in Chapter 2 is to characterize the pore size and PSD of AC samples, it also offers a powerful technique to study the properties of materials confined inside micropores. According to the DFT simulation result in Chapter 2, the NICS effect is very sensitive to the distance between probe nucleus and carbon surface when the distance is smaller than 2nm. That provides a nanometer scale spatial contrast inside micropores. Using these advantages, Zhi-Xiang Luo has studied the dehydration properties of ions [1]. By combining spatial information and dynamics information, Yan Song studies works on the water adsorption processes [2]. Meanwhile, ACs synthesized in our lab is a very useful conductive material with tunable pore size and relatively narrow PSD. It is a good material for the study of supercapacitor mechanisms [3].

The method introduced in Chapter 3 provides not only a reliable tool for the evaluation of gas shale samples but also a powerful technique to study the storage mechanism of nature gas in shale samples. As discussed in Chapter 4, there are several parameters can be acquired from NMR measurements. Correlation of these parameters with those from conventional industry measurements would provide a better understanding of the properties of shale samples. Moreover, the study of the dynamics of methane inside pores is crucial for understanding of the storage mechanisms of nature gas.

REFERENCES

[1] Luo Z-X, Xing Y-Z, Liu S, Ling Y-C, Kleinhammes A, Wu Y. Dehydration of Ions in Voltage-Gated Carbon Nanopores Observed by in Situ NMR. The journal of physical chemistry letters. 2015;6(24):5022-6.

[2] Song YC, Yuan; Raghavan, Arjun; Xing, Yun-Zhao; Ling, Yan-Chun; Kleinhammes, Alfred; Wu, Yue. Nucleation and Growth Process of Water Adsorption in Micropores of Activated Carbon Revealed by NMR. J Phys Chem C. 2017;Accepted.

[3] Luo Z-X, Xing Y-Z, Ling Y-C, Kleinhammes A, Wu Y. Electroneutrality breakdown and specific ion effects in nanoconfined aqueous electrolytes observed by NMR. Nature communications. 2015;6.